EXPLORATORY MODELLING OF BARRIER COAST DYNAMICS KOEN REEF 1

EXPLORATORY MODELLING OF BARRIER COAST DYNAMICS

KOEN REEF

INVITATION

YOU ARE CORDIALLY INVITED TO ATTEND THE PUBLIC DEFENCE OF MY DOCTORAL THESIS:

EXPLORATORY MODELLING OF BARRIER COAST DYNAMICS

ON JANUARY 13TH 2022 AT 16:45 AT THE UNIVERSITY OF TWENTE

AT 16:30 I WILL PRESENT AN OVERVIEW OF MY THESIS

KOEN REEF
KOEN.REEF@GMAIL.COM

EXPLORATORY MODELLING OF BARRIER COAST DYNAMICS

Koen Rutger Gerwin Reef

EXPLORATORY MODELLING OF BARRIER COAST DYNAMICS

DISSERTATION

to obtain
the degree of doctor at the Universiteit Twente,
on the authority of the rector magnificus,
prof. dr. ir. A. Veldkamp,
on account of the decision of the Doctorate Board
to be publicly defended
on Thursday 13 January 2022 at 16.45 hours

by

Koen Rutger Gerwin Reef

born on the 9th of July, 1993
in Hengelo, The Netherlands

This dissertation has been approved by:

Supervisor
prof.dr. S.J.M.H. Hulscher

Co-supervisors
dr.ir. P.C. Roos
prof.dr. H.M. Schuttelaars

Cover design: Koen Reef, adapted from NASA
Printed by: Ipskamp Printing
Lay-out: Koen Reef
ISBN: 978-90-365-5318-6
DOI: 10.3990/1.9789036553186

Graduation Committee:

prof.dr.ir. H.F.J.M. Koopman	University of Twente, chairman and secretary
prof.dr. S.J.M.H. Hulscher	University of Twente, supervisor
dr.ir. P.C. Roos	University of Twente, co-supervisor
prof.dr. H.M. Schuttelaars	Delft University of Technology, co-supervisor
prof.dr. K.M. Wijnberg	University of Twente
prof.dr. R.W.M.R.J.B. Ranasinghe	University of Twente, IHE
prof.dr.ir. Z.B. Wang	Delft University of Technology
prof.dr. P. Hoekstra	Utrecht University
prof.dr. A.B. Murray	Duke University

Keep buggering on

— Winston Churchill

Voorwoord

Eindelijk is het zover, aan vijf jaar als promovendus komt een einde met het verdedigen van mijn proefschrift. De eerste drie jaar heb ik ontzettend genoten van het leren van tal van nieuwe vaardigheden, het bezoeken van prachtige exotische oorden, en de vele gezellige activiteiten met collega's. Het is ook in die periode dat de inhoudelijke hoofdstukken van dit proefschrift tot stand zijn gekomen.

Toen Covid-19 ten tonele verscheen veranderde er veel, niet in de laatste plaats omdat ik zelf ernstig ziek ben geworden. Maandenlang ben ik bezig geweest met het herstellen van benauwdheid, inspanningsintolerantie, en vermoeidheid. Iets wat uiteindelijk ook bijzonder goed gelukt is. Tijdens het begin van mijn ziekteperiode heb ik veel begrip en ondersteuning vanuit de Universiteit ervaren. Helaas sloeg dit later om in onbegrip en voelde het alsof ik niet alleen tegen Long-Covid en een Burn-Out vocht, maar in meerdere gevallen ook tegen de UT zelf.

Dit proefschrift was er niet geweest zonder iedereen die mij de afgelopen jaren — maar vooral de afgelopen anderhalf jaar — gesteund en geholpen hebben. Ik gebruik dit voorwoord dan ook graag om deze mensen te bedanken.

Pieter bedankt voor jouw vakinhoudelijke kennis, en jouw positiviteit op de momenten dat het telt. Wij delen dezelfde humor en ik heb genoten van de vele goede en slechte grappen. Ook de rondjes hardlopen waren altijd erg plezierig en wat mij betreft is het laatste rondje samen nog niet gelopen! Henk bedankt voor jouw inhoudelijk scherpe blik en vernieuwende ideeën.

Mannen van W211, Johan, Michiel en Pim, bedankt voor de erg plezierige jaren op kantoor! Of het nou een goed gesprek, een slechte grap, of gewoon slap gelul was, ik heb van onze tijd samen genoten. Anouk, Andrea, Geert, Daan, Joost, Mathijs, Sara, en Wessel, bedankt voor de gezelligheid tijdens het sporten. Ik heb erg genoten van al het hardlopen, boulderen, en squashen! Daan, Geert, en Koen Berends bedankt voor de mooie momenten in het buitenland, ik zal de gesprekken in Shanghai, Beijing, Cuba, en Nieuw-Zeeland niet snel vergeten! Daarnaast dank ik ook alle andere collega's van WEM voor de mooie momenten samen.

Ten slotte wil ik mijn ouders bedanken die er altijd voor mij geweest zijn, en die voor mij gezorgd hebben toen ik dat zelf niet meer kon.

Summary

Barrier coasts are a distinct type of coast characterized by a chain of barrier islands and tidal inlets separated from the mainland coast by a backbarrier basin or lagoon. They cover around 10% of the world's coastline and they display a variety of shapes and sizes. Barrier coasts possess outstanding ecological values and are economically important for activities such as navigation, resources extraction, and tourism. Furthermore, they mitigate the effect of storms on the outer sea by shielding the mainland coast. Besides their functionality, barrier islands are prone to flooding, due to their low elevation and closeness to sea. This can have significant consequences, as in 2012 when Hurricane Sandy caused three breaches in the barrier islands off the coast of Long Island.

To maintain barrier coast functionalities and to curb the natural dynamics, barrier coasts are often subject to human interventions. More recent examples include the jettification of inlets to improve the inlet navigability, dredging of shipping channels, sand nourishments to counteract erosion, and the artificial opening and closing of tidal inlets. Notwithstanding the abundance of human interventions, the knowledge necessary to effectively apply long-term management of these systems is lacking, leading to less efficient and more expensive short-term management decisions. In this thesis we support the shift from short-term management to more cost-efficient long-term management by expanding our knowledge on the long-term evolution of barrier coasts and answer the following research questions:

1. What is the influence of back-barrier basin planview geometry, and changes therein, on multiple inlet systems?

2. What is the impact of storm-induced breaches on multiple inlet systems, and how is this affected by climate change?

3. How do variations in back-barrier basin geometry and storm surge characteristics affect storm surges in the Western Dutch Wadden Sea?

To answer the first research question, we extend an existing barrier coast model, to allow for the inclusion of arbitrary backbarrier basin geometries. Using this extended model, we studied the response of multiple inlet systems to variations in basin size and study the role of tidal resonance and bottom friction on this. We find that the total tidal prism through all inlets is predominantly determined by the (cross-shore) width of the basin and identify three regimes for this. Firstly, a linear regime for the shortest basins, followed by a resonant regime, and finally a regime in which the tidal wave dissipates due to bottom friction.

To answer the second research question, we again extend an existing barrier coast model to include the formation of storm-induced breaches. Using this

model, we perform Monte Carlo simulations to find how multiple inlet systems respond to storm-induced breaches. We found that if a barrier coast is in equilibrium, a new open inlet can cause the existing inlets to shrink. Furthermore, we find that the distance between a storm-induced breach and the existing neighbouring inlets is the most important predictor for whether an inlet remains open or not. Climate change driven changes in storm climate will result in changes in the time-scale in which these changes happen.

To answer the third research question, we extend the historical model used to study the impact of a large closure dam in the Netherlands on the remaining barrier coast system. We found that the maximum surge height strongly depends on the length of the basin, as a longer basin results in a longer wind-fetch length.

Samenvatting

Barrièrekusten, zoals de Waddenzee, worden gekenmerkt door een schakeling van barrière-eilanden afgewisseld met zeegaten, die van het vaste land gescheiden worden door een getijdebekken. Dit kusttype beslaat ongeveer 10% van de wereldwijde kustlijn en laat een grote verscheidenheid aan vormen en schalen zien. Barrièrekusten zijn belangrijke ecologische systemen en zijn economisch belangrijk vanwege scheepvaart, grondstof winning en toerisme. Daarnaast verminderen ze het effect van stormen door het afschermen van het vaste land. Hier tegenover staat de kwetsbaarheid van barrière-eilanden voor overstromingen door hun lage ligging nabijheid van de zee. Dit kan grote gevolgen hebben, zoals in 2012, toen Orkaan Sandy drie doorbraken veroorzaakte in barrière-eilanden voor de kust van Long Island, New York.

Om de functionaliteiten van barrierkusten te behouden en de natuurlijke dynamiek te beperken, worden barrièrekusten vaak beheerd en vinden menselijke ingrepen vaak plaats. Recente voorbeelden zijn het aanleggen van strekdammen ten bate van de scheepvaart, het uitbaggeren van vaarroutes, het opspuiten van zand op stranden om erosie tegen te gaan, en het kunstmatig openen en dichten van zeegaten. Ondanks het veelvuldig ingrijpen in deze systemen ontbreekt ons de noodzakelijke kennis om effectief lange-termijn beheer toe te passen. Dit leidt tot minder effectief en duurder korte-termijn beheer. In dit proefschrift ondersteunen ik de transitie van korte-termijn beheer naar lange-termijn beheer door onze kennis over de lange-termijn evolutie van barrièrekusten te vergroten en beantwoord ik de volgende onderzoeksvragen:

1. Wat is de invloed van de geometrie van het getijde-bekken, en veranderingen hierin, op systemen van meerdere zeegaten?
2. Wat is de impact van stormdoorbraken op systemen van meerdere zeegaten, en hoe wordt die beïnvloed door klimaatverandering?
3. Hoe beïnvloeden variaties in de geometrie van het getijde-bekken en storm karakteristieken stormvloeden in de Nederlandse Waddenzee.

Om de eerste onderzoeksvraag te beantwoorden hebben we een bestaand barrièrekust model uitgebreid, om getijdebekkens met een willekeurige vorm te kunnen doorrekenen. Met behulp van dit model hebben we bestudeerd hoe systemen van meerdere zeegaten reageren op variaties in grootte van het getijdebekken, en wat de rol van resonantie en bodemwrijving hierin is. Wij ontdekten dat het totale volume aan water wat gedurende een getijdecyclus door alle zeegaten van één barrièrekust stroomt voornamelijk beïnvloed wordt door de vorm van het getijdebekken, en we ontdekten hierin drie verschillende regimes. Ten eerste, een lineair regime, een resonant regime, en een regime waarin bodemwrijving dominant is.

Om de tweede onderzoeksvraag te beantwoorden, hebben we wederom een bestaand barrièrekust model uitgebreid. Ditmaal om stormdoorbraken mee te nemen in ons model. Met behulp van dit model, hebben we een Monte Carlo simulatie uitgevoerd om te bestuderen hoe system van meerdere zeegaten reageren op stormdoorbaken. Wij ontdekten dat als een barrièrekust zich in een evenwichtssituatie bevindt dat dan een nieuw zeegat, ontstaan als stormdoorbraak, de bestaande zeegaten kan verkleinen. De belangrijkste voorspeller voor het openblijven van een stormdoorbraak is de afstand tussen de stormdoorbraak en reeds bestaande zeegaten. Veranderingen in stormklimaat door klimaatverandering zal resulteren in een verandering van de tijdschaal waarop systemen van meerdere zeegaten zich aanpassen aan nieuwe stormdoorbraken.

Om de derde onderzoeksvraag te beantwoorden, breiden we een historisch model uit dat gebruikt is om de impact van de Afsluitdijk op de Waddenzee te bepalen. Wij ontdekten dat de maximale stormvloedhoogte sterk afhangt van de grootte van het getijdebekken, omdat er in grotere bekkens een langere strijklengte is voor de wind, wat resulteert in hogere stormvloeden.

Contents

Chapter 1: Introduction

1.1. Barrier coasts

Coastal regions have long since attracted people, as they offer both terrestrial and marine opportunities. It is estimated that 2.4 billion people or around 40% of the world's population live within 100 km of the coast and 600 million people or around 10% of the world's population live in areas less than 10 m above sea level (United Nations, 2017).

Barrier coasts are a distinct type of coast characterized by a chain of barrier islands and tidal inlets separated from the mainland coast by a backbarrier basin or lagoon. They cover around 10% of the world's coastline (see Figure 1.1) and they display a variety of shapes and sizes (Glaeser, 1978; Stutz and Pilkey, 2011). Four barrier coasts illustrating this variety are shown in Figure 1.2: panel a shows the Danish, Dutch, and German Wadden Sea (e.g. Wang et al., 2012; Oost et al., 2012), panel b shows the Portuguese Ria Formosa (e.g. Salles et al., 2005; Pacheco et al., 2008; Dias et al., 2009), panel c shows the New York Long Island coast (e.g. Leatherman, 1989; Yu et al., 2018), and panel d shows and North Carolina Outer Banks (e.g. Inman and Dolan, 1989; Mallinson et al., 2010; Mallinson et al., 2018).

Barrier coasts possess outstanding ecological values and are economically important for activities such as navigation, resources extraction, and tourism (e.g. Wang et al., 2012). Furthermore, they mitigate the effect of storms on the outer sea by shielding the mainland coast. Besides their functionality, barrier islands are prone to flooding, due to their low elevation and closeness to sea. This can have significant consequences, as in 2012 when Hurricane Sandy caused three breaches in the barrier islands off the coast of Long Island.

Most present-day barrier coasts formed in the late Holocene when sea level rise slowed and are the product of the reworking of sediments (Oost et al., 2012; Stutz and Pilkey, 2011; Mallinson et al., 2018). The archetypical shape of barrier coasts is the result of an interplay of various aeolian, hydrodynamic, and morphodynamic processes (e.g. De Swart and Zimmerman, 2009; Wang et al., 2012). The consequence of this complex interplay is that barrier coasts are dynamic systems, whose morphology is changing continuously.

To maintain barrier coast functionalities and to curb the natural dynamics, barrier coasts are often subject to human interventions. Early examples that started around 1000 CE include the construction of dikes and mounds to protect settlements and increase the area of arable land (Oost et al., 2012). More recent examples include the jettification of inlets to improve the inlet navigability, dredging of shipping channels, sand nourishments to counteract erosion, and

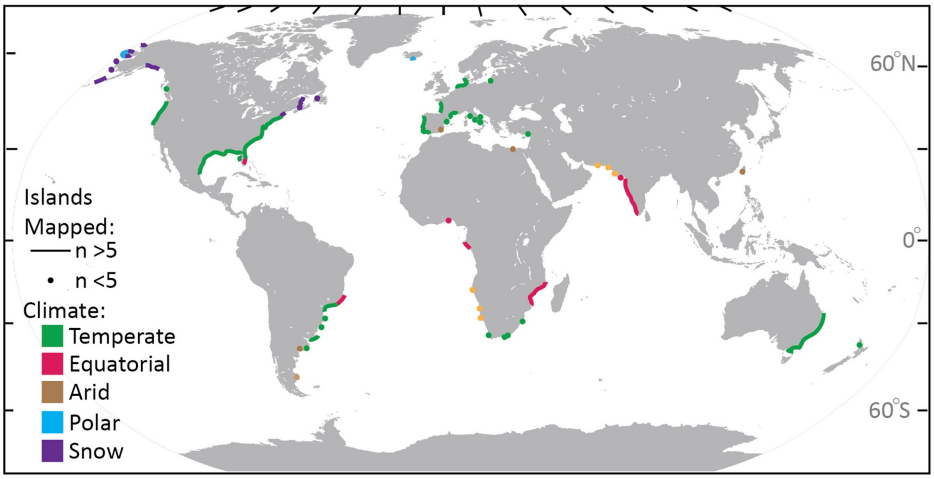

Figure 1.1: Map adapted from Mulhern et al. (2017), showing the global distribution of barrier islands and spits mapped by them; colors are used to indicate different climates.

the artificial opening and closing of tidal inlets. Notwithstanding the abundance of human interventions, the knowledge necessary to effectively apply long-term management of these systems is lacking, leading to less efficient and more expensive short-term management decisions (e.g. Wang et al., 2012).

In the remainder of this chapter: an overview of the most relevant processes affecting barrier coasts is provided in §1.2, challenges in barrier coast management are discussed in §1.3, knowledge gaps are identified in §1.4, the aim and research questions of this thesis are presented in §1.5, and an outline of the methodology is given in §1.6.

1.2. The morphological evolution of barrier coasts

In this section I firstly provide a brief overview of the morphological evolution of barrier coasts on a full system level and then provide an overview of the current knowledge on the equilibria of single, double and multiple inlet systems. The evolution and equilibrium properties of tidal inlets are of particular importance for the evolution of barrier coasts, as tidal inlets form the connection between the tidal backbarrier basin and the outer sea, separate barrier islands, and allow tidal co-oscillations in the backbarrier basin.

Firstly, in §1.2.1, I present the relevant observations, classifications, and physical processes affecting the morphological evolution of barrier coast systems as a whole on different timescales. Secondly, in §1.2.2, I focus on the equilibria

Figure 1.2: Satellite images of four barrier coasts. a: Danish, Dutch, German Wadden Sea (Image adapted from NASA). b: Portuguese Ria Formosa (Google, 2016). c: United States, New York, Long Island barrier coast (Google, 2016). d: United States, North Carolina, Outer Banks (Google, 2016).

of single inlet systems, the stability concept of Escoffier (1940), and the role of exploratory modelling. Thirdly, in §1.2.3, I discuss the initial inability of exploratory models to find stable equilibria for double inlet systems, and how the consideration of additional processes has led to finding stable equilibria. Fourthly, in §1.2.4, I describe how the state-of-the-art model by Roos et al. (2013) has enabled us to find and study the equilibrium properties of multiple inlet systems and briefly describe how the model works.

1.2.1 Observations, classifications, and physical processes

Barrier coasts are dynamic systems whose morphology continuously changes under the natural influence of hydrodynamic and morphodynamic processes. Observations from the present-day system, historical sources, and geological sources help in understanding how these processes affect the morphological evolution of barrier coasts (Oost et al., 2012), as described below.

Observations from the geological record show that most present-day barrier coasts emerged during the Holocene when the rate of sea level rise decreased (Stutz and Pilkey, 2011; Oost et al., 2012; Mallinson et al., 2018). Rather than being fixed in place ever since, the location of barrier islands has changed due to cross-shore regression and transgression and long-shore migration (Curray, 1964; Vila-Concejo et al., 2004; Simms et al., 2006; Hayes and FitzGerald, 2013). In general, the migration of barrier islands is the result of sedimentation on one side of the island and erosion on the other side. This is driven by processes such as tide and wave driven sediment transport for long-shore migration; and shore face deposition and storm-driven overwash for transgression and regression.

Historical sources such as maps show us that besides migration new inlets and islands can form or inlets can close and islands can merge. The processes driving this can be natural and anthropogenic. Naturally, new inlets form from storm-induced breaches that grow as tidal flows erode the newly formed breach, simultaneously splitting an existing barrier island in two in the process. If there is continuous sedimentation in an inlet channel, it will eventually close and the two barrier islands on either side of the inlet will merge. The same can happen due to human interventions, although usually on a shorter timescale (e.g. Vila-Concejo et al., 2004). New inlets have been artificially closed to protect human interest (e.g. after Hurricane Sandy on Fire Island, NY, USA; Hinrichs et al., 2018) and new inlets have been created to facilitate navigation (e.g. at the Ria Formosa, Portugal; Vila-Concejo et al., 2004).

Observations of present-day barrier coasts (i.e. between a century old and current state) have resulted in classifications linking the tidal and wave conditions to the shape of barrier islands. Based on the tidal range (TR) on the outer

sea, barrier coasts can be classified as microtidal (TR < 2 m), mesotidal (TR = 2-4 m), and macrotidal (TR > 4 m); (e.g. Hayes, 1979; Hayes and FitzGerald, 2013). This has long been linked to the shape of barrier islands, i.e. long and thin on microtidal coasts, drumstick shaped on mesotidal coasts, and absent on macrotidal coasts (Hayes, 1979). Later, Davis and Hayes (1984) argued that the relative magnitude of tides and waves is what characterizes barrier coasts. They identified three types of barrier coasts:

- wave-dominated with long-thin barrier islands;
- mixed energy, affected both by tides and waves with drumstick shaped barrier islands;
- tide-dominated with small or nearly absent barrier islands.

More recently, an analysis of 702 barrier islands from around the world showed that tidal range and wave height only account for 10% of the variance in island shape (Mulhern et al., 2017). This implies that other factors play an important role in determining barrier island shape as well.

Observations of the equilibrium properties of tidal inlets have resulted in various empirical relations such as the O'Brien-Jarret law linking the total volume of water entering and leaving an inlet every tidal cycle (i.e. the tidal prism) to the equilibrium cross-section of the inlet channel (O'Brien, 1931; O'Brien, 1969; Jarret, 1976). In the next section, the stability of single, double, and multiple inlets is discussed.

1.2.2 The equilibrium of single tidal inlets & the stability concept of Escoffier

The equilibrium properties of single tidal inlet systems in mixed energy barrier coasts (see §1.2.1) were treated by Escoffier (1940) who described that an inlet is in equilibrium if the erosion due to the tide and the accretion due to waves are in balance. Furthermore, depending on the response of an inlet system in equilibrium to small perturbations in the inlet's cross-section an inlet is considered stable if it returns to its equilibrium cross-section, and unstable if it does not. Besides introducing a stability concept, Escoffier also introduced a (mathematical) model to provide insight in how physical processes affect tidal inlets. The model introduced by Escoffier can be classified as an exploratory model as it focuses on a limited number of processes instead of attempting to simulate the entire system in large detail (Murray, 2003).

Escoffier (1940) presented a simple morphological model to study the stability of single inlet systems. He argued that the erosion and accretion in an

inlet can be linked to the balance between the tidal velocity amplitude in an inlet U and an equilibrium velocity U_{eq}. If $U > U_{eq}$ an inlet channel erodes and its cross-section increases, if $U = U_{eq}$ an inlet is in equilibrium and its cross-section remains unchanged, and if $U < U_{eq}$ an inlet channel accretes and its cross-section decreases.

By combining the simple morphological model with a simple lumped hydrodynamic model in which the tidal velocity amplitude in an inlet is affected by the cross-section of the inlet, Escoffier (1940) found 'closure curves' (i.e. showing the inlet's velocity amplitude U as a function of inlet area A) that show the response of an inlet's cross-section to variations in tidal velocity amplitude, see figure 1.3. Escoffier's closure curves show that by taking the inlet's tidal velocity amplitude U as a function of inlet cross-sectional area A, and intersecting this with an equilibrium velocity U_{eq}; zero, one, or two equilibria are found. Depending on the response of the inlet to perturbations in the equilibrium state, an inlet can either be stable if it returns to its equilibrium state, or unstable if it does not. If two equilibria are found, one is stable and one is unstable; if both coincide, one unstable equilibrium is found; if $U < U_{eq}$ for all A, no equilibrium is found. Support for this stability concept has more recently been provided by numerical simulations using detailed process-based models (Nahon et al., 2012; Tran et al., 2012).

1.2.3 Equilibria of double inlet systems

The first time that Escoffier's approach was extended to double inlets systems (consisting of two inlets connected to the same backbarrier basin), this did not result in stable equilibrium with two open inlets (Van de Kreeke, 1990a; Van de Kreeke, 1990b). Later it was argued that the model did not take essential physical processes into account for double inlet systems, and by adding these processes stable equilibria for double inlet systems were found. These processes include: tidal divides (Van de Kreeke et al., 2008; De Swart and Volp, 2012), hypsometric effects (De Swart and Volp, 2012), entrance/exit losses (Brouwer et al., 2012b), and spatially varying water levels (Brouwer et al., 2013).

Similar to the model by Escoffier (1940), these models are considered exploratory as they only focus on the most relevant processes without trying to simulate the natural system in as much detail as possible.

1.2.4 Equilibria of multiple inlet systems — the model of Roos et al. (2013)

More recently, Roos et al. (2013) found stable multiple inlet equilibria using an exploratory model. The model consists of an idealized hydrodynamic model

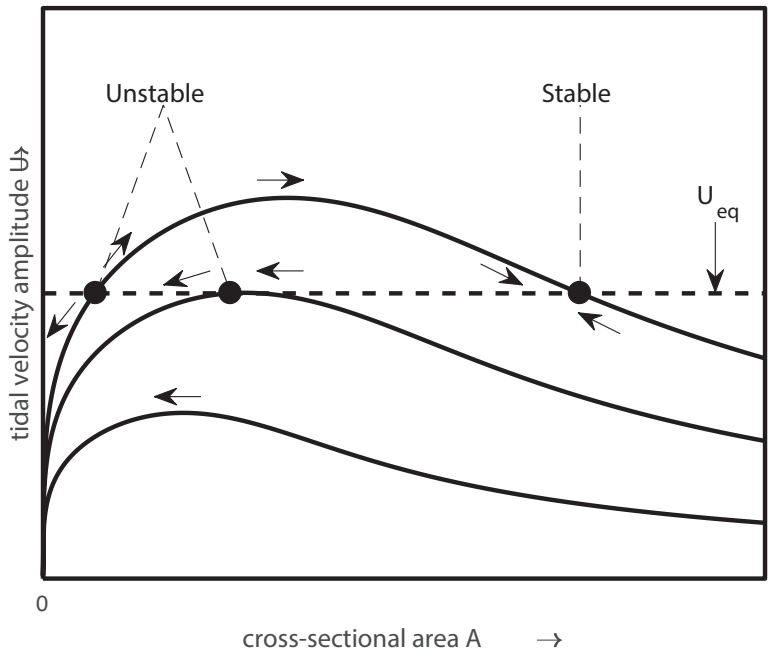

Figure 1.3: A closure curve for a single inlet, as presented by Escoffier (1940). The closure curve shows the inlet's velocity amplitude U as a function of inlet area A. Intersection with equilibrium velocity $U = U_{eq}$ yields zero, one or two equilibria. In the case of two equilibria one is stable and one is unstable, one equilibrium is found if both coincide and none is found if $U < U_{eq}$ for all A.

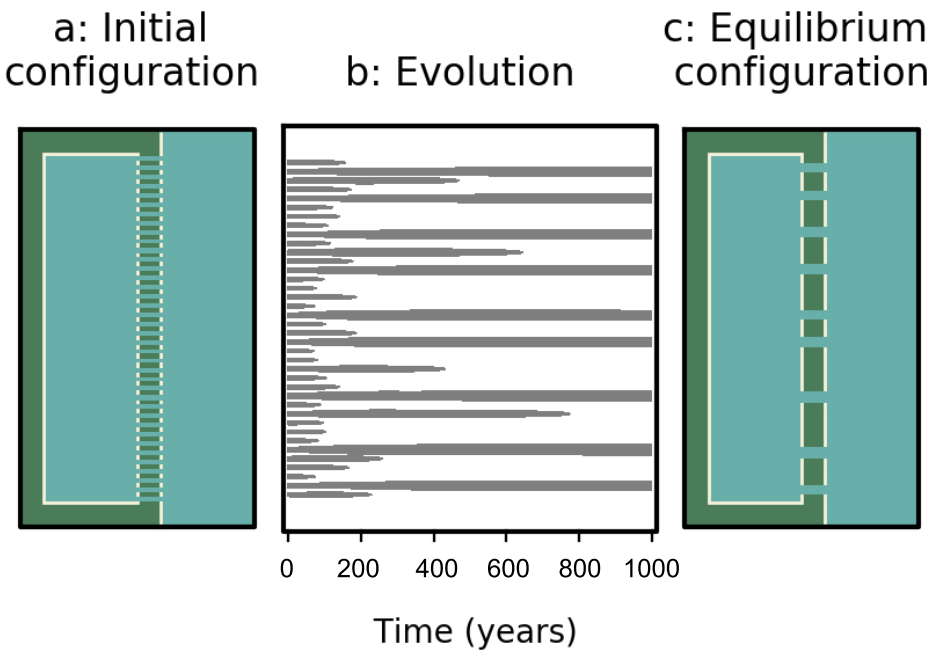

Figure 1.4: Example simulation of the idealized model by Roos et al. (2013). The initial model domain in blue consists from left to right of a tidal basin, $J = 40$ tidal inlets, and the outer sea (panel a). Next, the evolution of the tidal inlets is modelled (panel b) and an equilibrium configuration in which nine inlets remain open is found (panel c).

that takes spatially varying hydrodynamics into account and a morphological model based on the stability concept of Escoffier (1940). It has been used to investigate the processes stabilizing multiple inlet systems and the model results agreed with observed relationships that link the size of the tidal basin and tidal range with the cross-section of tidal inlets.

The model considers a schematized barrier coast consisting of an outer sea that is connected to a tidal basin through a number of J tidal inlets (see Figure 1.4). In the outer sea the model is forced with a tidal wave, resulting in co-oscillations in the tidal inlets and tidal basin. The inlets are rectangular channels with a fixed shape, with a cross-section A_j that changes depending on the velocity amplitude in the inlet. The strongly schematized tidal basin has a rectangular plan view geometry and a spatially uniform bathymetry, i.e. a constant depth.

An example simulation using the model is shown in Figure 1.4. Here, a

simulation starts with an oversaturated (i.e. with more inlets than in equilibrium) barrier coasts (panel a), whose evolution is simulated (panel b) towards an equilibrium state in which fewer inlets are open (panel c). Due to the idealized nature of the model it is computationally inexpensive — compared to more complex process-based models — allowing for ensemble simulations and extensive sensitivity analyses.

1.3. Challenges in barrier coast management

The wish to shift from short-term management to a more efficient and cost-effective long-term management ultimately stems from the desire to maintain or improve the functionality of barrier coasts for humans (see §1.1). This desire has led to numerous small and large scale interventions that in turn alter the natural evolution of these systems. Two examples of this will be treated in this section, selected to illustrate how a lack of understanding of the relevant processes inhibits us from assessing a priori what the effects of these interventions are. The first is the response of the Western Dutch Wadden Sea to the damming of a large bay in 1932: the Zuiderzee. The second is the artificial closure of two out of three storm-induced breaches after Hurricane Sandy in 2012, along the Great South Bay barrier coasts system — New York, United states of America.

These examples show that the natural long-term morphological evolution of barrier coasts is not considered when these interventions are applied, as the required knowledge of the evolution of the natural system is lacking. In section §1.4 these knowledge gaps are identified and further described.

1.3.1 From sea-claimed bay to agricultural clay: part I

With the construction of a large dam (the Afsluitdijk) between 1927 and 1932, a large bay (the Zuiderzee) was detached from the Western Dutch Wadden Sea, to allow large scale land reclamations (see Figure 1.5). The closure of the Zuiderzee had a profound impact on the hydrodynamics and morphodynamics of the barrier coast system, as the backbarrier basin length was artificially reduced by approximately 60 km.

The hydrodynamics in the Dutch Wadden Sea instantaneously changed. The changes in tidal dynamics were accurately predicted at the time using an idealized process-based mathematical model that considered a network of channels representing the Western Dutch Wadden Sea (State Committee on the Zuiderzee, 1926). However, a lack of process knowledge prevented an accurate assessment of the morphodynamic impact. Observations in the last century show that the morphology of the system underwent significant changes as a result of the basin length reduction (e.g. Elias et al., 2012). The channels leading into the now cut off part of the basin experienced significant infilling, as water was no longer

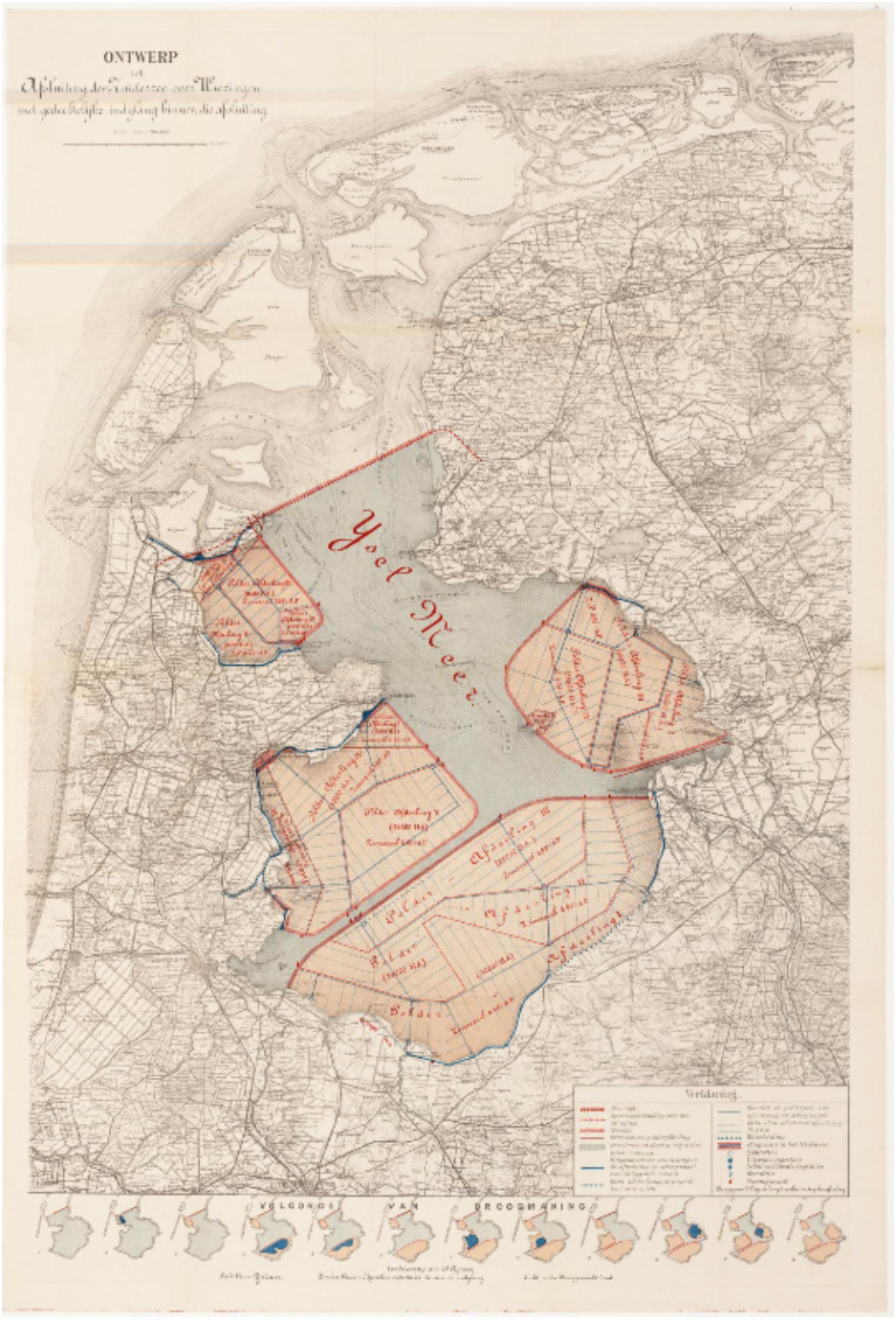

Figure 1.5: Caption on the next page.

Figure 1.5: Overview of land reclamation plans in the Zuiderzee, a former bay of the Western Dutch Wadden Sea (Lely, 1892). The top red line is the closure dam (Afsluitdijk), constructed between 1927 and 1932. The highlighted regions were plans for land reclamation projects, most of which have been implemented.

flowing into the so called Zuiderzee (i.e. the present day Lake IJssel). Furthermore, the tidal inlets connecting the North Sea to the former bay eroded and grew in cross-section, despite the often observed link between larger basins and larger inlets and vice versa (O'Brien, 1931; O'Brien, 1969; Jarret, 1976).

These observations illustrate that we do not completely understand how the equilibrium cross-section of tidal inlets is affected by the size of the tidal basin, and what mechanisms are important.

1.3.2 From storm-induced breaches to human-made beaches

The impact of storms on barrier islands can be devastating and even result in the splitting of barrier islands due to storm-induced breaches. When Hurricane Sandy hit the North-East coast of the United States in October 2012, Fire Island breached in two locations and a new breach appeared near Moriches Inlet. Of these three breaches, two were closed artificially at the cost of $7 million while one breach in the Fire Island wilderness area (i.e. Old Inlet, see Figure 1.6) was allowed to remain open (Bolger, 2012; Bonilla, 2012). Closure of the two breaches was motivated by the desire to better protect the mainland coasts by having

Figure 1.6: Satellite images of three storm-induced breaches at Fire Island and Westhampton (Long Island, NY, USA) due to hurricane Sandy in 2012 showing: a, before the storm (07-March-2012); b, shortly after the storm (04-November-2012); c, almost one year after the storm (20-September-2013). The location of the breaches is indicated with yellow circles. Retrieved from Google Earth (Map Data: DigitalGlobe, USDA Farm Service Agency). Image used with permission from Reef et al. (2020b).

an intact barrier island, while Old Inlet was not closed as to not interfere with the natural system of the wilderness area. Due to these interventions, it remains unknown how the two inlets that were closed would have evolved naturally. There is evidence of historical inlets along Fire Island that have closed naturally (Leatherman, 1985; Leatherman, 1989), hinting at the possibility that they could have closed naturally.

1.3.3 From sea-claimed bay to agricultural clay: part II

The Construction of the Afsluitdijk also served to protect the lands behind the dam from storm surges that historically significantly damaged the area (Rijkswaterstaat, 1916). Even though storm surges no longer occurred in the Zuiderzee and thus no longer posed any danger to the surrounding regions, the storm surges in the remaining Western Dutch Wadden Sea were expected to become more severe.

This expectation was based on rudimentary predictions using again an idealized process-based mathematical model that considered a network of channels representing the Western Dutch Wadden Sea (State Committee on the Zuiderzee, 1926). To make these predictions, the State Committee used their model to computed the storm surge height that a stationary storm would produce in the Western Dutch Wadden Sea, both for the cases with and without Zuiderzee.

While this prediction pointed in the right direction, it completely neglected the transient behavior of storm surges. Furthermore, no results were presented for variations in cross-barrier basin length.

1.4. Knowledge gaps

Below, I identify three knowledge gaps that I aim to fill in this thesis, based on the management issues described in the previous section.

Knowledge gap 1: Backbarrier basin shape

The apparently contrary response of individual tidal inlets and their associated tidal basins to variations in basin shape (see §1.3.1) indicates how poorly understood the effect of basin shape on the equilibria of multiple inlet systems is. Changes in the plan view geometry of a backbarrier basin can have a profound impact on multiple inlet systems. While the changes to the tidal circulation in the remaining Western Dutch Wadden Sea were predicted with remarkable accuracy by State Committee on the Zuiderzee (1926), the morphological response was not.

The increase of inlet cross-section as a response to a basin area reduction differs from a large body of observations that link a larger tidal basin to larger and/or more inlets and a smaller tidal basin to smaller and/or fewer inlets (Elias et al., 2012). These observations of various tidal inlet systems in the United States, showed that there is an almost linear response of the tidal prism and inlet cross-section to variations in basin size. This response has also been confirmed by an idealized modelling study (Roos et al., 2013). These contrary examples indicate our lack of understanding concerning the influence of the size and geometry of a backbarrier basin on the cross-section of tidal inlets.

Knowledge gap 2: Storm-induced breaches

Storms acting on barrier coast systems can have a significant effect on these systems (see §1.3.2). An example is the occasional creation of new tidal inlets due to barrier island breaching under storm conditions. The effect of storms on barrier islands and the process of barrier islands breaching, has been widely studied by combining observations and detailed process-based models such as Delft3D (Cañizares and Irish, 2008; Velasquez Montoya et al., 2018; Van der Lugt et al., 2019) and Xbeach (Lindemer et al., 2010; Sherwood et al., 2014; De Vet et al., 2015; Harter and Figlus, 2017; Mickey et al., 2018). This breaching of barrier islands has a broad impact, ranging from the destruction of properties and infrastructure on barrier islands to changes in the circulation of water in a tidal basin (Hinrichs et al., 2018). The latter also affects the existing inlets that connect to the same backbarrier basin, thus providing a mechanism through which a storm-induced breach affects the existing multiple inlet system. Currently, little is known about the effect of storm-induced breaches on existing multiple inlet system, and specifically the effect on the stability of the surrounding inlets.

Knowledge gap 3: Storm surges in the Dutch Wadden Sea

As described in §1.3.2, storms are an important class of events that can significantly affect barrier coasts. Often flood defences are built, to mitigate the effect of storm surges on coastal regions. A special case of this is the Afsluitdijk, a dam built to separate the Zuiderzee from the Dutch Wadden Sea and to protect the lands around the former Zuiderzee, see §1.3.3. The impact of the Afsluitdijk and detaching the Zuiderzee (thus reducing the cross-barrier basin length) from the Wadden Sea on tidal dynamics was predicted with reasonable accuracy (see §1.3.1), in the early 20^{th} century, using an idealized model in which the Wadden Sea was represented by a network of channels. However, no research has been found that aims to explain how variations in cross-barrier basin length affect the

maximum storm surge height, in the Western Dutch Wadden Sea.

1.5. Aim & Research questions

The research aim of this thesis is to understand the long-term morphological evolution of barrier coasts and specifically the hydrodynamic and morphodynamic processes affecting multiple inlet systems. To do so I will answer the following research questions:

1. What is the influence of back-barrier basin planview geometry, and changes therein, on multiple inlet systems?
2. What is the impact of storm-induced breaches on multiple inlet systems, and how is this affected by climate change?
3. How do variations in back-barrier basin geometry and storm surge characteristics affect storm surges in the Western Dutch Wadden Sea?

1.6. Outline of methodology

The particular research methodologies used to answer our research questions are described in this section. Figure 1.7 shows the relation between the next three chapters of this thesis, in which the three research questions are answered. The conclusions of this thesis are presented in Chapter 5.

Research questions 1 and 2 are answered by extending the existing barrier coast model presented by Roos et al. (2013) (see §1.2.4), research question 3 is answered by extending the model that was historically used to study the hydrodynamic impact of the Afsluitdijk. More extensive descriptions of the methodologies used for each research question are presented in the following subsection.

Research question 1: Basin geometry

To answer the first research question, we extend the existing barrier coast model of Roos et al. (2013), to allow for the inclusion of arbitrary backbarrier basin geometries. This enables us to study the influence of the plan-view geometry of the backbarrier basin on the equilibrium configuration of multiple inlet systems. Furthermore, it improves the schematization of the geometry in idealized barrier coasts models, which was identified by Wang et al. (2012) as one of the main shortcomings of these models.

To allow for the inclusion of arbitrarily shaped backbarrier basins, we adapt the solution strategy such that more complex basin geometries can be included at a slightly higher computation cost. Still, the computational costs remain low

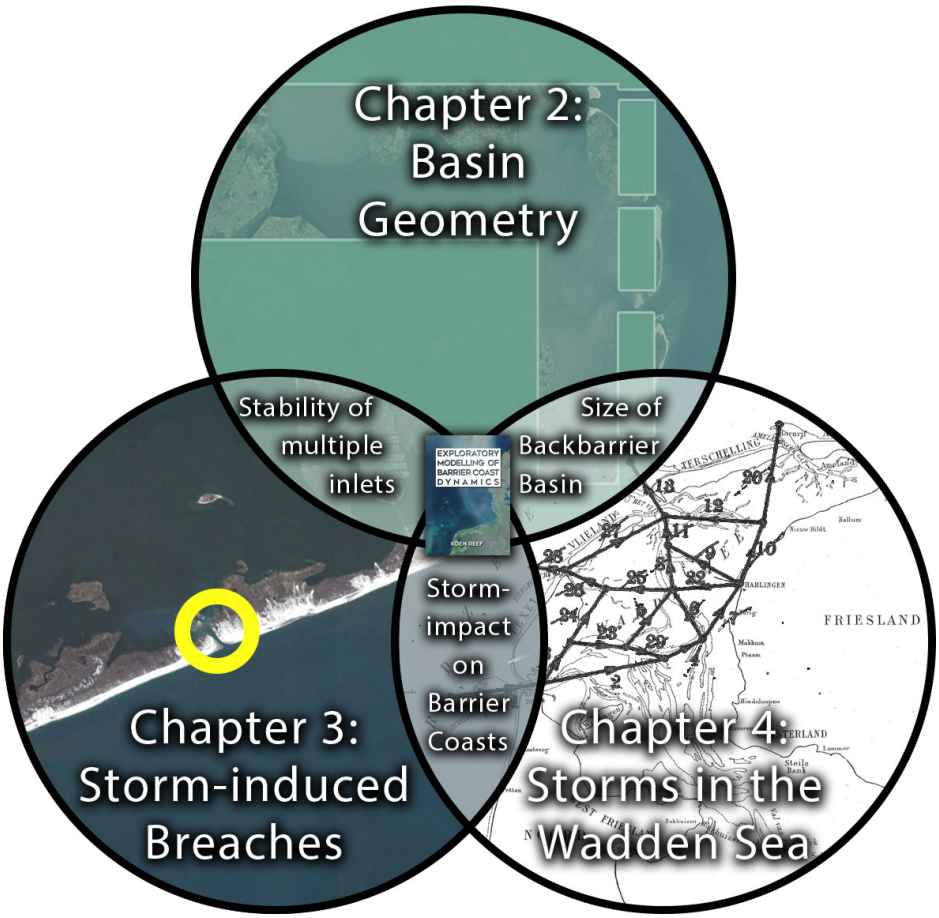

Figure 1.7: Outline showing the topical relations between chapters 2, 3, and 4.

compared to more detailed process-based models so this model remains suitable to perform ensembles consisting of numerous individual simulations.

Using this extended model, we can study the response of multiple inlet systems to variations in basin size and study the role of tidal resonance and bottom friction on this.

Research question 2: Storm-induced breaches

For the second research question, the existing barrier coast model of Roos et al. (2013) is extended by including the formation of storm-induced breaches. This introduces a mechanism for the formation of tidal inlets during a model simulation, based on the natural process of storm-induced barrier island breaching.

Previous studies have already found that the initial condition of long-term barrier coast models has a significant impact on the equilibrium configuration (Dastgheib et al., 2008). Due to this, and in absence of a standard approach to combine stochastic forcing mechanisms — e.g. wind and storms — and deterministic forcing mechanisms — e.g. tides — (Wang et al., 2012) we develop a stochastic shell around the model. This stochastic shell determines at every timestep whether new breaches are formed or not, how many are formed, where they are formed, and what their initial cross-section is. To do so, we use Probability Density Functions that link the occurrence of new breaches to observed storm frequencies along the United States East Coast (Hosseini et al., 2016; Keim et al., 2007) and the initial cross-section to observed breaches and observations of storm intensities (Hosseini et al., 2016; Andringa, 2017).

This enables us to perform a Monte Carlo analysis consisting of $n = 500$ individual simulations with unique initial conditions and randomly forced storm-induce breaches. Finally, the parameters that are used in the stochastic shell are varied to mimic the impact of climate change on storm climate (Intergovernmental Panel on Climate Change, 2013).

Research question 3: Storm surges in the Western Dutch Wadden Sea

To answer the third research question, the historical model developed by H.A. Lorentz is extended to account for time-varying storm surges (State Committee on the Zuiderzee, 1926). In this model the Western Dutch Wadden Sea is represented as a network of channels, reflecting the channel shoal topography of the area and that most water flows through the channels instead of over the shoals. The State Committee studying the impact of the Afsluitdijk considered simplified storm surges in their work consisting of a equilibrium response of the water to a time-invariant wind stress. This simplification was necessitated due to the

lack of computational possibilities in the early 20^{th} century.

In this chapter we first developed a computer version of this historical model, based on their mathematical descriptions, and secondly extended the model to account for time-varying storm surges. This was done by applying a Fourier transformation to the governing equations, boundary conditions, and wind forcing.

Using this model we studied the effect of basin geometry and storm characteristics on the characteristics of the storm surge.

Chapter 2: The influence of backbarrier basin geometry on multiple tidal inlet systems: the role of resonance and bottom friction

Abstract

Observations of barrier coasts around the world suggest that some systems do not conform to the O'Brien-Jarret law. Here we explain this by investigating how resonance and bottom friction affect the response of tidal inlets to variations in basin geometry. Therefore, we develop a morphodynamic barrier coast model that is based on the stability concept of Escoffier for the morphological evolution of the inlets, coupled with an idealized hydrodynamic model that describes the water motion in the outer sea, inlets and arbitrarily shaped backbarrier basin. We find that the total tidal prism through all inlets is predominantly determined by the (cross-shore) width of the basin and identify three regimes for this. First, a linear regime for narrow basins (i.e. basin width $\ll$ tidal wavelength) where a larger basin leads to a linear increase in total tidal prism. Second, a resonant regime for basins with a width around the resonant condition in which the total tidal prism reaches a peak. This resonance condition is a quarter tidal wavelength for basins without friction, which shifts to narrower basins as friction becomes stronger, down to 0.15 tidal wavelength. Third, a dissipative regime for wide basins (i.e. the cross-shore basin dimension or basin width $\gg$ resonant condition) with sufficiently strong bottom friction in which the total tidal prism does not change for wider basins, because the tidal wave completely dissipates in the basin.

This chapter has been published as: Reef, K. R. G., P. C. Roos, H. M. Schuttelaars, and S. J. M. H. Hulscher (2020a). "Influence of Back-Barrier Basin Geometry on Multiple Tidal Inlet Systems: The Roles of Resonance and Bottom Friction". In: *Journal of Geophysical Research: Earth Surface* 125.3. DOI: 10.1029/2019JF005261.

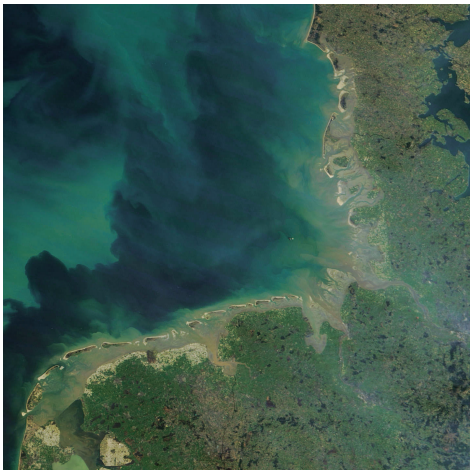

Figure 2.1: Satellite image of a barrier coast, showing the Dutch, German, and Danish Wadden Sea. Image adapted from NASA.

2.1. Introduction

Barrier coasts, covering around 10% of the worldwide coastline (Glaeser, 1978; Stutz and Pilkey, 2011), are often found near densely populated areas. They are important for their economic, ecologic, touristic value; and as protection of the mainland coast (e.g. Oost et al., 2012; Wang et al., 2012). The morphology of barrier coasts changes continuously under the influence of tides, waves, and storms (e.g. Escoffier, 1940; De Swart and Zimmerman, 2009), making them dynamic systems. Following Davis and Hayes (1984) barrier coasts are typically categorized according to the relative dominance of either tides (macro-tidal) or waves (micro-tidal), or equal importance of tides and waves (meso-tidal); this study focusses on the latter two.

An important aspect in the natural evolution of barrier coasts is the evolution of tidal inlets since they are the link between the backbarrier basin and the outer sea. Already in the early 20th century the tidal prism of an inlet was linked to the size of tidal basins, where an almost linear response was observed to differences in basin size between tidal inlets in the United States of America (O'Brien, 1931; O'Brien, 1969; Jarret, 1976). While these observations showed that a larger tidal basin corresponds to a larger tidal prism (for the same tidal range), the opposite was observed in the Western Dutch Wadden Sea (see Fig. 2.1) after a large bay was closed off, the Zuiderzee in 1932 (e.g. Kragtwijk et al., 2004; Elias et al., 2012). After this closure, the basin width (i.e. cross-shore dimension) was reduced by approximately 60 km; which led to an increase in inlet cross-section

for the inlets closest to the intervention (e.g. Elias et al., 2012). One suggested explanation (Elias et al., 2012) for this is the shift from a (cross-shore) basin width close to half the tidal wavelength to a basin width closer to quarter wavelength at which resonance occurs (e.g. in the Bay of Fundy). Another example is the Pamlico Sound (NC, USA) where a large backbarrier basin is connected to the outer sea by just three tidal inlets.

The above illustrates that while we have some understanding of how the equilibrium configuration (i.e. size and spacing) of tidal inlets is affected by spatial variations in cross-shore basin geometry; the underlying mechanisms are still not fully understood. The goal of this study is to better explain how tidal inlets are affected by variations in cross-shore basin geometry and specifically how this is affected by resonance and bottom friction. In particular we aim to answer the following questions:

- How does the cross-shore geometry of the back-barrier basin affect the equilibrium configuration of multiple inlets connected to one backbarrier basin?
- What is the effect of a reduction of the (cross-shore) basin width (e.g. due to human interventions such as damming or land reclamation) on the equilibrium configuration of multiple inlets connected to one backbarrier basin?

To answer our research questions we extend the idealized barrier coast model of Roos et al. (2013) to allow backbarrier basins of arbitrary shape. We choose an idealized model because it allows us to study the processes affecting multiple inlet systems in isolation and enables us to perform extensive sensitivity analyses. This extension allows us to simulate barrier coast systems with a backbarrier basin of arbitrary plan-view shape, instead of only a single rectangular basin as the model of Roos et al. (2013). Furthermore, the solution method employed results in low computational costs, making this model well suited to cope with the large spatiotemporal scales involved. This choice also allows us to examine a large set of initial inlet conditions, which is essential because initial conditions have been shown to have a large impact on the equilibrium configuration of tidal inlets in process-based models (Dastgheib et al., 2008).

This paper is organized as follows: the model is described in §2.2.1 and the solution method in §2.2.2. The results are presented in §2.3, the discussion in §2.4, followed by the conclusions in §2.5.

2.2. Model & Methods

2.2.1 Model Formulation

2.2.1.1 Model Description and Geometry

In our idealized model the morphological evolution of the tidal inlets is governed by the stability concept of Escoffier and the water motion is described by the linearized shallow water equations, forced by a tidal wave on the outer sea. As model domain, we consider a simplified barrier coast consisting of a semi-infinite outer sea bordering a straight coast, interrupted by a set of J tidal inlets that connect the outer sea to an arbitrarily shaped tidal basin (Fig. 2.2) with surface area A_b. Each inlet j is assumed to have a rectangular cross-section, with width b_j and depth h_j. The shape of the inlet is fixed using a constant shape factor $\gamma^2 = h_j/b_j$, (e.g. De Swart and Zimmerman, 2009). This implies

$$A_j = b_j h_j = b_j^2 \gamma^2. \tag{2.1}$$

The domains used in this study are schematizations of two real-world barrier coast systems. The first is a schematization of the Western Dutch Wadden Sea (see Figure 2.2 top row) consisting of a narrow and wide part (i.e. the top and bottom part in panel b of Figure 2.2, respectively). The width of this wide part will be varied later on in our analysis. The second is a schematization of the Pamlico Sound, North Carolina (see Figure 2.2 bottom row), ranging from Cape Lookout to Cape Hatteras and including parts of the Neuss and Pamlico estuaries. The parameter values corresponding to these domains, one set for the Western Dutch Wadden Sea and one for the Pamlico Sound, are given in Table 2.1.

2.2.1.2 Morphodynamics

For meso-tidal barrier coasts, both tides and waves are important for the morphological evolution of the tidal inlets (Davis and Hayes, 1984). The tides export sediment from inlet channels leading to erosion, whereas wave-induced littoral drift imports sediment into the inlet channel leading to accretion. Escoffier (1940) argued that an inlet is in equilibrium if the erosion due to the tides and the accretion due to waves balance each other.

In the approach of Escoffier (1940) the sediment export, denoted by X, is modelled as a function of the tidal velocity amplitude U in the inlet. The sediment import denoted by M is parameterized as a function of the equilibrium velocity U_{eq}. If $U < U_{eq}$ the inlet accretes, if $U = U_{eq}$ the inlet is in equilibrium, and if $U > U_{eq}$ it erodes. Using this concept and a simple hydrodynamic model with a spatially uniform water level in the basin, Escoffier (1940) found

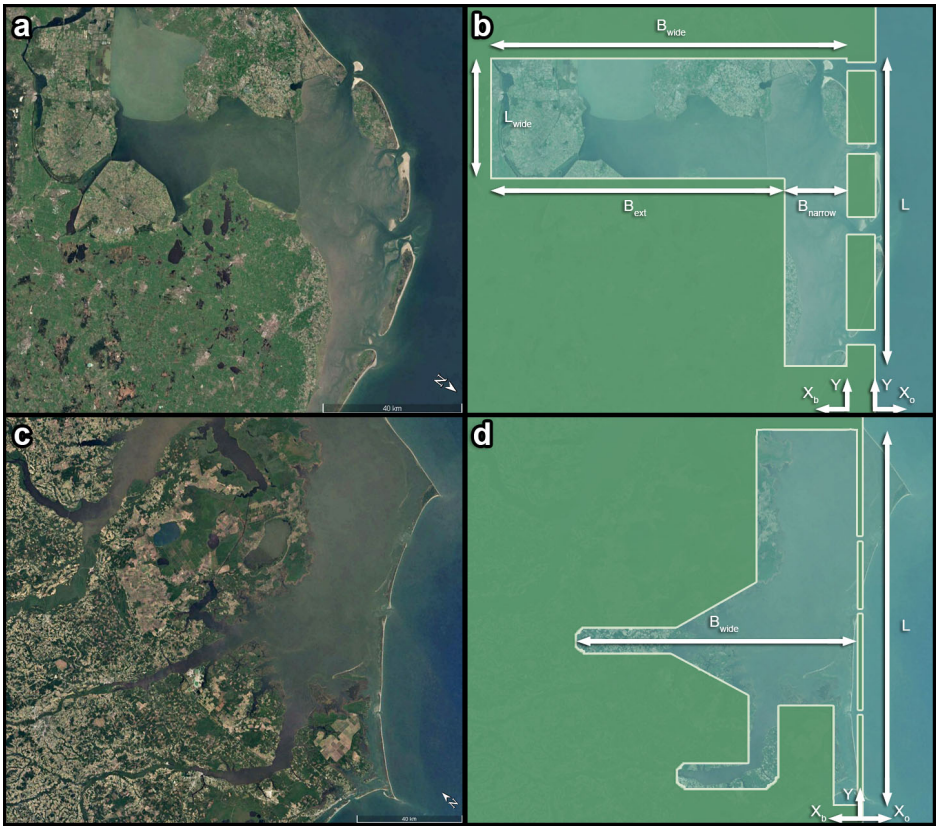

Figure 2.2: Top row: Satellite image (panel a; Google (2016)) and basin schematization (panel b) for the Western Dutch Wadden Sea. Bottom row: Satellite image (panel c; Google (2016)) and basin schematization (panel d) for the Pamlico Sound (NC, USA). In the left column a length scale and north arrow are provided for reference. In the right column shown in blue from left to right, are the tidal basin (with a wide and narrow part), the tidal inlets, and the outer sea. Shown in green is the mainland and the barrier islands. Key dimensions such as the (long-shore) basin length L and (cross-shore) basin width B are provided for the entire basin, and for different parts of the Wadden Sea basin. The positive x and y direction for both the basin (x_b & y) and the outer sea (x_o & y) are indicated as well.

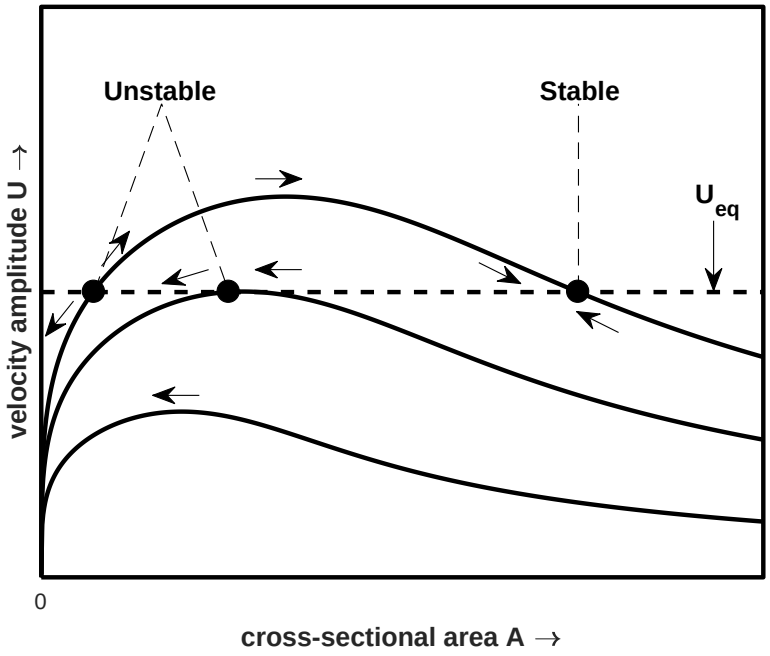

Figure 2.3: Three closure curves for a single inlet, as presented by Escoffier (1940). Each closure curve shows the inlet's velocity amplitude U as a function of inlet area A. Intersection with an equilibrium velocity U_{eq} (i.e. at $U = U_{eq}$) yields zero, one or two equilibria. Two equilibria are found if $U > U_{eq}$ for some A, one is found if both coincide and none are found if $U < U_{eq}$ for all A. In the case of two equilibria one is stable and one is unstable.

so-called closure curves describing the potential evolution of a single inlet system (Fig. 2.3). Using these closure curves it is found that either two equilibria (one stable and one unstable), one equilibrium, or no equilibrium at all exists. An equilibrium is stable if after a perturbation of the inlet cross section, it returns to its equilibrium size. More recently, process-based support for this stability concept was provided using complex numerical models (Tran et al., 2012; Nahon et al., 2012).

Escoffier's concept forms the basis of our morphodynamic model governing the evolution of the inlet cross-sections. The time evolution of the cross-sectional area A_j of each inlet j is controlled by the volumetric import M (assumed equal

for all inlets) and export X_j of sediment that is assumed to be spatially uniform

$$l_j \frac{dA_j}{dt} = X_j - M, \tag{2.2}$$

with l_j the length of inlet j. The tide-driven export X_j is taken to be proportional to the tidal velocity amplitude in the inlet U_j cubed: $X_j = \kappa U_j^3$, with κ a constant. The wave-driven import M is externally imposed and similar to previous studies (Van de Kreeke, 2004; Van de Kreeke et al., 2008; Roos et al., 2013) assumed identical for all inlets, implying that all necessary sediment can be supplied by the wave-induced longshore drift. This results in an effective equilibrium velocity U_{eq} by defining $M = \kappa U_{eq}^3$. Eq. (2.2) is then rewritten as:

$$\frac{dA_j}{dt} = \frac{M}{l_j}\left[\left(\frac{U_j}{U_{eq}}\right)^3 - 1\right]. \tag{2.3}$$

From this equation we can compute the change in cross-sectional area, given the velocity amplitude U_j in the inlet. To find U_j, we use a hydrodynamic model that is in part solved analytically and in part numerically. This hydrodynamic model is presented in the next subsection.

2.2.1.3 Hydrodynamics

The hydrodynamic model simulates the water motion in the outer sea, the tidal inlets, and the tidal basin. It is forced by an M_2-tidal wave in the outer sea resulting in a flow of water through the inlets, which in turn triggers oscillations in the back-barrier basin and in the outer sea. On the coastline of the outer sea, and on the basin boundaries a no-flow boundary condition is prescribed.

To describe the water motion in each inlet j, we consider the linearized cross-sectionally averaged momentum equation, with u_j the cross-sectionally averaged flow velocity that is uniform over the channel length. Furthermore, assuming a constant surface gradient in the inlet, the momentum equation reduces to

$$\frac{\partial u_j}{\partial t} + \frac{r_j u_j}{h_j} = -g\frac{\langle \eta_o \rangle_j - \langle \eta_b \rangle_j}{l_j}, \tag{2.4}$$

with h_j the inlet depth, η_o the water level in the outer sea (denoted by subscript o), and η_b the water level in the tidal basin (denoted by subscript b). The angle brackets denote averaging over the width of a tidal inlet j, located at either $x_o = 0$ or $x_b = 0$ and defined as $\langle \eta_o \rangle_j = b_j^{-1} \int_{y_j - b_j/2}^{y_j + b_j/2} \eta_o(0, y)\, dy$, with y_j the centre location of inlet j. Here x_b is the x-direction in the basin (with $x_b = 0$ at the basin side of the inlet) and x_o the x-direction in the outer sea (with $x_o = 0$ at the outer sea side of the inlet); both are shown in Figure 2.2, together with

the y-direction that is the same for the basin and outer sea. Furthermore, in Eq. (2.4) the coefficient r_j is a linearized bottom friction coefficient following from Lorentz' linearization (Lorentz, 1922):

$$r_j = \frac{8}{3\pi} c_d U_j, \tag{2.5}$$

with drag coefficient c_d and velocity scale U_j (see §2.2.2.2). The pressure gradient over the inlet channel (ρ times the r.h.s. of Eq. (2.4)) is due to the difference in elevation between the outer sea $\langle \eta_o \rangle_j$ and the basin $\langle \eta_b \rangle_j$, both averaged over the inlet width, with $g = 9.81$ m s^{-2} the gravitational acceleration.

Since our model equations are linearized, the elevation at the open sea $\eta_o(t, x_o, y)$ can be decomposed in an elevation related to the incoming tidal wave (i.e. $Z \cos(\omega t + k_t y)$, the tidal elevation that forces the entire system) and contributions from each inlet $\eta_{o,j}(t, x_o, y)$ due to radiating waves

$$\eta_o(t, x_o, y) = Z \cos(\omega t + k_t y) + \sum_{j=1}^{J} \eta_{o,j}(t, x_o, y), \tag{2.6}$$

with k_t the longshore component of the wave number of the incoming tide and ω the angular/radian frequency of the tide. The elevation in the basin $\eta_b(t, x_b, y)$ is the superposition (again allowed because of linearity) of oscillations $\eta_{b,j}(t, x_b, y)$ due to water flowing through all inlets:

$$\eta_b(t, x_b, y) = \sum_{j=1}^{J} \eta_{b,j}(t, x_b, y). \tag{2.7}$$

Since the water depth in the outer sea is large and the influence of Coriolis acceleration on the cross-sectional stability of tidal inlets is small (Brouwer et al., 2013), we neglect bottom friction and Coriolis acceleration. The resulting linearized depth-averaged shallow water equations read

$$\frac{\partial \mathbf{u}_o}{\partial t} = -g \nabla \eta_o, \qquad \frac{\partial \eta_o}{\partial t} + h_o (\nabla \cdot \mathbf{u}_o) = 0, \tag{2.8a,b}$$

with h_o the outer sea depth (assumed to be spatially uniform and constant in time), $\nabla = (\partial/\partial x_o, \partial/\partial y)$, and $\mathbf{u}_o = (u_o, v_o)$ the depth-averaged flow velocity with components in the x_o-direction and y-direction, that are indicated in Fig. 2.2. At the outer sea's closed boundaries (i.e. where no inlets are present), we require the normal velocity to vanish, i.e.

$$u_o = 0, \text{ so } \frac{\partial \eta_o}{\partial x_o} = 0, \quad \text{at } x_o = 0. \tag{2.9}$$

Furthermore, we only allow radiating waves propagating away from the inlets.

In the basin we include the effect of bottom friction, as the basin is much shallower than the outer sea, but we still neglect Coriolis acceleration. The resulting linearized system of equations reads:

$$\frac{\partial \mathbf{u}_b}{\partial t} + \frac{r_b \mathbf{u}_b}{h_b} = -g\boldsymbol{\nabla}\eta_b, \qquad \frac{\partial \eta_b}{\partial t} + h_b(\boldsymbol{\nabla} \cdot \mathbf{u}_b) = 0, \tag{2.10a,b}$$

with h_b the basin depth (assumed to be spatially uniform and constant in time), $\boldsymbol{\nabla} = (\partial/\partial x_b, \partial/\partial y)$, and $\mathbf{u}_b = (u_b, v_b)$ the depth-averaged flow velocity with components in the x_b-direction (u_b) and y-direction (v_b). The linearized friction coefficient r_b according to Lorentz' linearization (Lorentz, 1922) is

$$r_b = \frac{8}{3\pi} c_d U_b, \tag{2.11}$$

with U_b the velocity scale in the basin (see §2.2.2.2). At the closed boundaries of the tidal basin (i.e. where no inlets are present), we require the normal velocity to vanish

$$\mathbf{u}_b \cdot \mathbf{n} = 0 \text{ so } \boldsymbol{\nabla}\eta_b \cdot \mathbf{n} = 0, \quad \text{at} \quad \partial\Omega, \tag{2.12}$$

with $\mathbf{n}$ the normal vector at the coastline $\partial\Omega$ where no inlets are present. Finally, at the tidal inlets we require the transport of water through each inlet j to match the transport of water in the adjacent sea and basin, i.e.

$$h_o\langle u_o\rangle_j = h_j u_j = h_b\langle u_b\rangle_j, \text{ for } j \in [1, J] \tag{2.13}$$

where the angle brackets again denote averaging over the width of a tidal inlet j.

2.2.2 Outline of Solution Method

In this section we present an outline of the solution method for both the morphodynamic and the hydrodynamic part of the model. The former is solved using a forward Euler discretization of Eq. (2.3), with timestep Δt (given in Table 2.1). The latter is solved analytically – except for the eigenfunctions in the basin that are found numerically (see Appendices 2.A and 2.B) – and yields flow velocities and water levels in the outer sea, tidal inlets and basin.

The hydrodynamic part of the model is solved as follows. We first express the variables as a product of a complex amplitude and a time-periodic factor. Next, we express both the water motions in the basin and those in the outer sea in terms of the flow velocities in all inlets (see Appendix 2.A). Combinding this with the momentum equation for each inlet yields a system of linear equations for the velocity amplitudes in the inlets. This system of equations is solved

numerically using standard techniques.

2.2.2.1 Expansion of Variables

We first express both the water levels and flow velocities as the product of complex amplitudes (denoted by a hat) and a time-periodic factor

$$(\eta_o, u_o, v_o) = \Re\{(\hat{\eta}_o, \hat{u}_o, \hat{v}_o)\exp(i\omega t)\}, \tag{2.14}$$
$$(\eta_b, u_b, v_b) = \Re\{(\hat{\eta}_b, \hat{u}_b, \hat{v}_b)\exp(i\omega t)\}, \tag{2.15}$$
$$u_j = \Re\left\{\hat{u}_j \exp(i\omega t)\right\}. \tag{2.16}$$

Here, $\Re$ means taking the real part and ω is the tidal frequency already introduced in §2.2.1.3. Next, by substituting Eqs. (2.14) - (2.16) in Eqs. (2.6) and (2.7), the momentum equation (Eq. (2.4)) for an inlet j_a can be written as

$$i\omega\mu_{j_a}^2 \hat{u}_{j_a} = -\frac{g}{l_{j_a}}\left[\underbrace{Z\langle\exp(ik_o y)\rangle_{j_a}}_{\text{(I)}} + \underbrace{\left\langle\sum_{j_s=1}^{J}\hat{\eta}_{o,j_s}\right\rangle_{j_a}}_{\text{(II)}} - \underbrace{\left\langle\sum_{j_s=1}^{J}\hat{\eta}_{b,j_s}\right\rangle_{j_a}}_{\text{(III)}}\right], \tag{2.17}$$

with $\mu_{j_a}^2 = 1 - ir_{j_a}/(\omega h_{j_a})$ the frictional correction factor. Eq. (2.17) shows that the flow of water through inlet j_a, $\hat{u}_{j_a}$, is affected by all inlets j_s. There are three contributions to $\hat{u}_{j_a}$: one is related to the tidal elevation in the outer sea due to the forced tidal wave (term I), the 2nd contribution is related to waves radiating from the tidal inlets resulting in an additional sea surface elevation at the inlets (term II), and the 3rd contribution is due to the oscillating water level in the basin (term III).

To calculate the velocity amplitudes in the inlet, given the tidal wave characteristics, we express the latter two surface elevation contributions (i.e. terms II and III) in terms of $\hat{u}_{j_s}$. To this end we use the so-called sea impedance coefficients z_{o,j_s,j_a} and basin impedance coefficients z_{b,j_s,j_a} , that follow from the model equations (i.e. Eqs. 2.10a,b). These coefficients provide a relation between the surface elevation amplitude experienced by inlet j_a due to a flow of water through inlet j_s

$$\left\langle\hat{\eta}_{o,j_s}(0,y)\right\rangle_{j_a} = z_{o,j_s,j_a}\hat{u}_{j_s}, \qquad \left\langle\hat{\eta}_{b,j_s}(0,y)\right\rangle_{j_a} = z_{b,j_s,j_a}\hat{u}_{j_s}, \tag{2.18a,b}$$

where explicit expressions for the basin impedance coefficients z_{b,j_s,j_a} and sea impedance coefficients z_{o,j_s,j_a} are given in Appendix 2.A. Substituting these ex-

pression in Eq.(2.17) yields

$$i\omega\mu_{j_a}^2\hat{u}_{j_a} = -\frac{g}{l_{j_a}}\left[Z\langle\exp(ik_o y)\rangle_{j_a} + \sum_{j_s=1}^{J} z_{o,j_s,j_a}\hat{u}_{j_s} - \sum_{j_s=1}^{J} z_{b,j_s,j_a}\hat{u}_{j_s}\right], \tag{2.19}$$

resulting in a linear system of equations for the velocity amplitudes $\hat{u}_j$ that is solved numerically using standard techniques.

2.2.2.2 Velocity Scales for the Friction Formulation

The velocity scales U_b and U_j, as used in the friction coefficients r_b and r_j (Eq. 2.5 and 2.11), and defined as

$$U_b = \sqrt{\frac{1}{A_b}\iint_{A_b}\left(|\hat{u}_b|^2 + |\hat{v}_b|^2\right)dx_b\,dy} \text{ and } U_j = |\hat{u}_j|. \tag{2.20}$$

will be determined iteratively since they are both model input and output. First, an initial guess is used as input. Next, the velocity scales are updated iteratively by applying an underrelaxation procedure until the relative difference between the two is below an error tolerance threshold of 10^{-10}.

2.2.3 Design of model experiments

2.2.3.1 Single Simulation

In each simulation, we start with a so-called over-saturated coast containing J_{init} equidistantly spaced tidal inlets and simulate the morphologic evolution of the inlets. We slightly randomize the initial width (up to $\pm 10\%$ from the value in Table 2.1) of all tidal inlets in each simulation, allowing for possible different equilibrium configurations to be found. The simulation spans 1,000 years, a period that is large enough for the system to reach an equilibrium (or near-equilibrium) configuration. The model results consist of the inlet cross-sections A_j; the tidal elevation amplitude in the basin $\hat{\eta}_b$ and outer sea $\hat{\eta}_o$; and the tidal velocity amplitude in the basin $\mathbf{u}_b$, inlet $\hat{u}_j$, and outer sea $\mathbf{u}_o$.

To demonstrate that our model is capable of simulating various barrier coast systems we perform three representative model runs, two for Wadden Sea parameters and one for Pamlico Sound parameters (see Table 2.1). For the Wadden Sea parameters, we consider both the present-day system in which $B_w = 30$ km and the former system (i.e. pre-closure) in which $B_w = 120$ km. Since the Western Dutch Wadden Sea is a meso-tidal barrier coast with drumstick shape barrier islands and four tidal inlets (although up to 10 have been open in the last two millennia, see Vos and Knol (2015)), we expect our model to simulate multiple

Table 2.1: Parameters used in this study.

Parameter	Symbol (unit)	Wadden Sea	Pamlico Sound
Tidal Elevation Amplitude in sea	Z (m)	1	0.325
Tidal Frequency in sea	ω (rad/s)	1.405×10^{-4}	1.405×10^{-4}
Longshore Tidal Wave Number	k_t (rad/m)	0	0
Basin Depth	h_b (m)	5	4
Basin Length*	L (km)	75	135
Wide part Basin Length*	L_w (km)	30	100
Wide part Basin Width†	B_w (km)	20 - 120	-
Narrow part Basin Width†	B_n (km)	20	-
Drag Coefficient	c_d (-)	2.5×10^{-3}	2.5×10^{-3}
Initial Inlet Depth	h_j (m)	5	5
Inlet Length	l_j (km)	5	5
Initial Inlet Width	b_j (km)	1 ± 0.1‡	1 ± 0.1‡
Inlet Shape Factor	γ^2 (-)	0.005	0.005
Number of Initial Inlets	J_{init} (-)	50	70
Outer Sea Depth	h_o (m)	20	20
Sediment Import	M (m^3/year)	1×10^6	0.59×10^6
Morphodynamic Timestep	Δt (year)	0.5	1
# of simulations in one ensemble	n (-)	100	-

*: We define Basin Length as the long-shore dimension of the basin (see Fig. 2.2).

†: We define Basin Width as the cross-shore dimension of the basin (see Fig. 2.2).

‡: The actual initial width of an inlet is randomized using a uniform distribution between 0.9 km and 1.1 km.

inlets and barrier islands with limited lengths (i.e. longshore direction). Since the Pamlico Sound is a micro-tidal barrier coast with very long and thin barrier islands and three tidal inlets (although multiple inlets have opened and closed of the past two millennia, see Mallinson et al. (2018)), we expect our model to simulate a small number of inlets and thus very long barrier islands.

2.2.3.2 Ensemble Simulation

To study the effect of basin geometry on the size and spacing of tidal inlets, we performed a sensitivity analysis by varying the basin width (i.e. the cross-shore dimension) in the Wadden Sea inspired domain (i.e. shown in the top row of Fig. 2.4). For this sensitivity analysis, we use 21 ensembles in which the width of the back-barrier basin in the wide part of the basin B_w is varied from 20 km (i.e. $B_w = B_n$) to 120 km (the maximum extent of the Western Dutch Wadden Sea before closure of the Zuiderzee). Each ensemble consists of 100 simulations, using the Wadden Sea parameters and the same set of 100 randomized inlet widths for all ensembles, to ensure that variations in equilibrium configurations are solely due to changes in basin geometry.

Two types of experiments are carried out. The first set of experiments is used to investigate to what extent the geometry in one part of the basin affects the equilibrium configuration of tidal inlets in other parts of the basin. To this end we kept the width in the narrow part of the basin B_n constant, while varying B_w. These experiments are referred to as *Fixed-geometry runs*.

The second set of experiments is used to study the effect of basin reduction on the equilibrium configuration of tidal inlets. In these experiments, we first consider a wide tidal basin ($B_w = 120\text{km}$). After 500 years (i.e. halfway the simulation) the basin width is reduced in the wide part of the basin, this reduction varies from 5 to 100 km. With this set of experiments we simulate how the equilibrium configuration of tidal inlets changes due to an intervention, instead of finding the equilibrium state that an initially oversaturated coast will reach. These experiments are referred to as *Intervention runs*.

We analyze the results of each model run by determining three metrics for the total basin (denoted by a subscript $_t$): the ratio of the inlet cross-sections and its initial size $A_j/A_{init,j}$ for all open inlets j, all in the total basin (i.e. $A_{j,all}/A_{init,j,all}$), the number of open inlets J_t, and the dimensionless total tidal prism $P_t/P_{ref,t}$, with

$$P_t = \sum_{j=1}^{J} \frac{2|\hat{u}_j|}{\omega} A_j, \quad \text{and} \quad P_{ref,t} = ZA_{\text{ref basin}}. \tag{2.21}$$

Here $A_{\text{ref basin}}$ is the basin surface area. Since we vary the basin area of the Wadden Sea basin, we choose one reference basin area $A_{\text{ref basin}}$ that is equal to the basin area of the smallest Wadden Sea basin that we consider in this study

(i.e. for which $B_w = B_n = 20$ km). Similarly, these metrics can be defined for the wide and narrow part of the Wadden Sea basin, by replacing the total quantities by quantities for the wide part of the basin ($A_{j,w}/A_{init,j,w}$, J_w, and $P_w/P_{ref,w}$ with $P_{ref,w} = ZL_wB_n$) and the narrow part of the basin ($A_{j,n}/A_{init,j,n}$, J_n, and $P_n/P_{ref,n}$ with $P_{ref,n} = Z(L - L_w)B_n$). Per ensemble we aggregate the three metrics and determine the median, 50% envelope, and 100% envelope for each basin configuration.

2.3. Results

2.3.1 Representative Model Runs

Here we present the results of three representative model runs (using both the Wadden Sea and Pamlico Sound parameters from Table 2.1). These representative model runs are individual realizations from the ensembles described in §2.2.3.2.

Figure 2.4 shows the initial configuration (panel a, d, and g), evolution (panel b, e, and h), and equilibrium configuration (panel c, f, and i) of the tidal inlets. In the present day Wadden Sea simulation (top row), the initially oversaturated barrier coast ($J_{init} = 50$) evolved into an equilibrium state where in this example only 12 inlets remain open and 38 have closed. In the former Wadden Sea simulation (middle row), the initially oversaturated barrier coast ($J_{init} = 50$) evolved into an equilibrium state where in this example only 8 inlets remained open and 42 have closed. In the Pamlico Sound simulation (bottom row), the initially oversaturated barrier coast ($J_{init} = 70$) evolved into an equilibrium state where in this example only 3 inlets remain open and 67 have closed.

Comparison of the present-day Wadden Sea example run (Fig. 2.4 top row) with the real-world system (Elias et al., 2012) reveals that our model correctly simulates a slight increase in tidal amplitude near the back of the basin. Regarding the tidal inlets, our model underestimates the inlet cross-sections, and overestimates the number of inlets that remain open, in turn leading to simulated barrier islands that are shorter than those currently present in the Western Dutch Wadden Sea. For the former Wadden Sea example run (Fig. 2.4 middle row), a comparison with observations from the past (State Committee on the Zuiderzee, 1926) show that our model correctly simulates a decrease in tidal amplitude as the basin extends further. For the former Wadden Sea domain, our model appears to predict a number of inlets and barrier island lengths that are in the same range as found in reconstructed paleographic maps (Oost et al., 2012; Vos and Knol, 2015; Haas et al., 2018). The simulated number of inlets is slightly larger than the number of inlets currently present in the Western Dutch Wadden Sea.

Comparison of the example Pamlico Sound model run (Fig. 2.4 bottom row)

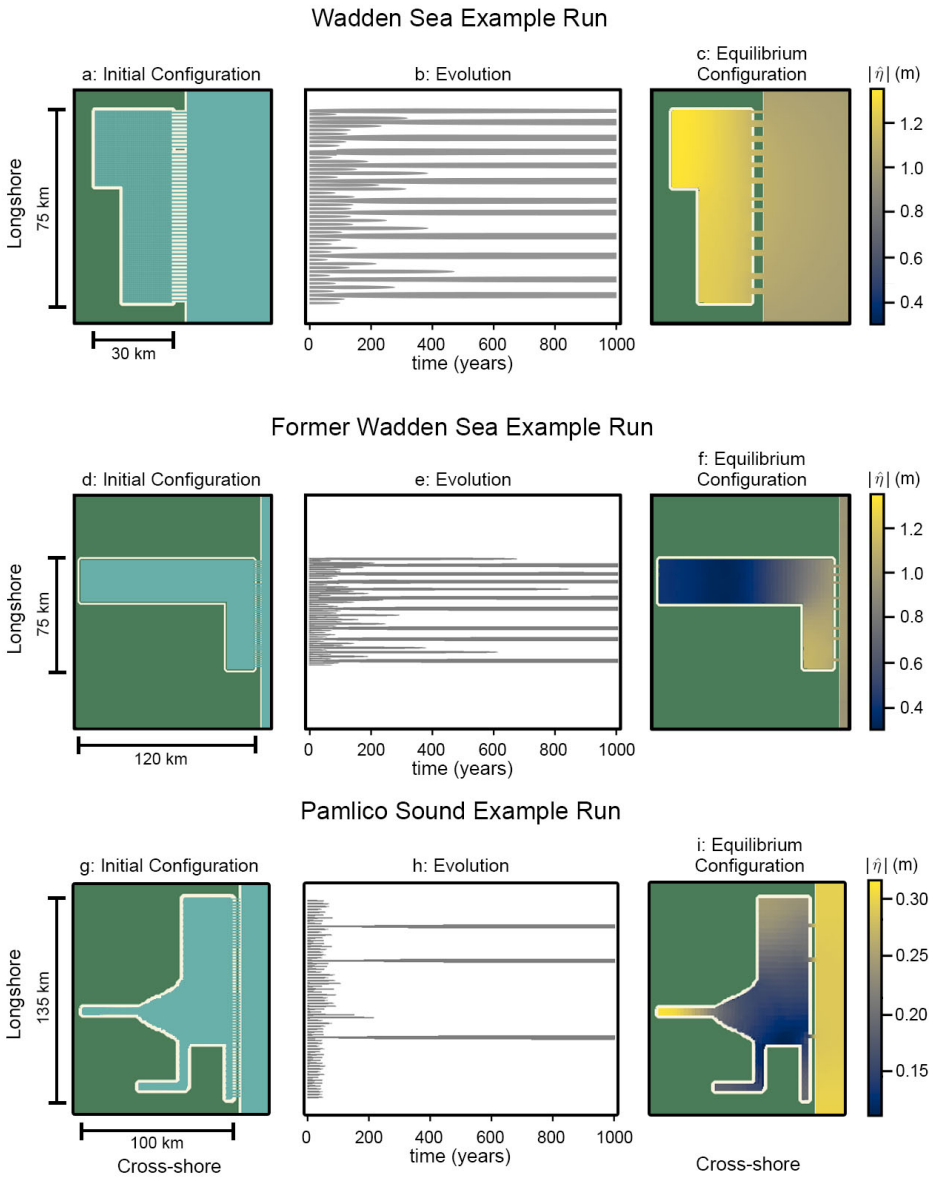

Figure 2.4: Three example runs for: the present Wadden Sea domain (top row, with B_w = 30 km), the former Wadden Sea (middle row, with B_w = 120 km), and Pamlico Sound domain (bottom row). Panel a, d, and g, show the initial over-saturated barrier coast (top view); b, e, and h, the evolution of the tidal inlets (time stack); c, f, and i, the equilibrium configuration (top view).

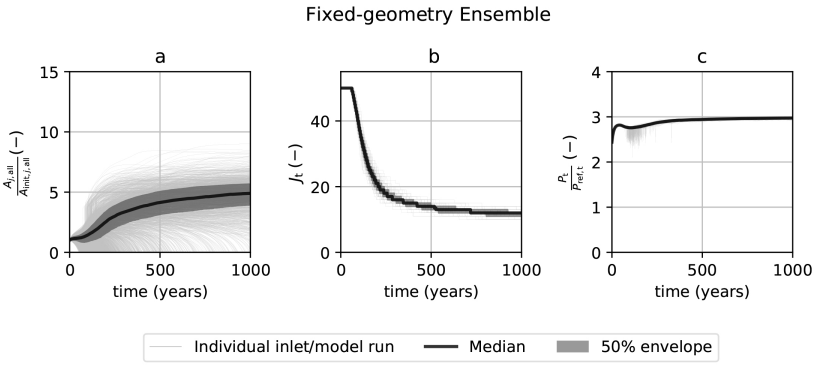

Figure 2.5: Results of a single ensemble run (for $B_w = 30$ km; i.e. the same basin as the example run) in three metrics: a, the relative inlet size $A_{j,all}/A_{init,j,all}$ of all open inlets; b, the number of inlets J_t; c, the dimensionless tidal prism $P_t/P_{ref,t}$ (see §2.2.3.1). These are plotted for the entire duration of the simulation.

with the real-world system (Inman and Dolan, 1989; United States Geological Survery, 2019; National Oceanic and Atmospheric Administration, 2020) reveals that our model correctly simulates the tidal amplitude pattern (i.e. lower in the basin and higher on the Pamlico river) and the number of inlets and barrier island lengths (although these results slightly vary for different initial conditions) but overestimates their total cross-section. Finally, the time period over which the inlets reach a stable equilibrium differs per example run. For the present-day Wadden Sea this period ranges from 100 yr to 500 yr, for the former Wadden Sea this period ranges form 100 yr to 800 yr, and for the Pamlico Sound this period ranges form 50 yr to 250 yr.

2.3.2 Fixed-geometry Runs

The experiments for the Fixed-geometry runs consist of 21 ensembles of 100 model runs each. For the ensemble corresponding to the basin of the example run where $B_w = 30$ km, the evolution of the ratio $A_{j,all}/A_{init,j,all}$ for each open inlet j in the total basin (panel a), the number of inlets J_t (panel b), and dimensionless tidal prism $P_t/P_{ref,t}$ (panel c) are shown are shown in Figure 2.5. The first panel shows that the inlets that remain open are approximately five times larger than their initial size. The second panel shows that the number of inlets reaches its equilibrium value right before the end of the simulation period. Finally, the third panel shows that the equilibrium tidal prism approaches its equilibrium faster than the inlet cross section and number of inlets. This indicates it reaching its equilibrium despite the individual inlets not having reached

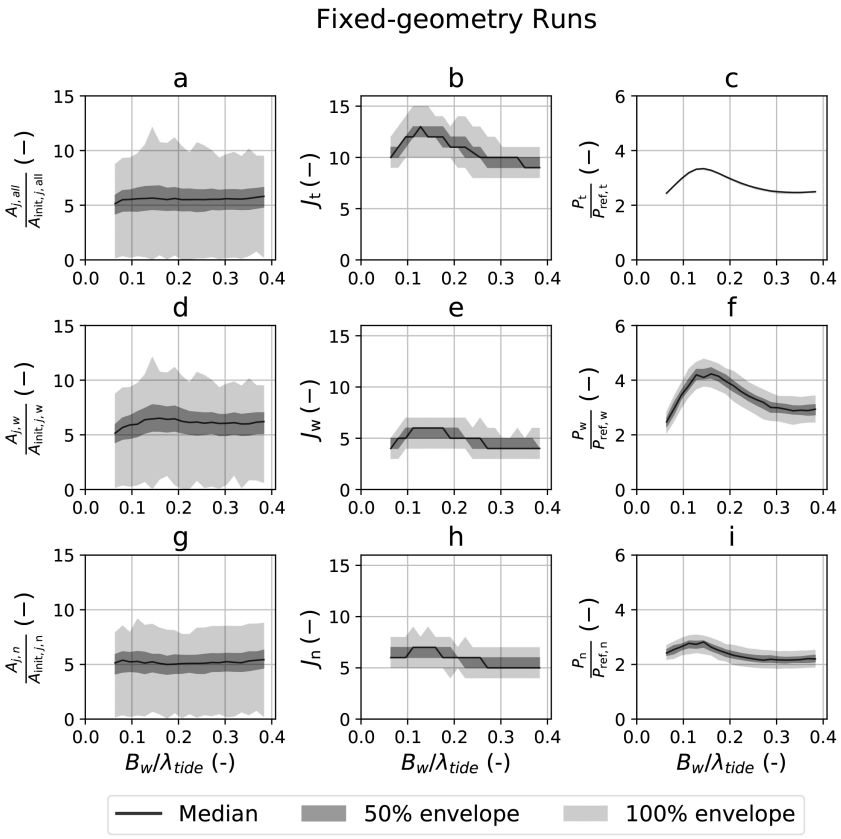

Figure 2.6: Results of end states of the Fixed-geometry runs to identify the effect of basin size on the cross-section A_j of each open inlet in all simulations, the number of inlets J, and the tidal prism P summed over all inlets. The relative inlet cross-section $A_j/A_{init,j}$ for each open inlet is shown for: a, the total basin ($A_{j,all}/A_{init,j,all}$); d, the wide part of the basin ($A_{j,w}/A_{init,j,w}$); g, and the narrow part of the basin ($A_{j,n}/A_{init,j,n}$). Similarly, the number of open inlets J and the dimensionless total tidal prism P/P_{ref}) are shown for: b & c , the total basin($P_t/P_{ref,t}$)); e & f , the wide part of the basin ($P_w/P_{ref,w}$)); h & i , and the narrow part of the basin ($P_n/P_{ref,n}$)). The basin size A_{basin} was varied by varying the (cross-shore) basin width in the wide part of the basin B_w and is plotted as a fraction of the frictionless tidal wave length λ_{tide}. The median of the ensembles (n = 100 model runs) is shown as a solid line, the envelopes around 50% and 100% of the model runs are transparent.

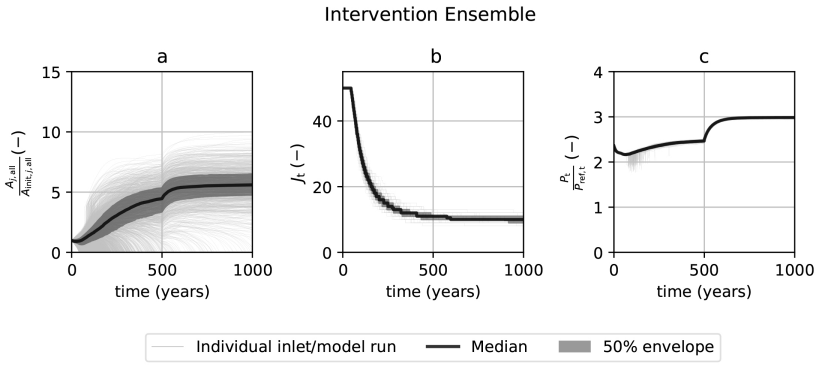

Figure 2.7: Same as Figure 2.5 , but now showing the results of an Intervention run, see §2.2.3.2.

their equilibrium.

The same three metrics are shown for the equilibrium, or, end states of the Fixed-geometry runs in Figure 2.6: for all inlets j, all in the entire basin (panels a - c), the inlets j, w in the wide part of the basin (panels d - f), and the inlets j, n in the narrow part of the basin (panels g - i). Our results show that the inlets in all parts of the basin are affected by changes in basin size. For larger basin sizes up to $B_w/\lambda_{tide} = 0.15$ (with λ_{tide} the wavenumber of the tide without friction), both the number of inlets along the backbarrier basin J_t and the total tidal prism P_t increase , with a maximum for $B_w/\lambda_{tide} \sim 0.15$. For even larger basins, both J and P decrease again until both aggregated variables reach a constant value. These results also show a large spread in inlet cross-section $A_{j,all}$ for given basin geometry, which remains more or less constant for different basin geometries. Only the cross-sections of inlets in the wide part of the basin (where the width is varied) weakly respond to variations in basin geometry, as they tend to become larger than those in the narrow part of the basin (where the width is not varied).

2.3.3 Intervention Runs

For a single ensemble experiment from the Intervention runs (corresponding to the basin of the example run where, at $t = 500$ yr, the basin width B_w is reduced from 120 km to 30 km), the temporal evolution is shown in Figure 2.7. The temporal evolution clearly shows that the system reaches an approximate equilibrium after 500 years; after the intervention the system in no longer in equilibrium anymore and evolves to a new equilibrium. This is reflected in both the relative inlet size of all open inlets $A_{j,all}/A_{init,j,all}$ and the dimensionless tidal

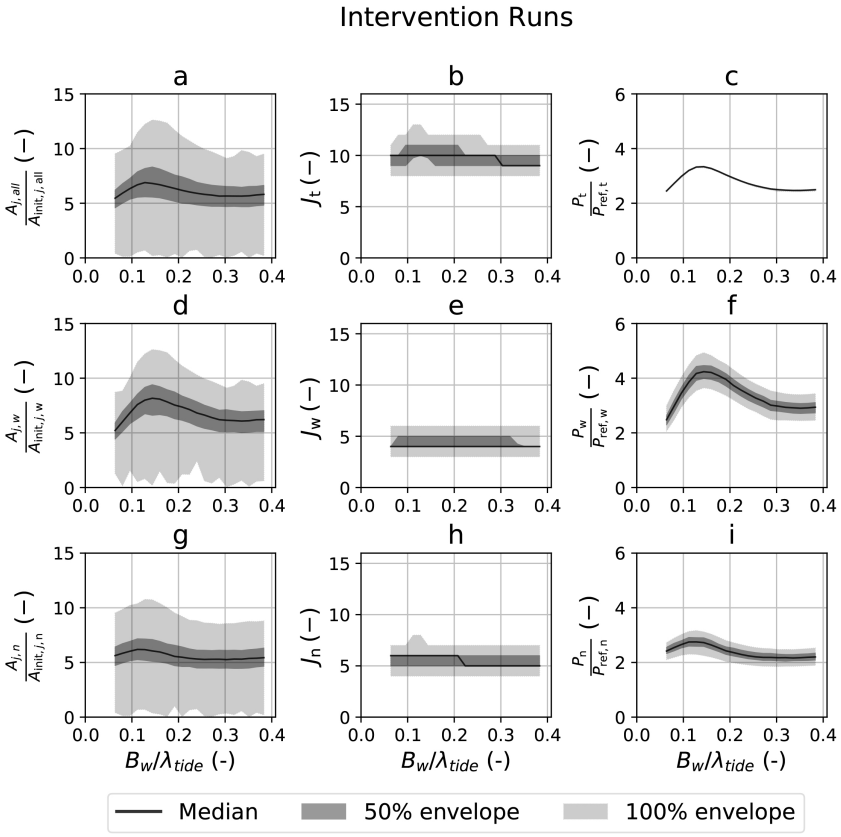

Figure 2.8: Same as Figure 2.6, but now showing the results of the Intervention runs, see §2.2.3.2.

prism $P_t/P_{ref,t}$. The only metric that appears to be unaffected is the number of inlets J_t.

The same three metrics are shown for the end states of the Intervention runs in Figure 2.8; for the total basin (panels a - c), the wide part of the basin (panels d - f), and the narrow part of the basin (panels g - i). Similar to the Fixed-geometry runs results we plotted the median, the 50% envelope and the 100% envelope. The end states of the Intervention runs show the same results for the total tidal prism P_t as the Fixed-geometry runs for the same value of B_w/λ_{tide}, but the results for the inlet cross-section $A_{j,all}$ and number of inlets J_t are different. The effect of reducing the basin width after an equilibrium has been reached is that after the intervention the number of inlets hardly varies, primarily the size of the inlets varies to compensate for a different equilibrium tidal prism. These results are discussed further in §2.4.3.

2.4. Discussion

2.4.1 The Effect of Basin Area on Tidal Prism

Our results for the total tidal prism P_t (panel c in Figures 2.6 & 2.8) show that for a multiple inlet system the tidal prism is predominantly determined by the overall basin area A_{basin} and much less by variations in (initial) inlet characteristics, as can be seen by the overlapping of the median and 50% and 100% envelopes. Further evidence for this comes from the fact that the total tidal prism for the entire basin is the same for the Fixed-geometry runs and the Intervention runs, implying that it is unaffected by the initial conditions of the tidal inlets. This also implies that the variations in the total tidal prism in the wide and narrow part of the basin are mostly due to variations in the equilibrium configuration of the tidal inlets.

Thus, the equilibrium configuration of the tidal inlets adapts to convey the total tidal prism P_t. This helps explaining the variations in tidal prism in the (unaltered) narrow part of the basin due to variations in (cross-shore) basin width in the wide part of the basin. The basin area determines the equilibrium tidal prism P_t of the system, so variations in basin area will lead to variations in P_t. In turn, the tidal inlets in the entire basin will evolve (due to inlet interaction) such that in their equilibrium configuration the entire tidal prism is conveyed by them.

For single inlet systems, the tidal prism has been observed to satisfy a linear relation with basin area (e.g. O'Brien, 1931), i.e. a *linear regime*, sometimes referred to as a *pumping mode*. This observation was also used for modelling these systems (e.g. Van de Kreeke, 1990a; Van de Kreeke, 1990b; Van Goor et al., 2003; D'Alpaos et al., 2010; Brouwer et al., 2012a). Our results for multiple inlet systems only support the occurrence of linear regimes in short basins

(i.e. $B \ll \lambda_{tide}$), but clearly indicate that this observation does not hold in longer basins where resonance can occur. Two additional regimes can be identified besides the classic linear regime, in our results on multiple inlet systems. First, a clear maximum can be seen in the total tidal prism P_t, implying a resonant regime. Second, the total tidal prism P_t becomes invariant for ever larger basins, implying a dissipative regime. In the next subsection these observations and the processes causing them are further discussed.

2.4.2 The Effect of Resonance and Bottom Friction on Tidal Prism

Our results show that the total tidal prism P_t (panel c in Figures 2.6 & 2.8) increases for an increase in basin width, and then decreases for large enough values of B_w/λ_{tide} eventually reaching a constant value; where λ_{tide} is the wavelength of the frictionless tidal wave. The relative width of the basin at which this peak happens is $B_w/\lambda_{tide} = 0.15$. This suggests this behavior is due to the well-known quarter wavelength resonance even though the maximum is found for $B_w/\lambda_{tide} < 0.25$.

To further investigate the importance of resonance, we used a 1D analytical model to study the effect of basin width B on the equilibrium cross section $A_{j,all}$ of a single tidal inlet connected to a rectangular basin (see Fig. 2.9a and Appendix 2.C). This model is forced by a tidal elevation amplitude at the seaside of the inlet (neglecting other seaside processes as Coriolis and radiative damping) and is again based on the linearized shallow water equations with a linearized friction coefficient. Using this model we compute for which inlet cross-section A_j the inlet velocity is exactly equal to the equilibrium velocity (i.e. $U = U_{eq}$). Our results in Fig. 2.9 b show that a clear resonance peak is present at $B/\lambda_{tide} = 0.25$ in case no bottom friction is present (i.e. $r_b = 0$). Stronger bottom friction (i.e. a higher value of r_b) leads to a shift of this peak towards narrower basins and a reduction of the peak. For larger basins, a constant value for the inlet cross section A_j is obtained, if bottom friction is sufficiently strong.

In narrow basins (i.e. $B \ll \lambda_{tide}$) resonance behavior does not occur, and the increase in inlet cross-section depends linearly on basin area, also referred to as linear regime, see Fig. 2.9b. Our results show that this linear regime gives way to a resonant regime around $B/\lambda_{tide} = 0.1$, or $B \sim 31$ km for the parameters in this study, although it will be lower for higher values of r_b.

Thus, the relation between basin size and tidal prism is no longer fully linear (as observed for single inlet systems; e.g. O'Brien (1931)), if the basin is sufficiently wide.

For wider basins with sufficient friction, the resonant regime gives way to

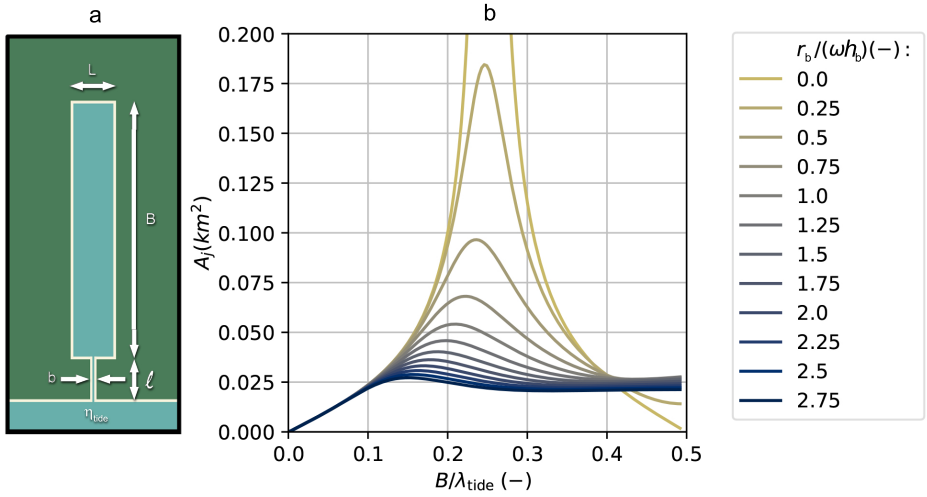

Figure 2.9: a: model geometry for our 1D model to study the effect of resonance and bottom friction on the equilibrium cross section A_j of a single tidal inlet. b: results of our 1D model showing different resonant responses in the inlet cross-section A_j for different (cross-shore) basin widths B/λ_{tide} and different values of the dimensionless friction coefficient $r_b/(\omega H)$. N.B. λ_{tide} refers to the tidal wavelength without friction.

a dissipative regime with constant inlet cross section A_j for increasing basin widths. Strong bottom friction causes the inlet cross-section A_j to reach a constant value with only a small resonance peak; weak bottom friction leads to a distinct resonance peak, before also reaching a constant value. This implies that the tidal wave completely dissipates in the basin and that increasing the basin width further has no effect on the water motion inside the basin and hence on the inlet cross-section. Thus a very wide basin can be accompanied by few/small tidal inlets, as can be observed in the wide and shallow Pamlico Sound behind the Outer Banks of North Caroline, U.S.A (e.g. Inman and Dolan, 1989; Luettich et al., 2002).

2.4.3 The Effect of Basin Reduction

If a basin reduction is implemented, the geometry of the basin changes and thus the total tidal prism P_t will change as well. The results from our Intervention runs (see Fig. 2.8) show that the equilibrium configuration of the inlets indeed adapts to the new basin geometry and a new equilibrium total tidal prism is reached that is not noticeable different from that reached in the Fixed-geometry runs for the same basin geometry. However, because only a limited number of inlets are open when the basin geometry is changed the change in tidal prism has to be accommodated by changes in the inlet cross sections. This closely mimics the situation in most barrier coast systems that are actively managed. In most of these systems new inlets are not allowed to open.

This implies that a significant reduction of basin width could lead to a regime shift from a constant to resonant regime or from a resonant to a linear regime. Thus a decrease in basin width could lead to an increase in tidal prism and inlet cross-sections. This has indeed been observed in the Western Dutch Wadden Sea, where a large bay (the former Zuiderzee) was separated from the main basin by a dam, resulting in a basin width reduction from ~ 115 km to ~ 30 km. The tidal inlets in the wide part of the basin grew in size because the basin width moved closer to a resonant state (e.g. Elias et al., 2012).

2.4.4 Model Validity and Limitations

To assess the performance of our model we compare the model results with the real-word systems that inspired our domain and parameter choices: the Wadden Sea and Pamlico Sound. Comparison of the example runs with the real world systems (see §2.3.1) revealed that our model is capable of qualitatively reproducing observed phenomena. Our Fixed Geometry runs (§2.3.2) show that for basins narrower than the resonant condition (i.e. $B_w \ll \lambda_{tide}$) a larger basin generally corresponds to more and larger inlets (per km barrier coast), agreeing with observations (Davis and Hayes, 1984; Stutz and Pilkey, 2011). Further-

more, our Intervention runs (§2.3.3) agree with observations from the Western Dutch Wadden Sea. Closure of a large bay significantly reduced the basin width from $B_w \approx 0.4\lambda_{tide}$ to $B_w \approx 0.1\lambda_{tide}$, brings the system closer to resonance. This has led to larger inlets and an increased tidal prism (Elias et al., 2003), as shown by our model results.

By basing the evolution of tidal inlets on the stability concept of Escoffier (1940) and coupling that with an idealized hydrodynamic model accounting for tidal oscilations under the influence of bottom friction and resonance; we were able to get a good qualitative comparison between our model results and the observations. To improve this comparison, one has to extend the model by including morphological features and processes neglected in this study. Previous studies have noted the importance of morphological features such as tidal divides (Van de Kreeke et al., 2008; De Swart and Volp, 2012), channel networks (Kragtwijk et al., 2004; Reef et al., 2018), ebb and flood deltas (Gerritsen and Dunsbergen, 1998; Elias et al., 2012), and the formation of new tidal inlets through storm-induced breaching of barrier islands (Sallenger, 2000; Kraus et al., 2002). It has also been suggested that processes such as the morphological evolution in the basin and outer sea (Kragtwijk et al., 2004; Elias et al., 2012), nonlinear hydrodynamics (Salles et al., 2005), residual transport (Duran-Matute et al., 2014; Sassi et al., 2015), and changes in boundary conditions due to climate change such as sea level rise and changes in longshore drift (Glaeser, 1978; Stutz and Pilkey, 2011) affect the long-term evolution of barrier coast systems as well.

2.5. Conclusions

We studied the effect of basin geometry and (cross-shore) basin width reduction on the long-term evolution and equilibrium configuration of tidal inlets in a meso-tidal barrier coast. Our newly developed model allowed us to simulate the long-term morphological evolution, from an oversaturated state to an equilibrium state, of multiple tidal inlets connected to a back-barrier basin with a non-uniform basin width. Simulations of the Western Dutch Wadden Sea and the Pamlico Sound showed that our model was able to get results that have a good agreement with observations.

Our results display a strong relation between the basin size and the total tidal prism in the basin. However, this relation is not always linear (i.e. a linear regime) as has been observed for single inlet systems with a small tidal basin. For shorter basins, the tidal prism increases approximately linearly for an increase in basin size linear regime, but after a resonance peak at $B_w/\lambda_{tide} = 0.15$ (resonant regime) the tidal prism decreases for an increase in basin size and reaches a constant value (dissipative regime), given that bottom friction is strong enough.

Furthermore, the equilibrium configuration of tidal inlets in the entire basin

is affected by the local basin geometry (and human interventions). That is for instance the case in the Wadden Sea, where the construction of the Afsluitdijk affected all inlets in the basin, also further away from the closure dam. This is caused by changes in flow patterns in the basin and outer sea, in turn affecting inlets in the entire basin. Therefore, it is necessary to consider entire multiple inlet systems, when evaluating the effects of basin geometry or land reclamation on barrier coast systems.

Acknowledgements

This research was carried out within the WADSnext! project, funded by the 'Simon Stevin Meester' prize (awarded by NWO to S.J.M.H. Hulscher), Deltares, and the 4TU centre for Fluids and Solid Mechanics. The model developed for this study is available online (Reef et al., 2019). We thank three reviewers (two anonymous and Brad Murray) for their helpful comments.

2.A. Basin and Sea Impedance coefficients

2.A.1 Basin Impedance coefficients

In this subsection, we seek an expression for the basin impedance coefficients z_{b,j_s,j_a} for inlet j_a due to a flow of water in inlet j_s (see Eq. 2.18b). First, we formulate the model equations (2.10a,b) in terms of complex amplitudes $\hat{\eta}_b(x_b, y)$, the surface amplitude in the basin, and $\hat{\mathbf{u}}_b$, the velocity amplitude in the basin defined in Eq. (2.15)

$$\nabla^2\hat{\eta}_b + \mu_b^2 k_b^2 \hat{\eta}_b = 0, \qquad \hat{\mathbf{u}}_b = \frac{gi}{\mu_b^2\omega}\nabla\hat{\eta}_b, \tag{2.22a,b}$$

where $\mu_b^2 = 1 - ir_b/(\omega h_b)$ is a frictional correction factor. The basin boundary conditions that describe the exchange of water with the tidal inlets, and no exchange along the other parts of the basin (see Eq. 2.12), read

$$\frac{\partial\hat{\eta}_b}{\partial x_b} = -\frac{i\mu_b^2\omega}{g}\hat{u}_b \text{ at an inlet,} \tag{2.23}$$

$$\nabla\hat{\eta}_b \cdot \mathbf{n} = 0 \text{ at } \partial\Omega. \tag{2.24}$$

Here $\hat{\mathbf{u}}_b$ is prescribed by using Eq. (2.13) for the complex amplitudes of the velocity (i.e. $h_j\hat{u}_j = h_b\langle\hat{u}_b\rangle_j$) and assuming that exchange of water between the inlet and the basin is uniformly distributed over the inlet cross-section (i.e. $h_j\hat{u}_j = h_b\hat{u}_b$). Next, an explicit solution for $\hat{\eta}_b(x_b, y)$ can be found by using the Green's function G_b (see e.g. Sommerfeld, 1949) that describes the impact of a Dirac-type of flow over the basin boundary on the basin hydrodynamics and that solves Eq. (2.22a) and the boundary conditions in Eq. (2.23) and Eq. (2.24). This solution reads

$$\hat{\eta}_b(x_b, y) = \sum_{j=1}^{J}\int_{y_{j_s}-b_{j_s}/2}^{y_{j_s}+b_{j_s}/2}\hat{u}_b(0, y_s)G_b(x_b, y; 0, y_s)dy_s, \tag{2.25}$$

with x_s and y_s being the coordinates where the boundary condition in Eq. (2.23) is applied. The influence of one inlet on $\hat{\eta}_b(x_b, y)$ denoted by $\hat{\eta}_{b,j_s}(x_b, y)$ is given by

$$\hat{\eta}_{b,j_s}(x_b, y) = \int_{y_{j_s}-b_{j_s}/2}^{y_{j_s}+b_{j_s}/2}\hat{u}_b(0, y_s)G_b(x_b, y; 0, y_s)dy_s, \tag{2.26}$$

where Green's function G_b associated with Eq. (2.22a) and the boundary conditions in Eqs. (2.23 & 2.24) is given by (e.g. Sommerfeld, 1949; Polyanin, 2002)

$$G_b(x_b, y; x_s, y_s) = \frac{\omega \mu_b^2}{gi} \sum_{m=0}^{\infty} \frac{\psi_m(x_s, y_s)\psi_m(x_b, y)}{(\lambda_m - \lambda)\|\psi_m\|^2}, \tag{2.27}$$

with ψ_m the eigenfunctions for a closed basin, $\|...\|^2$ the L^2-norm, $\lambda = \mu_b^2 k_b^2$, and λ_m the eigenvalue associated with ψ_m. Here we assume $\lambda \neq \lambda_m$. For cases with friction, this is always the case since λ has an imaginary part and λ_m does not.

By averaging $\hat{\eta}_{b,j_s}$ over action inlet j_a and applying the matching condition in Eq. (2.13), we obtain an expression for the basin impedance z_{b,j_s,j_a} as defined in Eq. (2.18b) by

$$\langle \hat{\eta}_{b,j_s}(0, y) \rangle_{j_a} = \left[\frac{b_{j_s} h_{j_s}}{h_b} \frac{\omega \mu_b^2}{gi} \sum_{m=0}^{\infty} \frac{\langle \psi_m(0, y_s) \rangle_{j_s} \langle \psi_m(0, y) \rangle_{j_a}}{(\lambda_m - \lambda)\|\psi_m\|^2} \right] \hat{u}_{j_s} \tag{2.28}$$

$$(= z_{b,j_s,j_a} \hat{u}_{j_s}).$$

More information about the numerical procedure that is used to find the eigenfunctions ψ_m and eigenvalues λ_m is given in 2.B.

2.A.2 Sea Impedance coefficients

We seek an expression for the sea impedance coefficients z_{o,j_s,j_a} for inlet j_a due to a flow of water in inlet j_s (see Eq. 2.18a). First, we formulate the model equations (2.8a,b) in terms of complex amplitudes $\hat{\eta}_o(x_o, y)$, the surface amplitude in the outer sea, and $\hat{\mathbf{u}}_o$, the velocity amplitude in the outer sea defined in Eq. (2.14)

$$\nabla^2 \hat{\eta}_o + k_o^2 \hat{\eta}_o = 0, \qquad \hat{\mathbf{u}}_o = \frac{gi}{\omega} \nabla \hat{\eta}_o, \tag{2.29a,b}$$

with $k_o = \omega / \sqrt{g h_o}$ the shallow water wave number and $\hat{\mathbf{u}}_o = (\hat{u}_o, \hat{v}_o)$ with $\hat{u}_o$ the velocity component in x-direction and $\hat{v}_o$ the velocity component in y-direction.

At the coastal boundary where no inlets are present, we require the normal velocity to vanish. This implies

$$\hat{u}_o = 0 \text{ so } \frac{\partial \hat{\eta}_o}{\partial x} = 0, \quad \text{at} \quad \partial\Omega, \tag{2.30}$$

with $\partial\Omega$ the coastline where no inlets are present. At the tidal inlets we require the transport of water through each inlet j to match the transport of water in the adjacent sea i.e.

$$h_o \langle u_o \rangle_j = h_j u_j, \tag{2.31}$$

where the angle brackets again denote averaging over the width of a tidal inlet. Next, we consider the Green's function for the elevation amplitude contribution $\hat{\eta}_{o,j_s}$ in the outer sea that describes the impact of a Dirac-type of flow of water over the sea boundary at inlet j_s

$$\hat{\eta}_{o,j_s}(x_o, y) = \int_{y_{j_s}-b_{j_s}/2}^{y_{j_s}+b_{j_s}/2} \hat{u}_o(0y_s) G_o(x_o, y; 0, y_s) dy_s, \tag{2.32}$$

where we use the oceanic Green's function G_o given by Buchwald (1971) but without the Coriolis effect ($f = 0$). This Green's function describes the impact of a flow through the inlets over the outer sea boundary on the outer sea hydrodynamics and that solves Eq. (2.29a) with boundary conditions (Eqs. 2.30 & 2.31). This solution reads

$$G_o(x_o, y; 0, y_s) = \frac{\omega}{2g} H_0^{(2)}(k_o d), \tag{2.33}$$

with $H_0^{(2)}$ being the Hankel function of the second kind of order zero and $d = \sqrt{(x_o - x_s)^2 + (y - y_s)^2}$ the distance from inlet j_s.

Finally, we average $\hat{\eta}_{o,j_s}(x_o, y)$ over action inlets j_a and apply the matching condition in Eq. (2.31) to achieve an expression for the sea impedance z_{o,j_s,j_a} as in Eq. (2.18a)

$$\begin{aligned}
\langle \hat{\eta}_{o,j_s}(x_o, y) \rangle_{j_a} = \frac{h_{j_s} \omega b_{j_a}}{2g h_o} \Bigg[& \beta_{j_s,j_a} + \frac{2i}{\pi} \Bigg(\beta_{j_s,j_a} \frac{3}{2} - \beta_{j_s,j_a} \Gamma \\
& - \beta^{\oplus 2}_{j_s,j_a} \ln \frac{1}{2} k_o b_{j_a} \sqrt{\alpha^2_{j_s,j_a} - \beta^{\oplus 2}_{j_s,j_a}} \\
& + \beta^{\ominus 2}_{j_s,j_a} \ln \frac{1}{2} k_o b_{j_a} \sqrt{\alpha^2_{j_s,j_a} - \beta^{\ominus 2}_{j_s,j_a}} \\
& + \alpha_{j_s,j_a} \left\{ \beta^{\ominus}_{j_s,j_a} \ln \frac{\alpha_{j_s,j_a} + \beta^{\ominus}_{j_s,j_a}}{\alpha_{j_s,j_a} - \beta^{\ominus}_{j_s,j_a}} - \beta^{\oplus}_{j_s,j_a} \ln \frac{\alpha_{j_s,j_a} + \beta^{\oplus}_{j_s,j_a}}{\alpha_{j_s,j_a} - \beta^{\oplus}_{j_s,j_a}} \right\} \\
& + \alpha^2_{j_s,j_a} \ln \sqrt{\frac{\alpha^2_{j_s,j_a} - \beta^{\ominus 2}_{j_s,j_a}}{\alpha^2_{j_s,j_a} - \beta^{\oplus 2}_{j_s,j_a}}} \Bigg) \Bigg] \hat{u}_{j_s} \qquad (= z_{o,j_s,j_a} \hat{u}_{j_s}),
\end{aligned} \tag{2.34}$$

with $\beta_{j_s,j_a} = b_{j_s}/b_{j_a}$, $\alpha_{j_s,j_a} = |y_{j_a} - y_{j_s}|/b_{j_a}$, $\beta^{\oplus}_{j_s,j_a} = (\beta_{j_s,j_a} + 1)/2$, $\beta^{\ominus}_{j_s,j_a} = (\beta_{j_s,j_a} - 1)/2$, and $\Gamma = 0.57721...$ being Euler's constant. The inequality $\alpha_{j_s,j_a} > \beta^{\oplus}_{j_s,j_a}$ is satisfied since the inlets are separated by a finite distance.

The above expression concerns the cross-impedance, (i.e. $j_s \neq j_a$), the self-

impedance (i.e. $j_s = j_a$) is given by

$$\langle \hat{\eta}_{oj_s}(x_o, y) \rangle_{j_s} = \frac{h_{j_s} \omega b_{j_s}}{2gh_o} \left[1 + \frac{2i}{\pi} \left(\frac{3}{2} - \Gamma - \ln \frac{k_o b_s}{2} \right) \right] \hat{u}_{j_s} \qquad (= z_{oj_s j_s} \hat{u}_{j_s}). \tag{2.35}$$

2.B. Eigenfunctions

The eigenfunctions ψ_m in Eq. (2.27) can be found by solving the following EigenValue Problem (EVP) with reflective boundaries

$$\nabla^2 \psi_m = -\lambda_m \psi_m, \tag{2.36}$$

where λ_m are the corresponding eigenvalues. As such, there is a distinct set of eigenfunctions and corresponding eigenvalues that depends on the geometry of the basin.

For simple geometries, such as rectangular and conical basins, the eigenfunctions are easily found to be cosines and (a linear combination of) Bessel functions, respectively. For more complex geometries, as used in this study, finding the eigenfunctions and eigenvalues is not as straightforward. For a basin of arbitrarily shape, we can solve a discretized EVP of the form

$$\mathbf{A}\boldsymbol{\psi} = -\boldsymbol{\lambda}\boldsymbol{\psi}, \tag{2.37}$$

in which the $P \times P$ matrix $\mathbf{A}$ holds the discretized ∇^2 operator from Eq. (2.36) on a grid of P points, $\boldsymbol{\psi}$ holds the eigenfunctions, and $\boldsymbol{\lambda}$ holds the corresponding eigenvalues.

In this study we used a 2^{nd} order central difference scheme to discretize the ∇^2 operator from Eq. (2.36) on a grid. We used a grid in which the points are spaced using $dx = 100$ m in x-direction and $dy = 20$ m in y-direction. The resulting grid is sufficiently fine for accurate results, while not being too computationally expensive to solve the EVP. The EVP in Eq. (2.37) was solved using the ARPACK software library (Lehoucq et al., 1998) for finding a specified number of eigenvalues in large sparse matrices.

2.C. One-dimensional analytical model of a single inlet

A one-dimensional inlet-basin model is developed to further study the effects of bottom friction and basin width on the inlet cross-section. Our model consists of a narrow inlet channel that is forced by a tidal elevation η_{tide} at the sea-side and is connected to a basin with no-flow boundaries. Furthermore, all seaside

processes besides the forced tidal elevation are neglected (e.g. Coriolis, radiative damping).

The momentum balance in the inlet is given by Eq. (2.4). At the sea-side of the inlet (i.e. at $x = -l$) a tidal elevation amplitude η_{tide} is prescribed. At the interface of the inlet and the basin, the volume transport must be equal

$$u_b(0,t)\, h_b L = u_j A_j, \tag{2.38}$$

where $u_b(x,t)$ is the flow velocity in the basin, h_b the depth of the basin, L the width of the basin, u_j the flow velocity in the inlet, and A_j the inlet cross-section The model equations for the basin are given by:

$$\frac{\partial u_b}{\partial t} + \frac{r_b u_b}{h_b} = -g\frac{\partial \eta_b}{\partial x}, \qquad \frac{\partial \eta_b}{\partial t} + h_b \frac{\partial u_b}{\partial x} = 0, \tag{2.39a,b}$$

with r_b the linearized friction coefficient in the basin and $\eta_b(x,t)$ the water level in the basin. At the closed boundaries of the basin the normal flow must vanish. Since our 1D model only has a flow of water in the x-direction, the boundary condition at the closed end of the basin becomes

$$u_b(B,t) = 0. \tag{2.40}$$

Next, we formulate the model equations in terms of complex amplitudes (Z, $\hat{u}_j$, $\hat{\eta}_b$, $\hat{u}_b$) using

$$(\eta_{tide}, u_j, \eta_b, u_b) = \Re\left\{(Z, \hat{u}_j, \hat{\eta}_b, \hat{u}_b)\exp(i\omega t)\right\}, \tag{2.41}$$

where ω is again the tidal frequency. The momentum equation in the inlet now becomes

$$\left[i\omega + \frac{r_j}{h_j}\right]\hat{u}_j = -\frac{g}{l_j}(Z - \hat{\eta}_b(0)). \tag{2.42}$$

And the model equations in the basin become

$$\frac{\partial^2 \hat{u}_b}{\partial x^2} + \mu_b^2 k_b^2 \hat{u}_b = 0, \qquad \hat{\eta}_b = \frac{i h_b}{\omega}\frac{\partial \hat{u}_b}{\partial x}. \tag{2.43a,b}$$

By applying the boundary conditions (Eqs. 2.38 & 2.40), the solution in the basin is found to be

$$\hat{u}_b(x) = \left[-\frac{A_j u_j}{A_b \sin(\mu_b k_b B)}\right]\sin(\mu_b k_b [x - B]), \tag{2.44}$$

$$\hat{\eta}_b(x) = \frac{i h_b}{\omega}\left[-\frac{A_j u_j}{A_b \sin(\mu_b k_b B)}\right]\mu_b k_b \cos(\mu_b k_b [x - B]). \tag{2.45}$$

By combining Eq. (2.42) and the solution for $\hat{\eta}_b$ at $x = 0$, we find the following expression for A_j

$$A_j = A_b \left[-\frac{\mu_j^2 k_b l_j}{\mu_b} + \frac{i\omega Z}{h_b \mu_b k_b \hat{u}_j} \right] \tan(\mu_b k_b B). \tag{2.46}$$

Here, $\mu_j^2 = \left(1 - \frac{ir_j}{\omega h_j}\right)$ is a frictional correction factor that depends on the depth of the inlet, and thus on the inlet cross section (using Eq. 2.1). Since both sides of Eq. (2.46) thus depend on A_j we use an iterative underrelaxation procedure to find the inlet cross-section for given parameters, basin length $L = 5km$), and requiring the inlet velocity amplitude to equal 1 m s^{-1}. We use the Wadden Sea parameters (see Table 2.1) and a basin of length L 5 km (i.e. along-shore) and a varying width B from 0 to 155 km (i.e. cross-shore).


3

Chapter 3: The impact of storm-induced breaches on barrier coast systems subject to climate change: a stochastic modelling study

Abstract

Storms can have devastating impacts on barrier coasts causing coastal erosion, partial inundation, and possibly the breaching of barrier islands. The breaching of barrier islands provides a mechanism for the creation of new tidal inlets that connect the backbarrier basin (or lagoon) and the outer sea. As a new tidal inlet affects both the basin and the hydrodynamics of existing inlets, it is important to understand why an initial breach either closes or may evolve into a new tidal inlet. To this end, we performed a Monte Carlo analysis using an idealized model capable of simulating the long-term morphological evolution of multiple tidal inlets connected to a single backbarrier basin. To do so required the creation of a stochastic shell, as a new element around this existing barrier coast model. Our results demonstrate that barrier coast systems tend towards an equilibrium value for the number of inlets per kilometer of barrier coast and total inlet cross section. This even holds with the continuous stochastic forcing of storm-induced breaches. This finding implies that if a new breach opens in a coast that is already in equilibrium, existing inlets will shrink and may close if the new breach remains open. Furthermore, we find that climate-driven changes in storm frequency will modify the time-scales in which barrier coasts reach their equilibrium state. Finally, we find that the distance between a new breach and its nearest neighbor is more important for its survival than the size of the breach or the degree of saturation of the barrier coast.

This chapter has been published as: Reef, K. R. G., P. C. Roos, T. E. Andringa, A. Dastgheib, and S. J. M. H. Hulscher (2020b). "The Impact of storm-induced breaches on barrier coast systems subject to climate change - A stochastic modelling study". In: *Journal of Marine Science and Engineering* 8.4. DOI: 10.3390/JMSE8040271.

3.1. Introduction

Barrier coasts are important dynamic systems that cover around 10% of the coastlines worldwide (Glaeser, 1978; Stutz and Pilkey, 2011). Due to their ecologic, economic, and touristic worth, they are often densely populated (Oost et al., 2012; Wang et al., 2012). Barrier coasts are highly dynamic systems whose morphology continuously changes under the influence of tides, waves, and storms (De Swart and Zimmerman, 2009). The large-scale morphology of barrier coast systems is controlled by the relative importance of tides and waves (Davis and Hayes, 1984). This study focusses on meso-tidal barrier coasts, that is those in which tides and (fair-weather wind) waves are of equal importance.

A key aspect in the natural morphological evolution of barrier coast systems is the evolution of the tidal inlets, which form the connection that links the outer sea to the inner tidal basin. The impact of tides and waves on the evolution of a single tidal inlet system has already been studied by Escoffier (1940) who showed that for an inlet to be in a morphological equilibrium, the sediment export due to the tide should be balanced by the wave-induced sediment import into the inlet. This equilibirum for multiple-inlet systems is also influenced by the interaction between various elements, such as between the inlets themselves and between the inlets and the backbarrier basin.

Evidence for this interaction comes from the observed residual circulation in backbarrier basins (Salles et al., 2005; Duran-Matute et al., 2014; Sassi et al., 2015), the role of spatially varying backbarrier basin hydrodynamics in the stablity of multiple tidal inlets (Brouwer et al., 2013; Roos et al., 2013), and the fact that the total tidal prism entering a backbarrier basin is primarily a system characteristic that is barely affected by the configuration of the tidal inlets (Reef et al., 2020a).

Storms also significantly affect barrier coasts despite the fact that they are less frequent and more episodic than tides and waves. The effects of storms on barrier coasts range from coastal erosion and local inundation to the breaching of barrier islands (Sallenger, 2000; Kraus et al., 2002). This breaching of barrier islands is one of the mechanisms through which new tidal inlets may form. Regions that commonly experience storm-induced breaches include the east coast of the United States of America (USA) (Leatherman, 1985; Mallinson et al., 2010) and the Ria Formosa in Portugal (Vila-Concejo et al., 2002; Kombiadou et al., 2019). These breaches can have a lasting impact on the entire barrier coast system, as a new inlet conveys a part of the total tidal prism entering the backbarrier basin, and alters tidal dynamics (Hinrichs et al., 2018; Yu et al., 2018).

Examples of the breaching of barrier islands are plentiful. During Hurricane Sandy in 2012 the barrier chain south of Long Island (NY, USA) was breached at three locations, two of them at Fire Island and one at Westhampton (FEMA, 2013). However, at the beginning of 2020, only one of those breaches in Fire

Figure 3.1: Satellite images of three storm-induced breaches at Fire Island and Westhampton (Long Island, NY, USA) due to hurricane Sandy in 2012 showing: a, before the storm (07-March-2012); b, shortly after the storm (04-November-2012); c, almost one year after the storm (20-September-2013). The location of the breaches is indicated with yellow circles (Google, 2016, Map Data: DigitalGlobe, USDA Farm Service Agency).

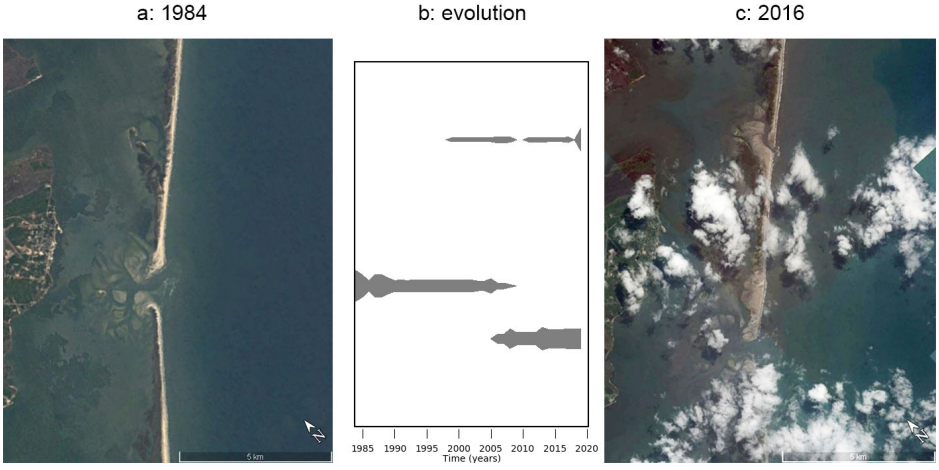

Figure 3.2: Evolution of three tidal inlets — Old Drum (top), New Drum (middle), and Ophelia Inlet (bottom) — that have alternatingly opened and closed at Core Sound, NC, USA. Shown are satellite images from 1984 (panel a) and 2016 (panel c), as well as the evolution (panel b) based on satellite image analysis. After the closing of Old Drum Inlet, New Drum Inlet was opened artificially in 1971. At the site of Old Drum Inlet, (New) Old Drum Inlet opened in 1999 as a storm-induced breach during Hurricane Dennis, and in 2005 Hurricane Ophelia opened Ophelia Inlet south of New Drum Inlet (Mallinson et al., 2008). Later, both Old and New Drum Inlet closed, but were reopened by Hurricane Irene in 2011. At the start of 2020 both Ophelia and Old Drum Inlet are open and New Drum inlet has closed. (Google, 2016, Map Data: Landsat/Copernicus).

Island is still open, which is now called Old Inlet, whereas the other two breaches were closed artificially (see Fig. 3.1). Another example is the Core Sound, the southern part of the North Carolina (USA) outer banks, where three inlets — Old Drum, New Drum, and Ophelia Inlet — have alternatingly opened and closed under the influence of storm-induced breaches (see Fig. 3.2).

These examples illustrate that storm-induced breaches have a profound effect on nearby inlets and the tidal circulation in the backbarrier basin. However, this effect is still poorly understood. Therefore, the goal of this study is to investigate the impact of storm-induced breaches on inlets connected to the same backbarrier basin and on the interaction among these inlets. Specifically, we aim to answer the following research questions:

- How do storm-induced breaches affect existing inlets connecting to the same backbarrier basin and what are the interactions between them?
- What breach characteristics determine whether a breach evolves into an open inlet or closes?
- How are multiple-inlet systems affected by climate driven changes in the storm climate?

To answer our research questions, we need to overcome a methodical challenge as no standard approach exists to combine the two types of driving forces that we consider: storms — occurring on an irregular basis — and tides and waves that continuously affect barrier coast systems (Wang et al., 2012). Our approach is to extend an existing idealized barrier coast model that simulates the morphological evolution of tidal inlets under the influence of tides and waves (Roos et al., 2013) by adding a stochastic shell around the model. This innovation allows the stochastic forcing of storm-induced breaches by determining whether or not breaches at each moment in the morphological evolution. We select an idealized barrier coast model as it allows us to study the effect of individual processes and its low computational cost allows us to systematically study the breach characteristics that determine whether a storm-induced breach remains open or not.

This work is organized as follows. First, the methods including the development of our stochastic shell are presented in §3.2, followed by the results in §3.3, the discussion in §3.4, and finally the conclusions in §3.5.

3.2. Methods

Previous studies on the long-term evolution of (multiple) inlet systems have used simulation models as long-term measurements are not available for a wide range of barrier coasts. Examples of models that have been used include semi-empirical models (e.g. ASMITA; Van Goor et al., 2003), complex process-based

models (e.g. Delft3D; Dastgheib et al., 2008), and idealized models (e.g. Roos et al., 2013). However, none of these models have been combined with a stochastic forcing of storm-induced breaches. This can be partially attributed to the absence of a standard approach to combine stochastic forcing (storms) and deterministic forcing (tides and waves) in barrier coast modelling (Wang et al., 2012).

We build a stochastic shell around an existing idealized barrier coast model (Roos et al., 2013) to allow us to stochastically force storm-induced breaches. This model is outlined in §3.2.1, the stochastic shell is presented in §3.2.2, and the design of our model experiments in §3.2.3.

3.2.1 Idealized barrier coast model

The idealized barrier coast model developed by Roos et al. (2013), and described in Reef et al. (2020a) will be used in this study to simulate the morphological evolution of multiple tidal inlets as it combines the impact of tides and waves on the morphological evolution of inlets. The model domain is represented by a simplified geometry consisting of multiple tidal inlets that connect a rectangular inner tidal basin having a spatially uniform depth to the outer sea where the system is forced by a tidal wave. The j tidal inlets have a length l_j, a cross-section A_j, and shape defined by a shape factor $\gamma^2 = h_j/b_j$ (e.g. De Swart and Zimmerman, 2009). The rectangular tidal basin is characterized by a longshore length L, cross-shore width B, and depth h_b. Finally, on the semi-infinite outer sea of depth h_o, a tidal wave is forced with amplitude Z and tidal frequency ω.

The model consists of a hydrodynamic and a morphodynamic part. The morphodynamic part is based on the stability concept of Escoffier (1940) and combines a constant sediment import M with a sediment export X_j that is based on the velocity amplitude of the tide in an inlet. The balance of these sediment fluxes determines dA_j/dt, that is an inlet accretes ($M > X_j$), erodes ($M < X_j$), or is in equilibrium ($M = X_j$).

The hydrodynamic part is based on the linearized shallow water equations with linearized bottom friction in the basin and inlet channels according to Lorentz' linearization, and it simulates the hydrodynamics in the entire domain. It is forced by a tidal wave on the outer sea with amplitude Z and tidal frequency ω. The morphodynamic part of the model is solved numerically using a forward Euler discretization (with timestep Δt), while the hydrodynamic part is analytically reduced to a linear system of equations that are solved using standard techniques.

In their simulations, Roos et al. (2013) started with an oversaturated barrier coasts (i.e. with far more inlets than the equilibrium configuration) and simulate the morphological evolution of the tidal inlets over centuries towards an equilibrium (or near-equilibrium) configuration in which some inlets remained open

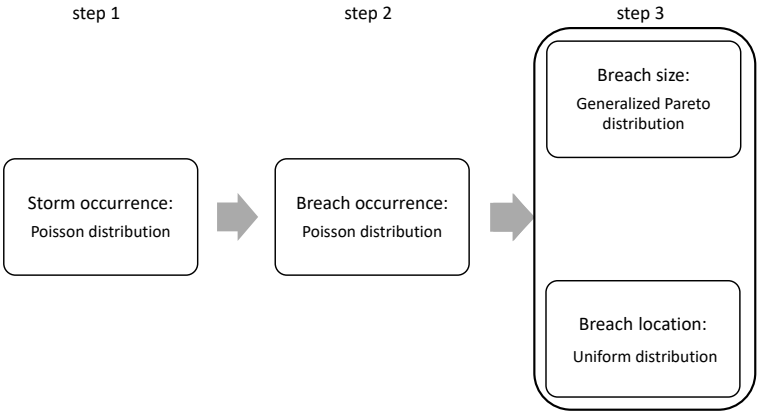

Figure 3.3: Diagram showing the procedure used in our stochastic shell to determine if storm-induced breaches are forced and what their characteristics will be. Further explanation in §3.2.2.

and some have closed. They found that their model results agree with observed relationships between inlet characteristics and both tidal range and tidal basin width.

3.2.2 Stochastic shell: forcing storm-induced breaches

To stochastically force storm-induced breaches in the model of Roos et al. (2013), we develop a stochastic shell around this model. At every timestep, this shell determines whether or not storm-induced breaches are created — and, if so, what their properties are — see Fig. 3.3. This is done in three steps:

step 1 determines the number of storms n_s that occur during the timestep,

step 2 determines the number of breaches n_b that occur (if $n_s > 0$),

step 3 determines the initial inlet cross-section A_{init} and inlet location y_j of each newly created breach (if $n_b > 0$).

In these three steps, we use three different Probability Density Functions (PDFs). In step one, to determine the number of storms n_s that occur during a timestep we use a Poisson distribution as it shows the best fit with the Annual

Hurricane Occurrence dataset (Hosseini et al., 2016), i.e.

$$p(n_s) = \frac{\lambda_s^{n_s}}{n_s!} e^{-\lambda_s}. \tag{3.1}$$

Here we use a mean value λ_s that is the inverse of the location specific recurrence times for hurricanes as determined by Keim et al. (2007).

Because only little data is available on storm-induced breaches, and particularly about their occurrence, we assume that the occurrence and initial size can be modelled using the same PDFs as the occurrence and intensity of storms. Therefore, we also use a Poisson distribution in step two to determine the number of breaches n_b per storm, i.e.

$$p(n_b) = \frac{\lambda_b^{n_b}}{n_b!} e^{-\lambda_b}. \tag{3.2}$$

Here we assume a mean value $\lambda_b = 1$ per storm due to a lack of data on the number of breaches per storm.

In step three, we use a Generalized Pareto distribution to determine the initial inlet cross-section A_{init} as it was found to be the best for the intensity of storms in the Annual Hurricane Occurrence dataset (Hosseini et al., 2016)

$$p(A_{init}) = \left(\frac{1}{\sigma}\right)\left(1 + k\frac{(A_{init} - \theta)}{\sigma}\right)^{(-1-\frac{1}{k})} \tag{3.3}$$

Here the scale $\sigma = 243\ m^2$, shape $k = 7.84 \times 10^{-9}$, and location $\theta = 38\ m^2$ were fitted using data from 19 historic breaches (Vogel and Kana, 1984; MacIvor and Motivans, 1998; Matias et al., 1999; Cañizares and Irish, 2008; Mallinson et al., 2008; Wamsley et al., 2010; Clinch et al., 2012; FEMA, 2013; Flagg et al., 2017; Safak et al., 2016; Google, 2016).

Finally, also in the third step, we use a uniform distribution to determine the inlet location y_j because we assume that the likelihood of a breach is considered the same for every part of the barrier coast (except for existing inlets). This implies

$$p(y_j) = \begin{cases} 0 & \text{for } y_j \text{ at an inlet,} \\ \frac{1}{L_{res}} & \text{for } y_j \text{ not at an inlet.} \end{cases} \tag{3.4}$$

Here $L_{res} = L - \sum_{j=1}^{J} b_j$ is the length of the barrier coast minus the cumulative width of all open inlets.

3.2.3 Design of model experiments

Table 3.1: Model parameters used in this study.

Parameter	Symbol (unit)	Great South Bay	Core Sound
Tidal Elevation Amplitude in sea	Z (m)	0.5	0.325
Tidal Frequency in sea	ω (rad/s)	1.405×10^{-4}	1.405×10^{-4}
Basin Depth	h_b (m)	1.3	2
Basin Length	L (km)	40	30
Basin Width	B (km)	5	5
Drag Coefficient	c_d (-)	2.5×10^{-3}	2.5×10^{-3}
Inlet Length	l_j (km)	0.5	1
Mean Initial Inlet Cross Section	A_μ (m^2)	281	281
Inlet Shape Factor	γ^2 (-)	0.005	0.005
Outer Sea Depth	h_o (m)	10	10
Sediment Import	M (m^3/year)	4×10^5	8.25×10^5
Mean number of Hurricanes per year	λ_s ($year^{-1}$)	1/35	1/5
Morphodynamic Timestep	Δt (year)	0.5	0.5
# of simulations in one ensemble	n (-)	500	500

3.2.3.1 Outline of a single simulation

We start each simulation with a barrier coast without any inlets at $t = 0$ and subsequently force a storm event that induces at least one storm-induced breach. To do so, we start at step two in our stochastic shell and keep repeating this procedure until at least one (possibly more) storm-induced breach is created. This starting procedure is different from Roos et al. (2013) where each simulation was initialized with an oversaturated barrier coast (i.e. with more inlets than in equilibrium). Next, the model simulates the evolution of the storm-induced breaches toward a final inlet configuration over a period of 1,000 years.

At every timestep, two morphological changes are considered. First, the stochastic shell determines whether or not storm-induced breaches are generated (see §3.2.2). Second, similar to (Roos et al., 2013; Reef et al., 2020a) we simulate the morphological evolution of the tidal inlets based on the stability concept of Escoffier (1940) (see §3.2.1).

The resulting final inlet configurations are analyzed using three dimensionless metrics: the ratio of equilibrium inlet cross-section and the mean initial size $A_{j,all}/A_\mu$, the number of open inlets per km barrier coast J_{total}/L, and the relative total tidal prism $P_{total}/P_{ref,total}$ with

$$P_{total} = \sum_{j=1}^{J} \frac{2|\hat{u}_j|}{\omega} A_j \quad \text{and} \quad P_{ref,total} = ZA_{basin} = ZBL. \tag{3.5}$$

Here, the tidal prism for a single inlet (i.e. $\frac{2|\hat{u}_j|}{\omega} A_j$) is obtained by integrating the sinusoidal tidal velocity signal $|\hat{u}_j|$ in an inlet over half a tidal cycle and multiplying the result by the inlet cross-section A_j.

Two sets of parameter values are used in this work. The first represents the Great South Bay system (NY, USA) and the second the Core Sound system (NC, USA), both can be found in Table 3.1.

3.2.3.2 Monte Carlo simulation

To systematically analyze the effect of storm-induced breaches we perform two Monte Carlo ensembles simulation consisting of $n = 500$ individual simulations, for both the Great South bay and Core Sound sets of parameter values (see 3.1). In every simulation different storm-induced breaches are forced, therefore we expect different final configurations for every simulation as well. To aggregate these results, we determine the median and 50% envelope over all simulations in the ensemble using the same metrics as above.

We also use these results to investigate which breach characteristics determine whether or not a storm-induced breach remains open. This is done by analyzing the effect of three breach characteristics:

- the relative size of the breach A_{init}/A_{μ},
- the barrier coast saturation J/J_{μ},
- the distance of a breach to the nearest neighboring inlet $d_{nearest}$.

To do so, we compute 2D histograms showing the breach survival rate of all three combinations of taking two of the three breach characteristics. The chance of breach survival over the entire simulation is defined as

$$p_{survival} = \frac{N_{open}}{N_{open} + N_{closed}}, \tag{3.6}$$

where N_{open} is the total number of breaches that remained open and N_{closed} is the total number of breaches that closed, both determined per histogram bin.

To study the effect of changes in storm climate we vary the storm frequency λ_s in the stochastic shell from -50% to $+50\%$ in 11 Monte Carlo ensemble simulations, consisting of 500 individual simulations each. The range of change in storm frequency from -50% to $+50\%$ is the span of the 67% confidence interval for tropical storm frequency (with a median just under 0), by the IPCC (Intergovernmental Panel on Climate Change, 2013). These results are analyzed by computing the same three metrics as before, as well as the timescale at which the median is at 90% of its final value (the value at $t = 1,000$ yr).

3.3. Results

3.3.1 Example model run

To illustrate individual simulations, Fig. 3.4 shows two example runs, for sets of parameter values *Great South Bay* and *Core Sound* (found in Table 3.1). It shows how, in both cases, an initially undersaturated barrier coast with some storm-induced breaches (panel a & d) evolves under the influence of more storm-induced breaches (panel b & e) towards a 'final' configuration in which more inlets are open (panel c & f). During the simulation a number of storm-induced breaches remain open and evolve into tidal inlets while most eventually close. Our example simulation shows that not only do new breaches close, but in some cases if the new breach remains open, nearby prior inlets may close.

Furthermore, the example run for the Great South Bay (Fig. 3.4 top row) shows an example of jump migration (Vila-Concejo et al., 2006) where an inlet (the bottommost inlet) closes and a nearby breach remains open (effectively moving the inlet).

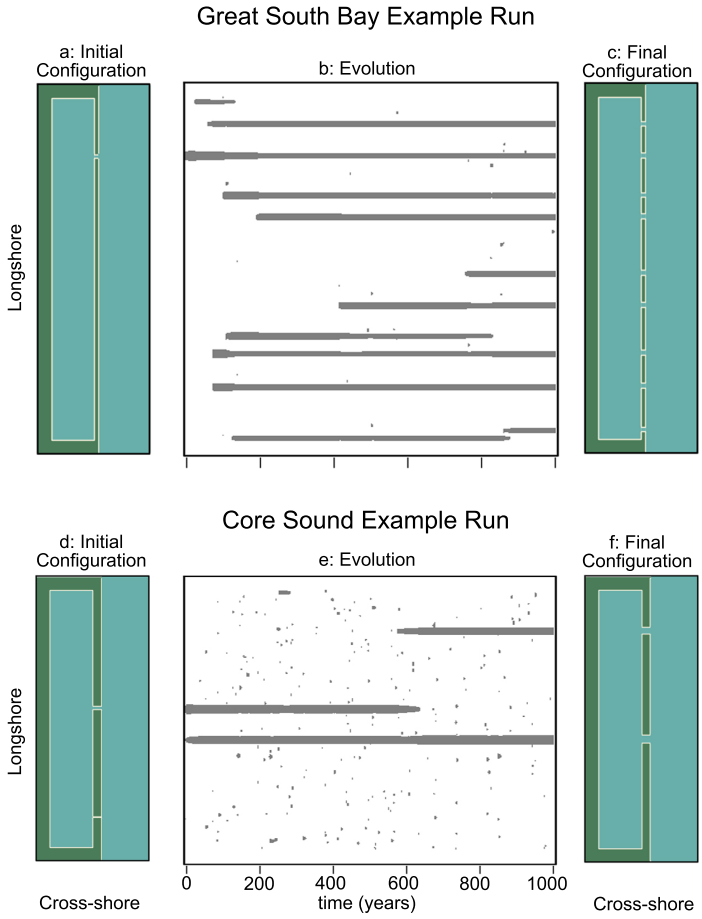

Figure 3.4: Two example runs for the sets of parameter values: Great South Bay (top), Core Sound (bottom). Shown are: the initial configuration with one open inlet (a & d); evolution of the system during which storm-induced breaches are stochastically forced (b & e); the final configuration with multiple open inlets (c & f). Please note that the grey dots correspond to breaches that quickly close after being randomly created.

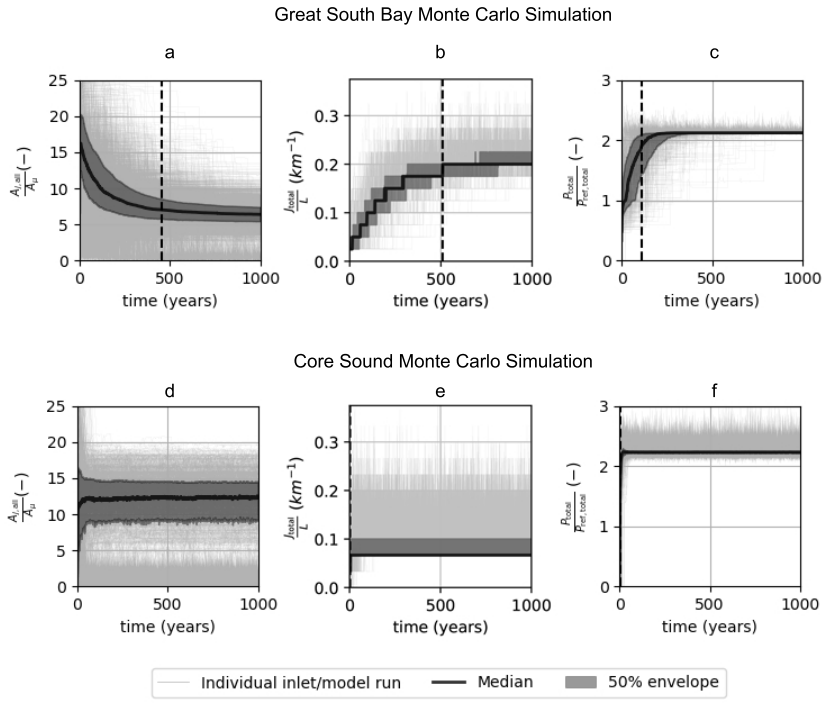

Figure 3.5: Results of two Monte Carlo simulations (N = 500) for both the Great South Bay (top) and Core Sound (bottom). Shown are: the ratio $A_{j,all}/A_{\mu}$ (a & d); the number of open inlets per km barrier coast J_{total}/L (b & e); dimensionless total tidal prism $P_{total}/P_{ref,total}$ (c & f), see §3.2.3. As these metrics are aggregated over all model runs, we show the mean (solid black), 50% envelope (dark grey), and individual model runs in light grey. The timescale to reach 90 % of the final value has been indicated by dashed lines.

3.3.2 Monte Carlo ensemble

To further analyze the impact of storm-induced breaches on barrier coast systems, we examine the results of two Monte Carlo ensembles for both the *Great South Bay* and *Core Sound* sets of parameter values (see Table 3.1).

Each Monte Carlo ensemble consists of 500 individual model runs, this number of individual model runs ensures that our results have converged, such that more runs would only change the result marginally. We find that even with the random forcing of breaches all three metrics (see §3.2.3.1) tend towards an equilibrium (see Figure 3.5). This means that the system reaches a dynamic equilibrium state, even with a continuous stochastic forcing of storm-induced breaches.

Comparison of the results for both sets of parameter values reveals that the equilibrium values and timescales are dependent on the set of parameter values. For all three metrics, the Core Sound system reaches its equilibrium values faster than the Great South Bay system. The former system approaches its equilibrium values very fast (the timescale in panel d & f coincides with the y-axis). The Core Sound system has less open inlets than the Great South Bay system (i.e. J_{total}/L is lower), while the inlets are larger (i.e. $A_{j,all}/A_{\mu}$ is larger).

The results for the Great South Bay also show that the dimensionless total tidal prism $P_{total}/P_{ref,total}$ approaches its dynamic equilibrium value first, followed by the ratio $A_{j,all}/A_{\mu}$, and finally the number of inlets J_{total}/L. Therefore, the configuration of the tidal inlets (i.e. size and spacing) takes longer to reach a dynamic equilibrium than the overall tidal prism of all inlets combined. This also explains why the ratio $A_{j,all}/A_{\mu}$ is initially relatively high; the dimensionless total tidal prism $P_{total}/P_{ref,total}$ increases faster than the number of open inlets per km barrier coast J_{total}/L, so each inlet conveys a larger part of the total tidal prism $P_{total}/P_{ref,total}$ than in the final state.

3.3.3 Breach survival chance

Next, we investigate how the three breach characteristics already introduced in §3.2.3.2, control the chance of a breach to survive and evolve into a stable tidal inlet. This is done by analyzing all storm-induced breaches that were forced in the Monte Carlo ensemble presented in the previous section. Figure 3.6 shows three histograms for all possible combinations of two breach characteristics.

These histograms show that the distance to the nearest neighbor $d_{nearest}$ is the breach characteristic that best predicts whether a breach will remain open or not. If a barrier coast is undersaturated (i.e. $J < 0.5J_{\mu}$), breaches closer to a nearest neighbor have an increased likelihood to remain open as well. Finally, the effect of the initial breach size A_{init} is that larger breaches slightly increase the chance of survival. This pattern was observed for both the Greath South Bay

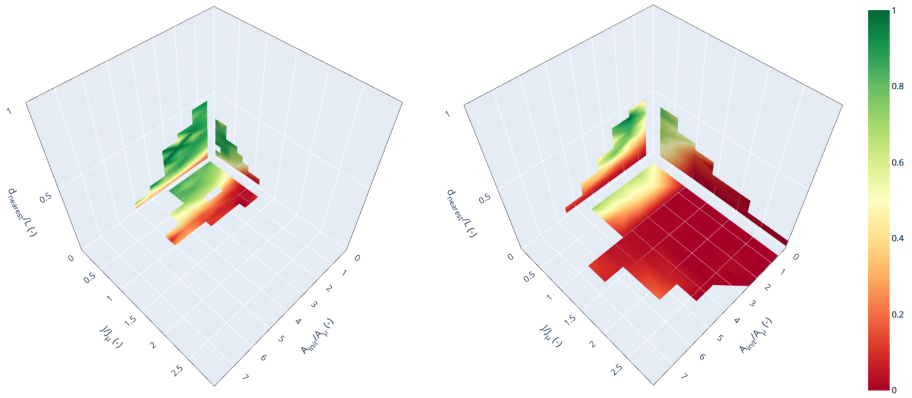

Figure 3.6: Breach survival chance shown for the simulations of Great South Bay (left) and Core Sound (right) sets of parameter values (see Table 3.1), in three histograms for varying values of relative initial breach size A_{init}/A_{μ}, barrier coast saturation J/J_{μ}, and distance to nearest neighboring inlet $d_{nearest}$.

(left part Figure 3.6) and the Core Sound (right part Figure 3.6) sets of parameter values.

3.3.4 The effects of climate change

The effect of changes in storm frequency due to climate change (Intergovernmental Panel on Climate Change, 2013) is that the timescales for the system to reach its dynamic equilibrium change, but the resulting values in dynamic equilibrium do not change. This change in timescale (here defined as time required to reach $\pm 10\%$ of the final value at $t = 1000$ yr) is shown in Figure 3.7. The results show that an increase (decrease) in storm frequency clearly leads to a shorter (longer) timescale for all three metrics for the Great South Bay system. The timescale for the inlet cross-section $A_{j,all}/A_{\mu}$ and the number of open inlets per km barrier coast J_{total}/L to reach their equilibrium value decreased from around 700 yr for $\lambda_s = 0.5$ to around 400 yr for $\lambda_s = 1.5$. For the total tidal prism $P_{total}/P_{ref,total}$ the timescale to reach its equilibrium decreased from over 300 yr for $\lambda_s = 0.5$ to just over 100 yr for $\lambda_s = 1.5$. For the Core Sound system, the timescale are very short already and barely changes due to variations in the storm frequency.

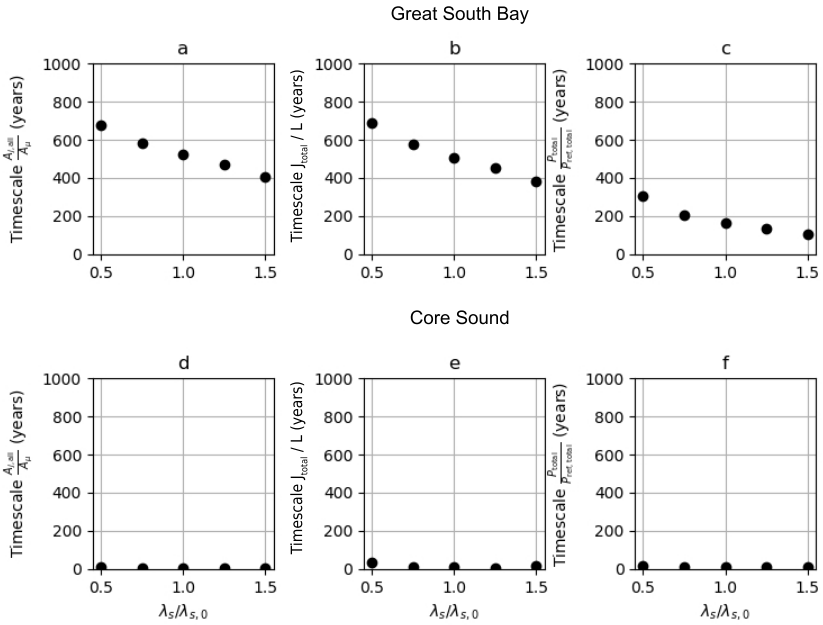

Figure 3.7: Effect of changes in storm frequency for the Great South Bay (left) and Core Sound (right) sets of parameter values (see Table 3.1). For the same three metrics as in Fig. 3.5, the timescales required to reach 90% of their final value is plotted while storm frequency F_s is changed between -50% and +50%.

3.4. Discussion

3.4.1 System-wide equilibrium

Our results show how a barrier coast system will reach a dynamic equilibrium in terms of inlet cross-section $A_{j,all}/A_{\mu}$, the number of open inlets per km barrier coast J_{total}/L, and total tidal prism $P_{total}/P_{ref,total}$ while being stochastically forced by storm-induced breaches. Moreover, the systemwide equilibrium in total tidal prism $P_{total}/P_{ref,total}$ implies that if a breach remains open once this equilibrium has been reached, it will take over part of the tidal prism from the existing inlets, potentially leading to inlets closing. The above implies that a storm-induced breach that remains open affects barrier coast systems in two ways. First, a new breach directly provides a new connection between the outer sea and basin resulting in changed hydrodynamics in both. Second, that as a result a new breach indirectly affects the existing tidal inlets and the impact that they have on the hydrodynamics in both the outer sea and basin. Importantly, these two aspects are nonlinearly coupled.

Furthermore, we found that variations in storm frequency do not lead to a different total tidal prism, only the equilibrium timescale might change. This result implies that if the storm frequency increases, barrier coast systems will reach their dynamic equilibrium faster. So, if a barrier coast is moved away from its equilibrium state (e.g. due to human interventions such as closing newly opened breaches) more effort will be required to maintain the non-equilibrium state if the storm frequency increases. These findings agree with previous findings indicating that the total tidal prism for a barrier coast system is a system characteristic (Reef et al., 2020a) and thus independent of storm frequency.

3.4.2 Survival of the farthest

Our analysis on which breach characteristics are adequate predictors for the survival of a storm-induced breach showed that the distance to a neighboring inlet is the best predictor, followed by barrier coast saturation as second best and initial breach size as third.

The importance of a minimum distance between a new breach and a neighboring inlet indicates the need for a 'barrier' between different inlets for them both to remain stable. This finding is in agreement with previous findings of a minimum inlet spacing between multiple tidal inlets (Roos et al., 2013) and separations such as a topographic high (i.e. a tidal divide) leading to stable configurations for double inlet systems (Van de Kreeke et al., 2008; De Swart and Volp, 2012).

If a new breach close to an existing inlet drains the backbarrier basin more efficiently than the existing inlets, this could lead to the closure of the existing

inlet. In this case, the new inlet succeeds in capturing part of the total tidal prism entering a backbarrier basin, which has been found to be a system characteristic (Reef et al., 2020a). Factors that were found to impact the minimum spacing of tidal inlets are the tidal range and backbarrier basin width (Roos et al., 2013; Reef et al., 2020a). Other factors that are likely to affect this minimum spacing are the depth of the basin h_b, length of an inlet l_j, and bottom friction in both the basin r_b and inlets r_j.

3.4.3 Model validity & limitations

In this work we studied the impact of storm-induced breaches on barrier coast systems (i.e. not the actual breaching of barrier islands) and imitated the stochastic nature of storms in the idealized barrier coast model by Roos et al. (2013). Their earlier results showed a good qualitative agreement between the model results and observed relationships between inlet size and spacing and both tidal range and tidal basin width. Furthermore, Reef et al. (2020a) demonstrated that the model was capable of qualitatively reproducing the observed phenomena.

To assess the validity of how we stochastically simulate the storm capacity to induce breaches, we assess the results of the Monte Carlo ensemble. These results show that an equilibrium number of inlets is reached by the system, implying that most new breaches will close or cause a nearby inlet close. The example run (see Fig. 3.4) also shows that most newly created breaches close as soon as the number of inlets has reached its equilibrium value. These results agree with observations from natural systems in which numerous tidal inlets, that started as storm-induced breaches, have closed (Mallinson et al., 2010). Examples of these natural systems are the barrier coasts systems considered in this study: the Great South Bay and the Core Sound system.

As a result of incorporating the most important processes which affect the long-term morphological evolution of barrier coast systems, our model is capable of capturing the most important qualitative behavior of the natural system. To attain a better quantitative description of the natural system, future work could include more morphological features that affect inlet locations such as tidal divides (Van de Kreeke et al., 2008; De Swart and Volp, 2012), washover deposits (Leatherman, 1985; Kraus et al., 2002), relict inlet features (Leatherman, 1985), channel networks (Kragtwijk et al., 2004; Reef et al., 2018), and paleographic river valleys (FitzGerald, 1996) that control inlet locations. Furthermore, additional processes can be considered such as basin and outer sea morphodynamics (Kragtwijk et al., 2004; Elias et al., 2012), changing boundary conditions due to climate change (Glaeser, 1978; Stutz and Pilkey, 2011), and nonlinear hydrodynamics (Salles et al., 2005).

3.5. Conclusions

We studied the impact of storm-induced breaches on the long-term evolution of multiple-inlet systems to an equilibrium configuration. To do so, we performed a Monte Carlo simulation in which storm-induced breaches were stochastically forced using a newly created stochastic shell around an idealized barrier coast model. Using parameters representative for the Great South Bay and Core Sound, we determined that most breaches close while some remain open and develop towards a new stable inlet. The formation of a new inlet has a profound impact on the barrier coast system dynamics as a whole, as a new inlet (nonlinearly) affects not only the basin hydrodynamics, but also the morphodynamics of the neighboring inlets. Despite this, the system tends towards an equilibrium in terms of number of inlets and total tidal prism, while stochastically forced by storm-induced breaches.

By analyzing all storm-induced breaches in our Monte Carlo ensemble, we identified the distance to a neighboring inlet as the breach characteristic that is the best predictor for a breach to remain open or not. Finally, we also determined that an increase in storm frequency due to climate change can lead to a decrease of the timescale over which these equilibria are reached.

Acknowledgements

The authors wish to thank four graduate students who helped doing exploratory simulations. We also thank three anonymous reviewers for their helpful comments and J. Strickland for proofreading the manuscript.

Chapter 4: Time-varying storm surges on Lorentz's Wadden Sea networks

Abstract

An idealized network model for the storm surges in the Wadden Sea extends the classical work by H.A. Lorentz, who only considered the equilibrium response to a steady wind forcing, by including time-varying wind speed and direction. The solutions obtained in the frequency domain for the linearized shallow-water equations in a channel are combined in an algebraic system for the network of tidal channels. The velocity scale used for the linearized friction coefficient is determined iteratively. The hindcast of the storm surge of 5 December 2013 produces credible time-varying results. A sensitivity analysis addresses the effects of storm and basin parameters on the peak surge elevation. The formulation in the frequency domain identifies the modes in the external forcing contributing the most to the surge response at coastal stations. A minimum storm duration of about 3-4 hours is required for a surge to attain its maximum elevation. The influence of the water levels at the North Sea inlets on the Wadden Sea surges decreases towards the shore, while the wind forcing generates its largest response near the shore, where the fetch length is at its maximum.

This chapter has been published as: Reef, K. R. G., G. Lipari, P. C. Roos, and S. J. M. H. Hulscher (2018). "Time-varying storm surges on Lorentz ' s Wadden Sea networks". In: *Ocean Dynamics* 68.8, pp. 1051–1065. DOI: 10.1007/s10236-018-1181-5.

4.1. Introduction

Storm surges, the raised water levels induced by strong winds in coastal areas, pose a serious hazard of flooding and of loss of life and property. This is amplified by growing population pressure, sea level rise, and increasing storminess projections due to climate change. Weather systems act upon the water by means of the atmospheric-pressure differences and the wind stresses acting on the free surface. The surge dynamics is further influenced by tides, nonlinear tide-surge interactions, wave dynamics, bed interactions, and the physiographic features of the coastal area. See e.g. Puch (1983) for general information on storm surges.

Storm surges have their greatest impact on shallow seas, in embayments, and on shores of low-lying lands. A region combining these vulnerabilities in the Netherlands was the Zuiderzee (lit. Southern Sea), a fringe basin in the southern North Sea, which in the 19th and early 20th century had been affected by 18 major floods (Rijkswaterstaat, 1916). In the aftermath of the deadly flood of 13 January 1916, the political consensus was reached to separate permanently the Zuiderzee from the outer basin with a dam, which was completed in 1932. The placemarks DO and KZ of Fig. 4.1a mark off the 32-km long Afsluitdijk (lit. closure dike) dividing the former Zuiderzee bay (the present-day lake IJssel) from the basin between the mainland and the tidal islands (the Wadden Sea). In preparation for the construction works, in 1918 a task panel, the State Committee for the Zuiderzee, was appointed to determine the change of peak elevations caused in the Wadden Sea by the diversion of the tidal and wind-driven currents. Its chairman, the Nobel laureate H.A. Lorentz, asserted the necessity of a novel investigation based on first principles (Mazure, 1963; Kox, 2007).

The report of State Committee on the Zuiderzee (1926) provides a pioneering idealization of the physiographic complexity of a tidal basin. The extensive flats of the Wadden Sea are separated by deep channels originating at the inlets, also visible in Fig. 4.1a. Since most of the water flows along these tidal channels, the State Committee on the Zuiderzee represented the western Wadden Sea as a network of equivalent channels having depth and width uniform over their length — specifically commented upon in §4.2.1.

Whereas originally this simplified approach aimed to overcome limitations of computing, idealized basins have been used until recently for investigating phenomena in coastal dynamics, such as tides (Hill and Souza, 2006; Alebregtse et al., 2013; Alebregtse and De Swart, 2014; Alebregtse and De Swart, 2016), storm surges (Stroband and Wijngaarden, 1977), and tide-surge interactions (Prandle and Wolf, 1978). Their enduring advantage over the models retaining the full complexity of physics and topography — for example Zijl et al. (2013), Duran-Matute et al. (2014), and Duran-Matute et al. (2016) — lies in their computational efficiency. Idealized models do reproduce key physical processes

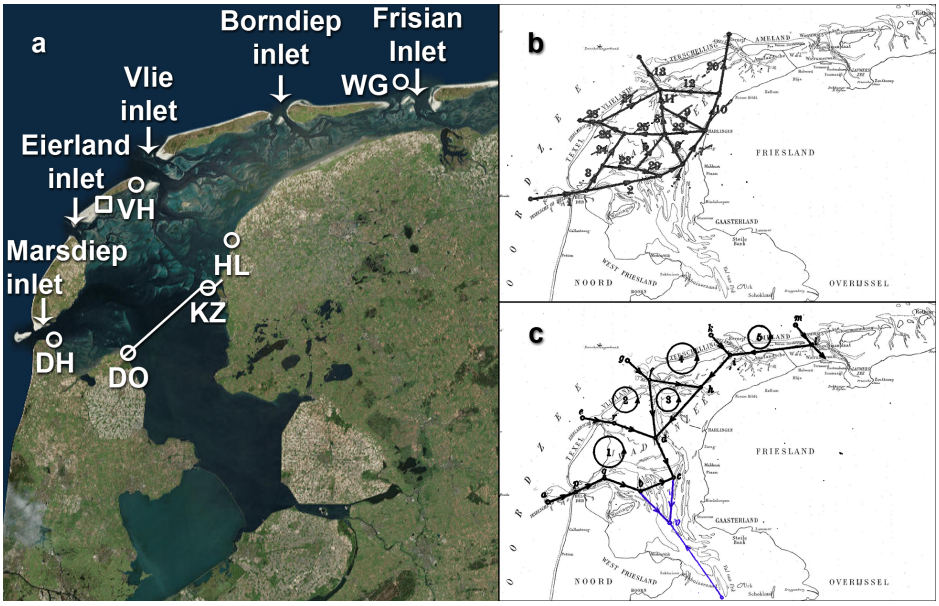

Figure 4.1: **a** Satellite image of the western Dutch Wadden Sea (United States Geological Survey, 2016). The *Afsluitdijk* dam is shown in white between the markers DO and KZ. The present-day lake IJssel, inland of the dike, is the previous sea bay known as *Zuiderzee*. Tidal gauges used for this study are indicated on the map by ○: Den Helder (DH), Den Oever (DO), Harlingen (HL) Kornwerderzand (KZ), Vlieland Haven (VH), Wierumergronden (WG). The wind measurement station at Vlieland is indicated by □. **b** The 'tidal network' used by the State Committee on the Zuiderzee for simulating tidal flows (their §45). **c** The 'storm network' used for simulating storm surges (their §89), with channels representing the Zuiderzee in blue (see §4.3.2.1).

at a limited computational cost, and provide accurate results (both in a quantitative and qualitative sense), for example usable for extensive sensitivity analyses against geometrical and physical modelling parameters that drive the system's response — as presented in this article.

Further, in order to compute the one-dimensional flow inside the individual channels, the State Committee on the Zuiderzee (1926) linearized the shallow-water equations averaged over the channels' cross sections. To this end, the seabed friction was parametrized through a novel procedure based on energy-equivalence arguments, known as Lorentz linearization, described in §4.2.2.2.

Unfortunately, for the lack of adequate processing power at the beginning of the 20th century, the tide and storm-surge simulations could only be performed separately. In particular, the storm-surge simulations consisted of calculating the steady-state water levels in equilibrium with an extreme wind having fixed speed and direction. Therefore, the State Committee on the Zuiderzee could not identify that both motion and storage of the surge water inside the Wadden Sea are modulated by the temporal variability of the wind field, as well as by the fluxes across the tidal inlets — see, for example, the reanalyses of Lipari et al. (2008), Lipari and Vledder (2009), and Duran-Matute et al. (2016). This implies that, in a semi-enclosed basin, the most severe surges are not necessarily generated by the storms with the highest wind speed. Time-varying storms can cause higher surges than steady-state storms do, even when the peak wind speed is the same (Lipari et al., 2008).

Jallah and Bakker (1994) already coded a computerized transcription of the model and algorithms of the State Committee on the Zuiderzee. Here, inspired by Lorentz's seminal studies of the Wadden Sea surges, and drawing from the work of Chen et al. (2015, 2016), we have developed a new idealized network model allowing for time-varying external forcing, namely the storm surge elevation in the outer sea and the wind-stress field. The model is based on the linearized shallow-water equations applied to the flow in the network channels. Unlike the State Committee on the Zuiderzee, the equations are cast in the frequency domain after Fourier transformation of both input and output variables and the equations. Because of the linearity, the superposition of the solutions of the individual modes gives the unsteady solution in the time domain.

With this tool we aim to provide insights on the transient behavior of storm surges within tidal basins. We will specifically investigate how basin characteristics, storm characteristics, and different forcing mechanisms affect the transient behavior of storm surges in tidal basins. The model, the forcings, and the outline of the solution method are presented in §4.2. The simulations presented in §4.3 deal with the hindcast of the storm surge of 5 December 2013, the sensitivity analysis of the peak surge on the coast to selected basin and storm parameters, and a modal analysis of the surge response to the external forcing. Finally, §4.4 and §4.5 contain the discussion and the conclusions.

Table 4.1: Characteristics of the 'tidal network' and 'storm network'.

	Tidal network	Storm network	Storm network with Zuiderzee
Number of nodes			
Internal	31	10	11
Open sea	4	5	5
On coast	0	0	1
Total	35	15	17
Number of channels			
Total	69	33	36
Max. ratio of h/b	0.03	0.01	0.01

4.2. Methods

4.2.1 Network geometry

The study area covers the western sub-basin of the Wadden Sea from the Texel Inlet in the west to the Frisian Inlet in the east, as shown in Fig. 4.1a. The State Committee on the Zuiderzee schematized the routing of water along the tidal channels with two networks of rectangular channels, each having uniform depth, h, and width, b, over its length, l. A finer 'tidal network' was used for the sole simulations of tidal dynamics (Fig. 4.1b), a coarser 'storm network' for the simulation of the storm surge (Fig. 4.1c). Both networks consist of channels connected at nodes where boundary conditions are imposed (§4.2.2.3) accounting either for the interior linkages or for the influences of the open sea and the coast. Some information on the two networks is shown in Table 4.1; for the complete data see §45 ('tidal network') and §89 ('storm network') in the report of the State Committee on the Zuiderzee (1926). Notably, the widths of the channels are much larger than their depth (maximum value in our networks: $h/b = 0.03$), and the cross-channel variation in width is small.

We have borrowed both networks for developing the analyses presented in §4.3.

4.2.2 Hydrodynamic model

4.2.2.1 Governing equations

Using the condition $h \ll b$ and that of small cross-channel variations, the hydrodynamic model for simulating unsteady wind-driven flows in a network consists of a system of one-dimensional, cross-sectionally averaged, linearized

shallow-water equations written for each j-indexed channel:

$$\frac{\partial \zeta_j}{\partial t} + h_j \frac{\partial u_j}{\partial x} = 0, \tag{4.1}$$

$$\frac{\partial u_j}{\partial t} + \frac{\tau_{b,j}^{lin}}{\rho h_j} + g\frac{\partial \zeta_j}{\partial x} = \frac{\tau_w \cos\tilde{\theta}_j}{\rho h_j}, \tag{4.2}$$

where t is time, x denotes the position on the channel axis, h_j is the constant channel depth with respect to the undisturbed water level, $\zeta_j(x,t)$ is the corresponding free surface elevation, $u_j(x,t)$ is the cross-sectionally averaged flow velocity. Further, $\tau_{b,j}^{lin}(x,t)$ is the linearized bed shear stress, further specified and discussed in §4.2.2.2, while $\tau_w(t)$ and $\tilde{\theta}_j(t)$ are the wind shear stress and the angle between the wind direction and the positive direction of the channel axis, both further specified and discussed in §4.2.2.4. Finally, $g = 9.81$ m s^{-2} is the gravitational acceleration, and $\rho = 10^3$ kg m^{-3} is the density of water. Henceforth, we will refer to the cross-sectionally averaged velocity as velocity, and to the free-surface elevation with respect to the undisturbed water level as elevation.

4.2.2.2 Lorentz's linearization of the bottom friction

For tidal simulations, on the one hand, Lorentz proposed a seminal linearization of the bottom shear stress τ_b. Unlike quadratic formulations, such as

$$\tau_{b,j}^{quad} = \rho\frac{g}{\chi_j^2}|u_j|u_j, \tag{4.3}$$

where χ_j is the Chézy smoothness coefficient, the parametrization with a linearized friction coefficient r_j

$$\tau_{b,j}^{lin} = \rho r_j u_j, \tag{4.4}$$

paved the way to a closed-form solution of the shallow-water equations. Lorentz required the friction coefficient r_j to be such that, over the tidal cycle of the M_2 constituent, in each channel the quadratic and linear stresses yield the same energy dissipation. Hence he set

$$\int_0^T \tau_{b,j}^{quad} u_j \, dt = \int_0^T \tau_{b,j}^{lin} u_j \, dt \tag{4.5}$$

with tidal period $T = 2\pi/\omega_{M_2}$ where ω_{M_2} is the angular velocity of the monochromatic tide. For a harmonic signal for the velocity, $u_j = U_j \cos(\omega_{M_2} t)$, the equal-

ity (4.5) leads to the expression for the friction coefficient

$$r_j^{\text{tide}} = \frac{8}{3\pi}\frac{g}{\chi_j^2}U_j, \tag{4.6}$$

with the amplitude of the tidal velocity, U_j, providing a natural scale for it.

For simulating aperiodic storm surges, on the other hand, no energy-based argument could be applied in a straightforward manner. To circumvent this, the State Committee on the Zuiderzee adopted a steady equilibrium approach at a single moment in time and retained the quadratic friction formulation. In contrast, we have implemented a linearized friction parametrization using, as velocity scale, the peak velocity attained in each channel during the simulated time, $u_{j,\text{peak}}$ (the mild form of non-linearity implied by this choice is discussed in §4.2.3). Our linearized friction coefficient for unsteady storm surges reads

$$r_j^{\text{surge}} = g\frac{\mu_j^2}{h_j^{1/3}}u_{j,\text{peak}}, \tag{4.7}$$

where a Manning formulation captures the explicit sensitivity of friction to the channel depth (μ is the Manning roughness coefficient). The linearized and quadratic friction parametrizations are then equal at the point in time when the velocity in the channel is at its peak value. Further, the time-invariant part of our solution (§4.2.3) resembles the approach of the State Committee on the Zuiderzee closely.

In their surge simulations, the State Committee on the Zuiderzee used a constant Chézy coefficient $\chi = 50\ \text{m}^{1/2}\ \text{s}^{-1}$. We use a constant Manning coefficient $\mu = 0.0242\ \text{s}\ \text{m}^{-1/3}$, corresponding to coastal waters with characteristic grain sizes of $D_{50} = 0.2$ mm and $D_{90} = 0.5$ mm with a typical depth of 5 m (Barua, 2017). These conditions are typically found in the Wadden Sea area, such as in the Borndiep basin near Ameland (Van Straaten, 1954), and in the basin of Spiekeroog (Flemming and Ziegler, 1995).

4.2.2.3 Boundary conditions

The boundary conditions for each channel are assigned at the n-indexed network nodes, and concern either the connection of the network with the open sea, or interior nodes where channels meet, or the coast. At the open sea, the time series of water elevations is imposed, say at $x = 0$

$$\zeta_j(0,t) = \zeta_{\text{sea}}(t), \tag{4.8}$$

where the appropriate expression for the time series $\zeta_{\text{sea}}(t)$ is specified later in §4.2.3. In the interior nodes n, where q channels meet, at all times the eleva-

tions must be equal for all channels and the sum of inflows must equal that of outflows:

$$\zeta_{j_1}(t) = \zeta_{j_2}(t) = \ldots = \zeta_{j_q}(t) \tag{4.9}$$

$$\sum_{k=1}^{p} u_{j_k} b_{j_k} h_{j_k} = \sum_{k=p+1}^{q} u_{j_k} b_{j_k} h_{j_k}. \tag{4.10}$$

Here a total of p channels cause inflows into node n and $q - p$ channels cause outflows. Finally, the water velocity vanishes, at the coast, say at $x = l$:

$$u_j(l_j, t) = 0. \tag{4.11}$$

4.2.2.4 Wind forcing

The model is forced by a spatially-uniform, time-dependent wind stress of magnitude $\tau_w(t)$ and direction $\theta(t)$. The wind stress τ_w (N m^{-2}) is represented as in Puch (1983):

$$\tau_w = C_w \rho_{air} |u_w| u_w, \tag{4.12}$$

with u_w the wind speed at a standard 10 m height (m s^{-1}), $\rho_{air} = 1.225$ kg m^{-3} the density of air, and $C_w = 5.2 \times 10^{-4} u_w^{0.44}$ a dimensionless wind-drag coefficient, following Safaie (1984).

4.2.3 Outline of solution method

Drawing from the work of Chen et al. (2015, 2016), a temporal Fourier transform is applied to the governing equations (4.1) and (4.2), which are solved for the individual modes in the frequency domain. The superposition of the individual solutions then gives the solution to the full problem in the time domain.

The time-dependent wind stress is written as a superposition of m-indexed modes having $2M + 1$ equally-spaced angular frequencies ω_m:

$$\tau_w(t) \cos \tilde{\theta}_j(t) = \sum_{m=-M}^{M} W_m \exp(i\omega_m t), \quad \omega_m = m\omega_{min}, \tag{4.13}$$

with the constant complex amplitudes W_m (N m^{-2}). For τ_w to be a real-valued quantity, we require W_{-m} to be equal to its complex conjugate (denoted by an overbar), i.e. $W_{-m} = \overline{W}_m$. Since all modes are periodic, after the simulated time window, T_{simul}, the transformed wind-stress signal (4.13) repeats itself by construction; the lowest resolved angular frequency is thus given by

$\omega_{min} = 2\pi/T_{simul}$. For simulating a storm event with a physically limited duration, T_{event}, we require that T_{simul} is sufficiently larger than T_{event} to prevent that significant spurious interferences arise from the periodicity of this approach. At the other end of the spectrum, the highest resolved angular frequency is $\omega_{max} = M\omega_{min}$, where the truncation number, M, determines the temporal resolution of the signal. We also note that the mode with number $m = 0$ represents the time-invariant contribution.

Likewise, the Fourier expansions for the velocity and elevation in each channel are

$$u_j(x,t) = \sum_{m=-M}^{M} U_{j,m}(x)\exp(i\omega_m t), \tag{4.14}$$

$$\zeta_j(x,t) = \sum_{m=-M}^{M} Z_{j,m}(x)\exp(i\omega_m t), \tag{4.15}$$

having space-varying complex amplitudes $U_{j,m}(x)$ and $Z_{j,m}(x)$. This same formulation holds for the boundary conditions with assigned elevations, as in Eq. (4.8).

The closed-form solutions of each mode are given in Appendix 4.A.2.

4.2.3.1 Network

The solution for an entire network (see Fig. 4.1b,c) is obtained by solving the linear system of the channel equations and of the corresponding boundary conditions at the nodes. First, for each mode, the flow solution for the network is derived. The summation of the $2M + 1$ network-wide solutions then gives the evolution over the simulation period of all flow quantities at the nodes. The distribution of elevations and velocities inside each channel are obtained from summing up the closed-form expressions (4.20), (4.21) in Appendix 4.A.2.

Finally, the above procedure is nested in a cycle for determining the velocity scale to the bottom friction coefficient of formula (4.7), $u_{j,peak}$. Starting from an estimated seed, the velocity scale is corrected iteratively with an under-relaxation procedure until the residual $R = \sqrt{u_{j,peak}^2 - u_j^2}$ does not exceed 10^{-3} m/s.

4.2.3.2 Simulations

Our analyses are based on the simulation of two weather events:

- The storm of 5 December 2013, known as 'Sinterklaas' storm or Xavier storm (Rijkswaterstaat, 2013). We have applied the measured wind signals at Vlieland, shown in Fig. 4.2a, as a time-varying and spatially uni-

form field over the basin. The wind direction during the storm was mostly northwesterly.

The elevation data at the tide gauges shown in Fig. 4.1a have been retrieved from Rijkswaterstaat (2016), which include tide. For the open-sea nodes we used the signals at Den Helder (DH), Vlieland Haven (VH) and Wierumergronden (WG). These have been applied to the nearest tidal inlets (Marsdiep; Eierland and Vlie; Borndiep and Frisian inlets, respectively): the modelling error of not having truly local data for some inlets is minor, owing to the limited influence of boundary elevations on the surge farther inside the Wadden Sea (see §4.3.3.1). The signals at the coastal stations of Den Oever (DO), Kornwerderzand (KO), and Harlingen (HL), have then been used to assess the model predictions.

The baseline physical parameters have been given in §4.2. The numerical parameters are T_{simul} = 10 days and M = 127; as a result, being able to resolve periods of nearly 1.9 h, the simulations reproduce the frequency content of the hydrometeo data, sampled at intervals of 1 h.

These simulations are used in §4.3.1 and §4.3.2.1.

- An artificial episode with a schematized wind stress pattern (Fig.4.2b), for evaluating the influence that the storm ramp-up time T_{ramp}, storm duration T_{event}, and wind direction θ have on the free-surface set-up and set-down at the coast. The ramp-up time T_{ramp} is the duration of the ramp-up as well as of the ramp-down stage. The duration of the storm event T_{event} is defined as the period between halfway the ramp-up and halfway the ramp-down of the storm duration, and should be larger or equal to the ramp-up time (i.e. $T_{event} \geqslant T_{ramp}$). The ramp-up time can be varied in the range $0 \leqslant T_{ramp} \leqslant T_{event}$ without changing the total 'amount' of wind stress experienced by the system, as illustrated by the blue shaded areas. The peak wind stress is 1.25 N m^{-2}, and the direction is northwesterly.

  These simulations are used in §4.3.2.2 and §4.3.3.

4.3. Results

4.3.1 Hindcast

To gain confidence in our model, we first applied it to a hindcast of the 'Sinterklaas' storm. This storm surge has been simulated on both networks of Fig. 4.1b,c. The model's performance is evaluated against the quantitative and qualitative expectations that, during the surge development, the simulated water levels, $\zeta_{modelled}$ stay within a 20% error range with respect to the measured water levels, $\zeta_{measured}$, and with limited phase lags.

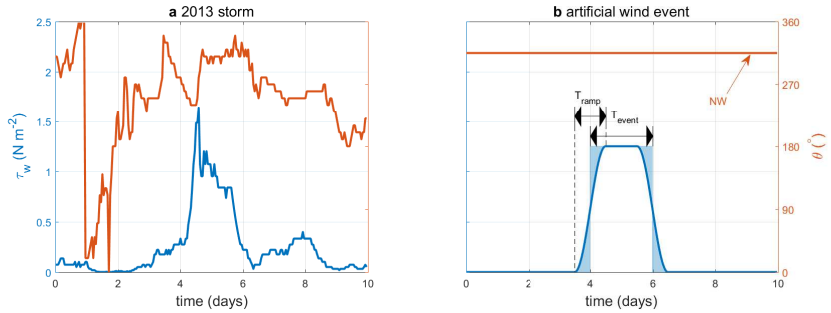

Figure 4.2: Wind stress (blue, left ordinates) and direction (orange, right ordinates) for: **a** The storm of 5 December 2013 measured at the station Vlieland (indicated by □ in Fig. 4.1a) (KNMI, 2016); **b** An artificial wind event with a ramp-up, constant-wind and ramp-down period. Compass directions according to nautical convention (N is 0°, angles grow clockwise).

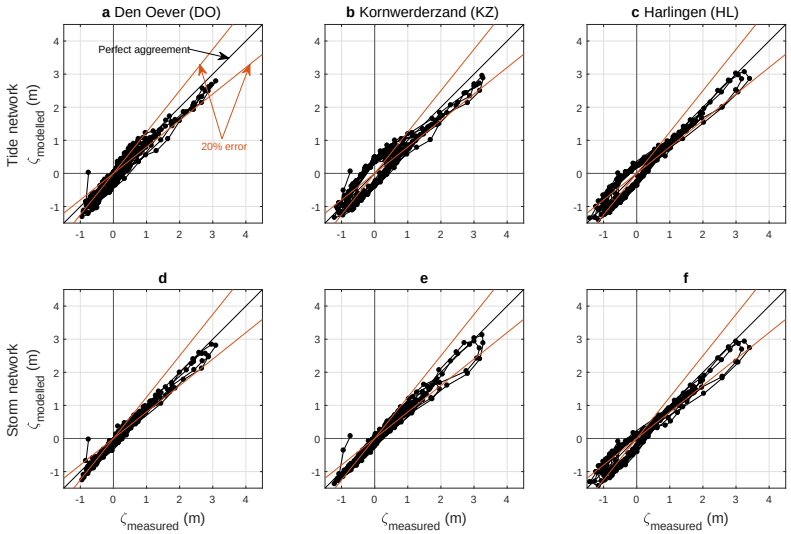

Figure 4.3: Scatter plots of the measured and simulated elevations for the hindcast of the 5 December 2013 surge at three stations in the Wadden Sea (see Fig. 4.1a) with both networks of Lorentz's. Top row: 'tidal network' (Fig. 4.1b); bottom row: 'storm network' (Fig. 4.1c). The black bisector indicates a perfect match between model results and measurements; the red lines indicate a 20% error. Numerical parameters: T_{simul} = 10 days, M = 127.

In the scatter plots in Fig. 4.3 the line connecting the 1h-spaced data points renders the temporal development at 1 h intervals: there, magnitude errors appear as distances from the plot bisector, and phase errors appear as loops. These show that the simulated storm surge elevations have a maximum error within $\pm 20\%$ of the measurements, for all stations (columns) and both networks (rows). In most cases, the simulated surges tend to underestimate the measurements, as seen from the data points below the bisector during the surge development. The maximum errors during the surge are, in fact, less than 0.6 m with the 'tidal network' and than 0.8 m with the 'storm network', whereas the error in the peak surge level is less than 0.1 m.

The denser 'tidal network' of Fig. 4.1b (Fig. 4.3, top) leads to slightly better quantitative agreement during the surge than the coarser 'storm network' of Fig. 4.1c does (Fig. 4.3, bottom). This is clearly observable for the surge at stations Den Oever (DO) and Kornwerderzand (KZ), since the dots in the top panel are closer to the perfect agreement line. The agreement at the station of Harlingen is possibly affected by the fact that the networks do not allow flow towards the eastern Wadden Sea. Also note that the network nodes that can be associated to each stations are not exactly the same in either network. Then, before and after the surge, for elevations within typical tidal ranges, the 'storm network' (Fig. 4.3, bottom) performs better than the 'tidal network' (Fig. 4.3, top).

In sum, there is a reasonably good qualitative agreement between the modelled water levels ζ_{modelled} and the measured ones ζ_{measured} and in the error of peak elevations. The performance of the model is qualitatively correct and quantitatively acceptable at all three stations for both networks, remarkably in the lack of any *ad hoc* calibration.

Having considered that the 'tidal network' gives only slightly better results at the cost of accounting for twice as many channels, in the remainder of our analysis we restrict ourselves to the 'storm network'.

4.3.2 Sensitivity of the peak elevations to basin and storm parameters

4.3.2.1 Basin parameters

We study the influence of the basin on the storm surge by varying three parameters: sea-level rise, basin size, and friction. The effects of their variations on the peak of the storm surge of 5 December 2013 are shown in Fig. 4.4. For the sensitivity to basin size, an output station has been placed at the dam. These results are based on the model fully forced by both the wind stress over the domain and the elevation signals at the inlets; we assume that the variations of the sensitivity analysis do not affect the elevation signals assigned at the open

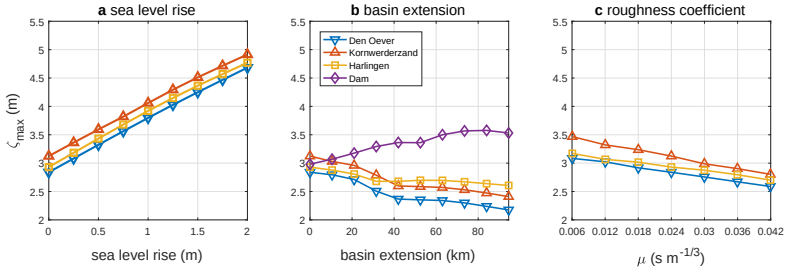

Figure 4.4: Variations of the peak surge elevations at Den Oever, Kornwerderzand, Harlingen and the dam for the hindcast of the 5 December 2013 surge. **a**: against sea level rise. **b**: against basin extension; the distance in the abscissae corresponds to a simulated landward displacement of the Afsluitdijk with respect to its present-day location. **c**: against the Manning's friction coefficient μ_j in Eq. 4.7. Numerical parameters: T_{simul} = 10 days, M = 127, 'storm network'.

boundaries.

The sea level rise has been imposed by increasing the depth of the network channels uniformly. Its influence, shown in the left panel, results in an almost linear increase of elevations by the coast. Interestingly, the increase of the peak elevations by the coast is slightly smaller than the assigned sea level rise, which indicates that the combined effect cannot be reduced to the addition of surge and sea level rise.

Next, the middle panel shows the peak elevations against different southward displacements of the dam from its real position. Moving the location of the Afsluitdijk southwards increases both the wind's fetch length and the basin's water storage. The network has been extended by adding channels representing the Zuiderzee (as shown in Fig. 4.1c, in blue). A larger basin size increases the peak elevations at the fictional dam location because of the increased fetch, while reduces those at Den Oever and Kornwerderzand (at the real dam position) because of the basin's wider extent. The peak elevations at Harlingen, further away from the bay entrance, are less sensitive to the re-positioning of the dam.

Finally, the right panel shows the influence of the Manning's roughness coefficient, μ. A single value has been applied to the whole network. A higher roughness coefficient leads to lower elevations, since increased friction hampers the inflow of surge water into the network. The roughness coefficients range from unrealistically smooth values for the identification of resonance peaks (i.e. $\mu = 0.006\,\mathrm{s\,m^{-1/3}}$ and $\mu = 0.012\,\mathrm{s\,m^{-1/3}}$), through earth channels (clean and straight: $\mu = 0.018\,\mathrm{s\,m^{-1/3}}$; and winding: $0.024\,\mathrm{s\,m^{-1/3}}$), to rubbly ($\mu = 0.03\,\mathrm{s}$

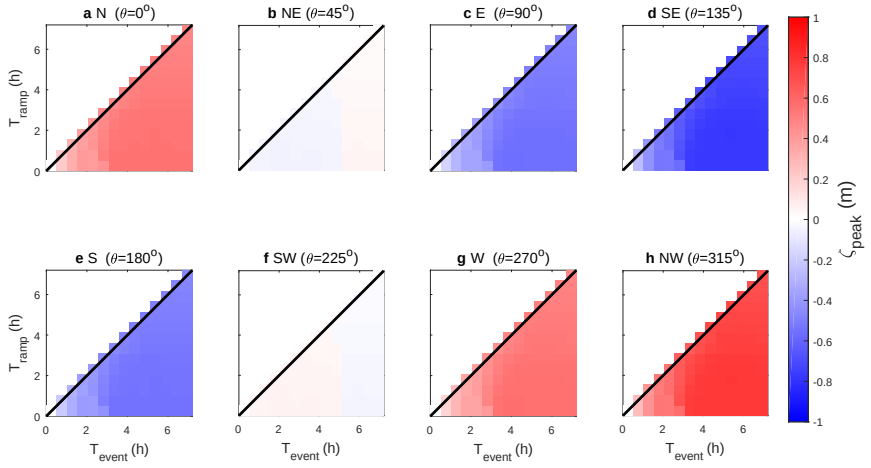

Figure 4.5: Effect of the parameters of the artificial wind event (ramp-up time T_{ramp}, duration T_{event}, and wind direction θ) on the peak water elevation at Kornwerderzand, and the inherent response time of the system. Note that $T_{ramp} \leqslant T_{event}$. Compass directions according to nautical convention. Numerical parameters: T_{simul} = 10 days, M = 127, 'storm network'.

$m^{-1/3}$), stony ($\mu = 0.036\ s\ m^{-1/3}$), and cobble-bottomed ($\mu = 0.042\ s\ m^{-1/3}$) channels (Chow, 1959). Within the range of realistic parameters (say $\mu = 0.018 - 0.042\ s\ m^{-1/3}$) the impact of the uncertainty of the roughness coefficient on the surge elevation at the coast is below 0.5 meters. It should be noted that different estimates could be obtained when the roughness has a spatial distribution of its own.

4.3.2.2 Storm parameters

The parameters defining the artificial storm profile of Fig. 4.2b have been varied to identify their influence on the peak elevations. These are the wind direction θ, the peak duration T_{event}, and the ramp-up time T_{ramp}. Unlike in §4.3.2.1, here we set the elevation signal at the inlets to zero and isolate the effect of wind stress from that of the open-boundary forcing. This approach is justified by the (near) linearity of our model; discounting the iterative calculation of friction, the solution to the fully forced model is the superposition of the individual solutions of the separate forcings. This choice is also practical, since we do not know the elevation at the inlets during the artificial wind event.

Fig. 4.5 shows the peak water elevations at Kornwerderzand, where we dis-

tinguish between set-up and set-down. There, a northwesterly wind ($\theta = 315°$) causes the highest set-up of 75 cm, followed by the northerly and westerly ones ($\theta = 0°$, 55 cm; $\theta = 270°$, 55 cm). This is expected because of the downwind position of this station, and because of the longer fetch across the basin. In contrast, southerly and easterly winds tend to push the water out of the basin towards the open sea, lowering the elevation at the coast, hence causing the free-surface set-down. This is observed for southeasterly ($\theta = 135°$, -75 cm), southerly ($\theta = 180°$, -55 cm), and easterly ($\theta = 90°$, -55 cm) winds.

Panels *a*, *g*, and *h* also indicate that a minimum storm duration is required before the maximum peak surge is reached. This minimum duration is also observed in panels *c* through *e* for a set-down. At Kornwerderzand this minimum duration for maximum set-up is of about 3-4 hours. For locations Den Oever and Harlingen the peak elevation (ζ_{peak}) is somewhat lower (55 cm and 45 cm, respectively) and is reached around the same time (after 3-4 hours).

The influence of ramp-up time is limited to minor variations in the resulting surge, at least for a fixed wind direction.

4.3.3 Frequency response analysis

The formulation of a time-varying process in the frequency domain makes it possible to dissect the causal relationship between external forcings and resulting flow fields into the constituting individual modes. To this end, we consider as many forcing scenarios as there are modes: in the m-th scenario, the m-th mode in the forcing has unit amplitude, whilst all others modes are zero. Again, as in §4.3.2.2, this is motivated by the model's (near) linearity. The corresponding solution highlights the degree of sensitivity of the overall response to that unimodal unit forcing. Therefore, we can identify the modes in the forcings (external hydrography, wind shear) that are conducive to higher responses (elevations) at any selected location (the coastal stations).

The forcing factors considered separately are the elevations assigned at the network open boundaries (the tidal inlets), and the direction of the wind stress vector, these simulations have been carried out on the 'storm network'.

4.3.3.1 Forcing of elevations at the tidal inlets

Fig. 4.6 shows the elevation response to a monochromatic unit boundary conditions at each of the five tidal inlets. The wind stress is nil and the velocity scale ($u_{j,peak}$) used in Eq. (4.7) is fixed at 1 m/s. The response is quantified by the amplitude of the complex amplitude of the elevation, Z_m.

The range of the roughness coefficients used here is the same as in the sensitivity analysis of §4.3.2.1; $\mu = 0.0242\,s\,m^{-1/3}$ is chosen as baseline value. With the different Manning friction coefficients the elevations at the Texel and Vlie

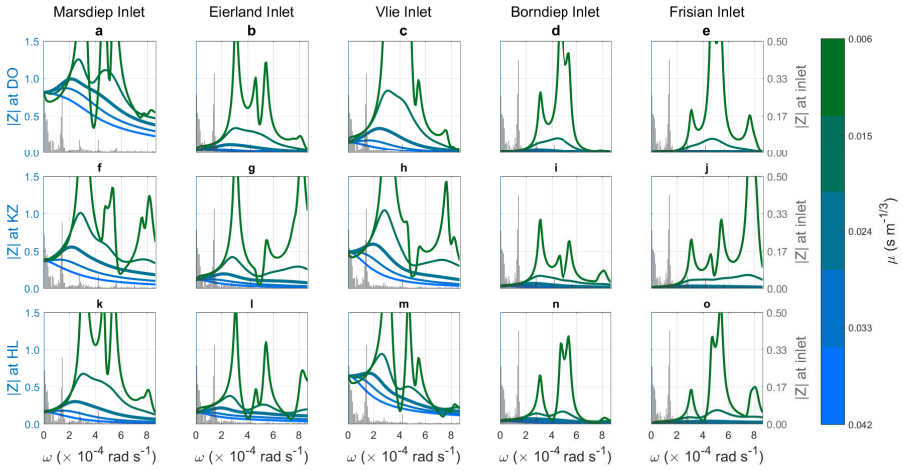

Figure 4.6: Amplitude of the onshore elevation response to unimodal unit forcings at the tidal inlets, for different values of the roughness coefficient μ. Top row: Den Oever; middle row: Kornwerderzand; bottom row: Harlingen. The line colour shades indicate roughness coefficients μ; the thick line is the baseline value $\mu = 2.42 \times 10^{-2}\,\mathrm{s\,m^{-1/3}}$. Numerical parameters: T_{simul} = 10 days, M = 127, 'storm network'. The elevation amplitudes of the 'Sinterklaas' storm (Fig. 4.2a) are given in grey shades and on the right axis.

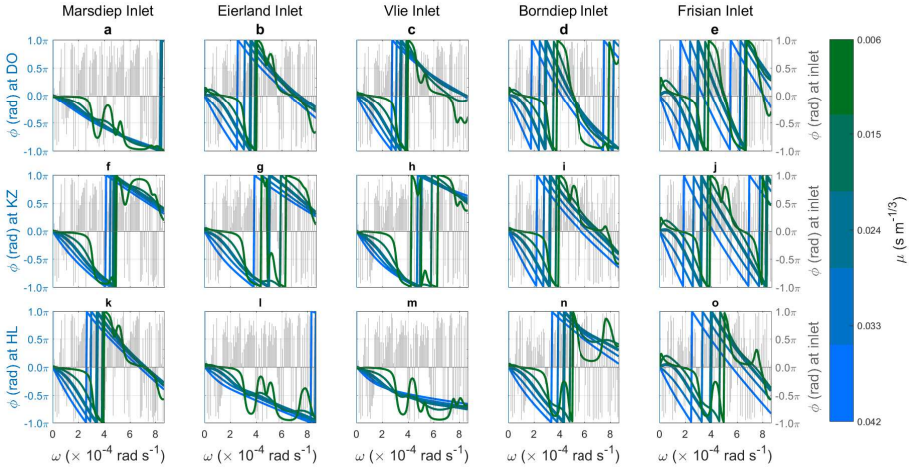

Figure 4.7: Phase of the onshore elevation response to unimodal unit forcings at the tidal inlets, for different values of the roughness coefficient μ. Same coding as Fig. 4.6

inlets generate the largest response at Den Oever and Kornwerderzand, the stations nearby. These locations are all in the westernmost part of the basin unlike the Borndiep and Frisian Inlets, which are somewhat further east and exert no influence at the output stations. The narrow Eierland Inlet, also in the west, has a minor influence. For the Texel Inlet the modes at angular velocities of around $\omega = 3 \times 10^{-4}$ rad s^{-1} (T = 8.7 hours) determine the highest response. For the Vlie Inlet this occurs for angular velocities around or just under the same value, depending on the station.

Higher friction coefficients ($\mu = 0.033$ s m$^{-1/3}$ and $\mu = 0.042$ s m$^{-1/3}$) result in a lowering of the surge response for all cases. This is due to the increased friction holding back the flow of water and reducing the response at the measuring stations further in the basin. Lower friction coefficients ($\mu = 0.015$ s m$^{-1/3}$ and $\mu = 0.006$ s m$^{-1/3}$) lead to strong variations in the frequency response at the observation locations. There are clear response peaks around $\omega = 3 \times 10^{-4}$ rad s^{-1}, observed at all three locations for forcings originating at one of three inlets (Marsdiep Inlet, Eierland Inlet, and Vlie Inlet). In practice, this maximum response suggests that the basin experiences resonance due to oscillations of this precise frequency. For the two other inlets (Borndiep Inlet and Frisian Inlet) resonance peaks can be observed at different frequencies. We also observe that the effect of the friction coefficient is small for modes with a

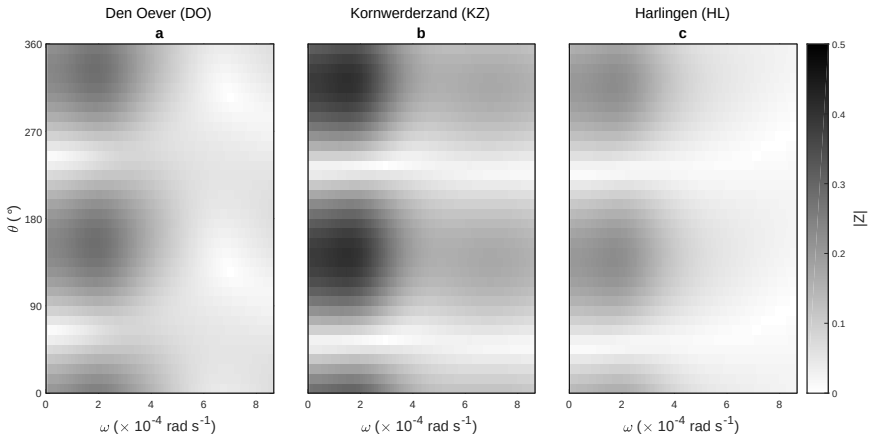

Figure 4.8: Amplitude of the onshore elevation response (shading) to unimodal unit wind stresses (abscissae) for varying directions (ordinates). Left: Den Oever; middle: Kornwerderzand; right: Harlingen. Numerical parameters: T_{simul} = 10 days, M = 127, 'storm network'.

low angular frequency. The power of a storm is indeed concentrated at such low angular frequencies (see the grey bars in Fig. 4.6): so the effect of changes in roughness coefficient will be limited for the storm surge. Note that, in our approach, these low-frequency events are correctly handled as oscillations that do no recurring within our simulation window, T_{simul}.

Fig. 4.7 shows the phase angles corresponding to the amplitudes in Fig. 4.6. Frstly, the phase variations are the largest if the observation station and the inlet are the farthest away (e.g. Den Oever and Frisian Inlet), and vice versa (e.g. Harlingen and Vlie Inlet). This indicates that distance between inlet and observation location is again important for the frequency response. Secondly, changes in friction coefficient μ result in a phase shift of the frequency response. High values of the friction coefficient lead to a constant but faster rate of change of the phase angle; a higher friction coefficient causes a slower propagation into the basin of the variations of the water level at the tidal inlet. Low values of the friction coefficient lead to a more fluctuating yet slower overall rate of change of the phase angle; these result in a slower change over the entire spectrum, although the response becomes more susceptible to fluctuations due to resonance.

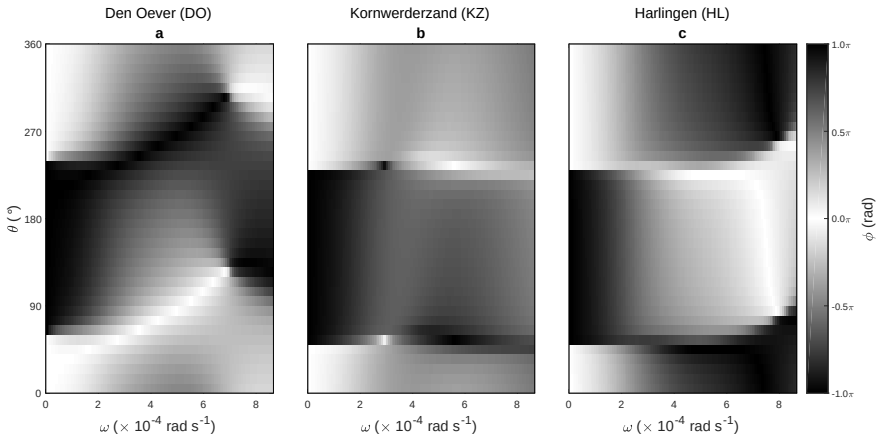

Figure 4.9: Same as Fig. 4.8, but for the phase (ϕ) instead of the modulus of the onshore elevation response for varying wind direction.

4.3.3.2 Wind direction

Fig. 4.8 shows the elevation response at the output stations to a unimodal unit wind stress. The water elevations at the boundaries are zero. The strongest responses occur for south-southeasterly (157°) and north-northwesterly winds (337°) with the greatest sensitivity to forcing modes of $\omega = 2 \times 10^{-4}$ rad s^{-1} (T = 8.7 h). In the Wadden Sea, northwesterly wind directions tend to cause elevation set-up, the southeasterly ones set-down, as seen in Fig. 4.5. The station most sensitive to wind influence appears to be Kornwerderzand, while the least sensitive is Harlingen. At higher frequencies the response is much smaller and independent of the wind direction. This happens at frequencies around 4×10^{-4} rad s^{-1}, corresponding to oscillations of just above 4 hours. So the effect of fast oscillations in the wind stress signal is much smaller than for slower oscillations. Since storms are mainly composed of slowly oscillating constituents and their time scale is in the order of days, a minimum storm event duration is required for the basin to generate the significant surge responses. This is in agreement with the findings in §4.3.2.2.

Fig. 4.9 shows the phase response at the output stations, in a similar way to Fig. 4.8. At lower frequencies the phase response mainly shows two opposite values, whereby the wind amplitude peaks of Fig. 4.8 act in opposite direction; as shown in Fig. 4.5, southeasterly winds cause a set-down response, and northwesterly ones set-up.

4.4. Discussion

The network-based idealized model for the Wadden Sea described in this study appears to be well-suited for gaining insights in the behavior of unsteady storm surges in a semi-enclosed tidal basin. The hindcast of the storm surge of 5 December 2013 presented in §4.3.1 agrees with measurements within 20% of magnitude and with small phase errors at the peaks time, all the simplifications of its construction and settings notwithstanding.

4.4.1 Critique of the model assumptions

One of the model simplifications is the linearized form of the shallow-water equations. Neglecting nonlinear dynamics implies the neglect of tide-surge interactions, the relevance of which has been noted by Spencer et al. (2015) in their study of the same 2013 storm surge on the English coast: "Storm surge impacts are not simply linearly related to maximum elevation but rely on more complex, nonlinear interactions between tide-surge condition". Nonetheless, the agreement between the measured and simulated elevations for the 5 December 2013 storm surge is reasonable.

Furthermore, Prandle and Wolf (1978) signal that on the Thames Estuary the dominant interaction mechanism between tides and storm surges is nonlinear (quadratic) friction. Instead, our model implements a channel-wise, time-invariant, linearized parametrization of bottom-friction using the peak velocity as scale. Also, this friction coefficient overestimates bottom friction before and after the storm, when the velocities are mostly driven by tidal streams. Overcoming this limitation is focus of ongoing research (Roos et al., 2017).

Along the same lines, Horsburgh and Wilson (2007) explained the surge clustering at the time of rising tide mathematically as the consequence of a tidal phase shift combined with the modulation of surge generation due to water depth. Another assumptions of linear dynamics, that water elevations are small in comparison to the water depth, becomes less realistic under storm conditions.

Here, we should notice that Lorentz's networks do not allow the water to flow further into the eastern Wadden Sea, which naturally occurs and can be an important factor determining which storms actually generate local severe surges (Lipari et al., 2008; Duran-Matute et al., 2016). Our model cannot reproduce this basin-wide surge dynamics and, as a result, the two easternmost inlets extert a limited influence upon the surge in the western Dutch Wadden Sea (see Fig. 4.6).

4.4.2 Determinants of the surge elevations

Storm surges in semi-enclosed tidal basins are caused by a local wind effect, a set-up of water at the tidal inlets (i.e. a regional wind effect), and atmospheric

pressure effects (neglected in this study). Our (nearly) linear model is capable of simulating storm surges in tidal basins, and linearity enables to study the effect of the different forcing mechanisms separately. Both the wind and the elevations at the tidal inlets produce a stronger response at lower frequencies (longer periods) at the coastal stations Den Oever, Kornwerderzand, and Harlingen in the Wadden Sea.

On the one hand, the elevations at the Marsdiep and Vlie inlets, the two dominant inlets, produce surge peaks responding to a frequency of $\omega \approx 3 \times 10^{-4}$ rad s^{-1} (T $\approx$ 35′), with weaker responses to lower frequencies (for $\mu = 0.0242$ s m$^{-1/3}$). The influence of the elevations at the tidal inlets on the surge at the coast can be ascribed to two factors: the inlet size, and the distance from the tidal inlet, given the network. The narrower Eierland Inlet has a trailing influence on the water elevations at the output stations Den Oever and Harlingen, regardless of the proximity to it. Then, the response generated by the conditions set at the tidal inlets fades with the distance from them. For example, the Texel Inlet influences Den Oever more than elsewhere, and likewise for the Vlie Inlet and Harlingen. Furthermore, there is a small response at Den Oever, Kornwerderzand and Harlingen to the water level variations in the Borndiep Inlet and Frisian Inlet.

On the other hand, the responsiveness to wind shear displays distinct peaks at frequencies in the range of $\omega = 0-4$ rad s^{-1} (T $= 0-8.7$ h), with significantly lower responses to higher frequencies. Long-period oscillations are only present in storms with a sufficiently long duration. Therefore, storms in tidal basins require a minimum duration before they can produce their peak surge elevation.

We analysed this minimum storm duration by focusing only on the surge generated locally by the wind shear, and found minimum duration in the order of several $(3-4)$ hours. The minimum duration required for reaching the peak surge is explained by the non-instantaneous adaptation of the water to changes in the forcing, such as a rapid increase of wind stress (or of water level at the inlets). It is important to realize that real-world storms have a time-varying wind stress, as seen in Fig. 4.2 for the 'Sinterklaas' storm. Therefore, during a storm the water system constantly adjusts to the evolving time-dependent forcing, instead of aiming at steady-state equilibrium.

Expectedly, the largest set-up is caused by northwesterly winds, and the largest set-down by southeasterly winds. When considering a northwesterly storm, the wind forcing shows an opposite relationship of the response amplitude with the distance from the land boundary, because of the onshore wind and fetch length. Locations with a shorter fetch length, such as Den Oever and Harlingen, show smaller surge response to a unit wind stress than locations with a larger fetch length like Kornwerderzand.

4.5. Conclusion

We have developed a new idealized network model for storm surges in the western Dutch Wadden Sea, extending the modelling approach of the (State Committee on the Zuiderzee, 1926) with a time-dependent wind-stress magnitude and direction. We probed the validity of our approach by simulating the 5 December 2013 'Sinterklaas' storm, which lent sufficient confidence in our model.

The effect of basin characteristics on the transient behavior of storm surges has been analysed using the full set of forcings, that is wind shear over the domain and elevation signals at the tidal inlets. We considered the impact of changes in sea level, basin extension, and friction coefficient. We found that sea-level rise results in a slightly less increase of the surge height than the amount of sea-level rise imposed. The effects of basin extension, aiming to reproduce the situation before the closure of the Zuiderzee, consist of increased surge heights at the back of the basin and lower elevations near the present day location of the Afsluitdijk; this is, indeed, the situation that the State Committee on the Zuiderzee aimed to prevent. The sensitivity of the model to the roughness coefficient showed that an increase in bottom roughness results in a lower surge, and vice versa.

The effect of storm characteristics on surges has been analysed using only wind forcing and varying the ramp-up time, duration, and wind direction for an artificial wind event. We found that the effect of the ramp-up time is limited, whereas a minimum duration is required for a surge to attain its peak level. The wind direction has an expected effect both on set-up (northwesterly winds result in the highest surge, followed by northerly and westerly winds) and set-down (southeasterly winds result in a larger lowering than easterly and southerly winds).

The effect of different forcing mechanisms on the transient behavior of storm surges has been studied by dissecting the solution of our model into the separate responses to the individual forcing frequency components having unit value. This has been done both for the elevation signal at the tidal inlets and for the wind forcing. The response of the coastal surges to the elevation signal at the tidal inlets is affected by the distance from the inlet and by the size of the inlet; larger inlets have a larger influence on the basin, and inlets have a larger influence on the nearer regions of the basin. The wind forcing was shown to have the largest effect near the coastal boundary of our basin, since the larger fetch results in the higher set-up on the coast.

Acknowledgements

The authors thank H.E. de Swart for sharing his knowledge of the work of the State Committee on the Zuiderzee and his feedback; and J.R. de Graaf, J.C. Hazeleger, M.D. Krol for their contribution to the sensitivity analysis. The remarks of the anonymous reviewers stimulated the achievement of valuable insights.

4.A. Solution method

4.A.1 Boundary-value problem for complex amplitudes

The expressions (4.13), (4.14) and (4.15) are substituted into the continuity and momentum equations (4.1) and (4.2) resulting in

$$Z_m = -i\,h\frac{U'_m}{\omega_m}, \tag{4.16}$$

$$\left(\frac{r}{h} + i\,\omega_m\right) U_m + g\,Z'_m = \frac{\cos\tilde{\theta}}{\rho h}\,W_m, \tag{4.17}$$

where the primes indicate derivatives with respect to x.

4.A.2 Closed-form solution for the flow in the channel

Combining equations (4.16) and (4.17) leads to an inhomogeneous Helmholtz problem for the velocity amplitude:

$$U'' + k_m^2 U = -i\frac{\cos\tilde{\theta}}{gh^2\rho}\omega_m W_m, \tag{4.18}$$

with mode-dependent complex wavenumbers k_m:

$$k_m^2 = \frac{\omega_m^2}{gh}\left(1 - i\,\frac{r}{h}\frac{1}{\omega_m}\right). \tag{4.19}$$

The solutions for each mode are

$$U_m(x) = U_{0m}\cos k_m x - i\frac{1}{h}\frac{\omega_m Z_{0m}}{k_m}\sin k_m x + i\frac{\cos\tilde{\theta}}{gh^2\rho}\frac{\omega_m W_m}{k_m^2}(\cos k_m x - 1), \tag{4.20}$$

$$Z_m(x) = Z_{0m}\cos k_m x - i\,h\frac{k_m U_{0m}}{\omega_m}\sin k_m x + \frac{\cos\tilde{\theta}}{gh\rho}\frac{W_m}{k_m}\sin k_m x. \tag{4.21}$$

For any given mode of the wind forcing W_m, these relationships link the amplitudes of the flow velocity and of the surface elevation at any location x inside a channel (U_m, Z_m) with the respective values at the begin of the channel (U_{0m}, Z_{0m}).

Chapter 5: Conclusions

5.1. Conclusions

In this section the research questions as presented in §1.5, and repeated below, are answered.

What is the influence of back-barrier basin planview geometry, and changes therein, on multiple inlet systems?

To answer this research question, we extended an existing barrier coast model, to enable inclusion of backbarrier basins of arbitrary shape. This allowed us to study the effect of the planview geometry of a backbarrier basin on multiple inlet systems.

By simulating the evolution of an oversaturated barrier coast (i.e. with more inlets than in equilibrium) towards an equilibrium state, we found that the cross-shore basin length has a significant effect on the number of inlets, the cross-section of the inlets, and the total tidal prism entering the basin.

We found that the total tidal prism is impacted linearly by the cross-barrier basin length (referred to as basin width in chapter 5) for smaller basin lengths, then shows a resonant response for longer basins before the response becomes constant due to the dissipation of the tidal wave due to bottom friction.

Furthermore, we found that the effect of local changes in basin geometry is felt by inlets along the entire basin, instead of only by the inlets in the immediate proximity. This implies that if the geometry of the backbarrier basin is changed in one area (e.g. due to the damming of a bay or land reclamation), this has a direct local effect and an indirect effect on the entire barrier coast system due to changes in the hydrodynamics of the basin.

What is the impact of storm-induced breaches on multiple inlet systems, and how is this affected by climate change?

To answer this research question, we again extended an idealized barrier coast model, capable of simulating the long-term morphological evolution of multiple tidal inlets towards an equilibrium state, by including a mechanism for tidal inlet creation due to storm-induced breaches. This allowed us to study the impact of barrier island breaching and the creation of new tidal inlets, on existing

multiple inlet systems.

By including storm-induced breaches in a stochastic way in our model and by performing a Monte Carlo simulation, we found that storm-induced breaches that remain open and turn into stable tidal inlets have a profound impact on the neighboring inlets. A new tidal inlet that remains open captures a part of the total tidal prism entering a tidal basin. As we found that the total tidal prism has a maximum value for a specific basin and tidal conditions, a new inlet that remains open can end up cannibalizing the tidal prism of existing nearby inlets.

The rate at which the system tends towards this maximum total tidal prism depends on the storm frequency. As the storm frequency around the world is expected to change due to climate change, this rate of change is expected to be affected as well.

Finally, we found that the distance of a breach to its neighboring inlets is the most important predictor for an inlet remaining open or not.

How do variations in back-barrier basin geometry and storm surge characteristics affect storm surges in the Western Dutch Wadden Sea?

To answer this research question, we developed an idealized network model that is an extension to the model used in the early 20^{th} to study the impact of the Afsluitdijk on the hydrodynamics in the Western Dutch Wadden Sea. This allowed us to study the effect of the transient behavior of storm surges as opposed to a steady state response as obtained by the State Committee on the Zuiderzee.

Using the model, we found that a decrease in the cross-shore basin length (e.g. due to construction of a dam) had two distinct effects. Firstly, it leads to higher water levels at the current location of the dam in comparison to the situation without a dam. Secondly, the water levels at the dam are slightly lower than at the southern end of the Zuiderzee before closure; and if a dam were constructed further to the south of its current location, the water levels at the dam would be higher than at the southern end of the Zuiderzee before closure. We found that this is caused by an increase in wind-fetch length, leading to higher storm surges in longer basin. Contrarily, the impact of higher water levels on the outer sea (i.e. the North Sea in case of the Wadden Sea) is largest near the tidal inlets and decreases towards the end of the tidal basin.

Finally, in order to achieve a maximum water set-up due to the wind shear stress, the storm should last for a significant period of time. So for short storm events, the approach by the State Committee will lead to an overestimation of the storm-surge height.

5.2. Synthesis

5.2.1 Stability of tidal inlets

For a tidal inlet Escoffier (1940) explained how its stability depends on a balance between accretion and erosion of an inlet channel, and linked this to a balance between the velocity amplitude of the tide in an inlet U and an equilibrium velocity amplitude U_{eq}. By coupling this concept with a simple hydrodynamic model, he found at most one stable equilibrium for a tidal inlet (see §1.2.2).

In this thesis, following Roos et al. (2013), we coupled Escoffier's stability concept with a hydrodynamic model covering a multiple inlet system and found multiple stable equilibria for these systems. By varying only the initial cross-section and location we found equilibria in which the location of the inlets, the equilibrium cross-section of the inlets, and the number of inlets varied but the equilibrium total tidal prism P flowing in and out of the basin each tidal cycle remained constant.

This implies that for a multiple inlet system in equilibrium, an increase in the number of inlets (e.g. due to storm-induced breaches; see Chapter 3 and §5.2.3) or decrease in the number of inlets (e.g. due to closure of an inlet) has an effect on the cross-section of other inlets connected to the same backbarrier basin. Thus if a storm-induced breach remains open, the inlets that were in a stable equilibrium will decrease in size as the same total tidal prism is now conveyed by more tidal inlets. Contrarily, if an inlet closes the same tidal prism has to be conveyed by fewer inlets, resulting in larger cross-sections for the remaining inlets

5.2.2 Size of the backbarrier basin

In this thesis we found that the cross-barrier basin length has a significant impact on both the equilibrium configuration of the tidal inlets, as well as on storm surge height.

The size of the backbarrier basin is a system characteristic that affects the total tidal prism P flowing in and out of the basin each tidal cycle and in turn affects the equilibrium cross-section and number of inlets (see Chapter 2). Previous literature often viewed the relation between basin size and tidal prism as a linear relation. We found this linear relation for smaller basin lengths, but for longer basins this relation is dominated by resonance before it becomes constant due to the dissipation of the tidal wave due to bottom friction.

Regarding storms, the size of the backbarrier basin primarily affects the peak elevation of the storm-surge through the link between basin length and wind-fetch length. A longer basin has a longer wind-fetch length, resulting in higher storm surges.

This implies that the changes in cross-barrier basin length, e.g. due to land

reclamation (see §1.3.1) or foreshore evolution (e.g. Willemsen et al., 2018), have an impact on storm surge height and tidal inlet cross-section. Moreover, the effect of a change in basin size affects all inlets connected to the same backbarrier basin, as they interact with each other.

5.2.3 Storm-impact on barrier coasts

We focused on two aspects of storm-impact on barrier coasts in this thesis.

Firstly, we investigated how storm-induced breaches affect the equilibria of multiple inlet systems and the stability of individual inlets. We found that despite the small initial size of storm-induced breaches, they can have a significant and lasting impact on entire barrier coast systems as the presence of a new inlet affects the cross-section of the other inlets (see Chapter 3).

Secondly, we studied how the propagation of storm-surges in a backbarrier basin is affected by the basin geometry (see Chapter 4). Here, we found that the maximum storm-surge height strongly depends on wind-fetch length and occurs at the end of the basin. Contrarily, the effect of higher water levels on the outer sea are largest near the tidal inlets and decrease further into the tidal basin.

5.3. Recommendations

Three topics for further research on the long-term morphological evolution of barrier coasts are presented here.

Firstly, the effect of bathymetric variations in the backbarrier basin on the equilibrium configuration of tidal inlets has not been studied in the case of multiple inlet systems. Similar to the cross-barrier basin length, the bathymetry of the basin has an effect on the tidal dynamics and thus the morphology of the tidal inlets as well. To do so, an extended version of the model presented in this thesis can be used, in which the bathymetry of the backbarrier basin is allowed to vary spatially (Reef et al., 2021).

Secondly, regarding the model presented in Chapter 2 the morphological model governing the evolution of the tidal inlets can be extended. Currently a fixed volume of sediment enters each inlet each timestep, but this can be improved using the formulations by Nienhuis and Ashton (2016). Therein, the amount of sediment entering an inlet is a fraction of the long-term net alongshore sediment transport rate.

Thirdly, the model presented in Chapter 2 can be used to provide input for other models such as ASMITA. As that model depends on an observed equilibrium state, it is less suited to investigate how such an equilibrium state changes under e.g. climate change. Using the models presented in this thesis these changes can be estimated, and in turn be used as input in other models.

Bibliography

Alebregtse, N. C. and H. E. De Swart (2014). "Effect of a secondary channel on the non-linear tidal dynamics in a semi-enclosed channel: A simple model". In: *Ocean Dynamics* 64.4, pp. 573–585. DOI: 10.1007/s10236-014-0690-0.

Alebregtse, N. C. and H. E. De Swart (2016). "Effect of river discharge and geometry on tides and net water transport in an estuarine network, an idealized model applied to the Yangtze Estuary". In: *Continental Shelf Research* 123, pp. 29–49. DOI: 10.1016/j.csr.2016.03.028.

Alebregtse, N. C., H. E. De Swart, and H. M. Schuttelaars (2013). "Resonance characteristics of tides in branching channels". In: *Journal of Fluid Mechanics* 728.10. DOI: 10.1017/jfm.2013.319.

Andringa, T. E. (2017). *Modelling the impact of storm-induced breaching on the morphodynamic evolution and stability of multiple tidal inlet systems*. URL: https://www.utwente.nl/en/et/wem/education/msc-thesis/2017/andringa.pdf.

Barua, D. K. (2017). "Seabed Roughness of Coastal Waters". In: *EncyclopediaofCoastalScience*. Ed. by C. Finkl and C. Makawoski. Vol. 14. 1. Springer International Publishing. DOI: 10.1007/978-3-319-48657-4.

Bolger, T. (2012). *Questions Surround Rebuilding Fire Island*. URL: http://archive.longislandpress.com/2012/11/22/questions-surround-rebuilding-fire-island/.

Bonilla, D. M. (2012). *Cuomo: Breaches near Moriches Inlet to be closed*. URL: https://www.newsday.com/long-island/suffolk/cuomo-breaches-near-moriches-inlet-to-be-closed-1.4229821.

Brouwer, R. L., H. M. Schuttelaars, and P. C. Roos (2012a). "Influence of basin geometry on equilibrium and stability of double inlet systems". In: *Jubilee Conference Proceedings NCK-days 2012: Crossing borders in coastal research*, pp. 85–89. DOI: 10.3990/2.175.

Brouwer, R. L., J. Van de Kreeke, and H. M. Schuttelaars (2012b). "Entrance/exit losses and cross-sectional stability of double inlet systems". In: *Estuarine, Coastal and Shelf Science* 107, pp. 69–80. DOI: 10.1016/j.ecss.2012.04.033.

Brouwer, R. L., H. M. Schuttelaars, and P. C. Roos (2013). "Modelling the influence of spatially varying hydrodynamics on the cross-sectional stability of double inlet systems". In: *Ocean Dynamics* 63.11, pp. 1263–1278. DOI: 10.1007/s10236-013-0657-6.

Buchwald, V. T. (1971). "The diffraction of tides by a narrow channel". In: *Journal of Fluid Mechanics* 46.3, pp. 501–511. DOI: 10.1017/S0022112071000661.

Cañizares, R. and J. L. Irish (2008). "Simulation of storm-induced barrier island morphodynamics and flooding". In: *Coastal Engineering* 55.12, pp. 1089–1101. DOI: 10.1016/j.coastaleng.2008.04.006.

Chen, W. L., P. C. Roos, H. M. Schuttelaars, and S. J. M. H. Hulscher (2015). "Resonance properties of a closed rotating rectangular basin subject to space- and time-dependent wind forcing". In: *Ocean Dynamics* 65.3, pp. 325–339. DOI: 10.1007/s10236-015-0813-2.

Chen, W. L., P. C. Roos, H. M. Schuttelaars, M. Kumar, T. J. Zitman, and S. J. M. H. Hulscher (2016). "Response of large-scale coastal basins to wind forcing: influence of topography". In: *Ocean Dynamics* 66.4, pp. 549–565. DOI: 10.1007/s10236-016-0927-1.

Chow, V. T. (1959). *Open-channel hydraulics*. New York: McGraw- Hill Book Co. ISBN: 978-0070107762.

Clinch, A. S., E. R. Russ, R. C. Oliver, H. Mitasova, and M. F. Overton (2012). "Hurricane Irene and the Pea Island breach: prestorm site characterization and storm surge estimation using geospatial technologies". In: *Shore and Beach* 80.2, pp. 38–46.

Curray, J. R. (1964). "Transgressions and regressions". In: *Papers in marine geology*. Ed. by R. L. Miller. New York: Macmillan, pp. 175–203.

D'Alpaos, A., S. Lanzoni, M. Marani, and A. Rinaldo (2010). "On the tidal prism-channel area relations". In: *Journal of Geophysical Research: Earth Surface* 115.1, pp. 1–13. DOI: 10.1029/2008JF001243.

Dastgheib, A., J. A. Roelvink, and Z. B. Wang (2008). "Long-term process-based morphological modeling of the Marsdiep Tidal Basin". In: *Marine Geology* 256.1-4, pp. 90–100. DOI: 10.1016/j.margeo.2008.10.003.

Davis, R. A. and M. O. Hayes (1984). "What is a Wave-Dominated Coast?" In: *Developments in Sedimentology* 39.C, pp. 313–329. DOI: 10.1016/S0070-4571(08)70152-3.

De Swart, H. E. and N. D. Volp (2012). "Effects of hypsometry on the morphodynamic stability of single and multiple tidal inlet systems". In: *Journal of Sea Research* 74, pp. 35–44. DOI: 10.1016/j.seares.2012.05.008.

De Swart, H. E. and J. T. F. Zimmerman (2009). "Morphodynamics of Tidal Inlet Systems". In: *Annual Review of Fluid Mechanics* 41.1, pp. 203–229. DOI: 10.1146/annurev.fluid.010908.165159.

De Vet, P. L. M., R. T. McCall, J. P. Den Bieman, M. J. F. Stive, and M. Van Ormondt (2015). "Modelling Dune Erosion, Overwash and Breaching At Fire

Island (NY) During Hurricane Sandy". In: *Coastal Sediments 2015*, pp. 1–10. DOI: 10.1142/9789814689977_0006.

Dias, J. M., M. C. Sousa, X. Bertin, A. B. Fortunato, and A. Oliveira (2009). "Numerical modeling of the impact of the Ancão Inlet relocation (Ria Formosa, Portugal)". In: *Environmental Modelling and Software* 24.6, pp. 711–725. DOI: 10.1016/j.envsoft.2008.10.017.

Duran-Matute, M., T. Gerkema, G. J. De Boer, J. J. Nauw, and U. Gräwe (2014). "Residual circulation and freshwater transport in the Dutch Wadden Sea: A numerical modelling study". In: *Ocean Science* 10.4, pp. 611–632. DOI: 10.5194/os-10-611-2014.

Duran-Matute, M., T. Gerkema, and M. G. Sassi (2016). "Quantifying the residual volume transport through a multiple-inlet system in response to wind forcing: The case of the western Dutch Wadden Sea". In: *Journal of Geophysical Research: Oceans* 121.12, pp. 8888–8903. DOI: 10.1002/2016JC011807.

Elias, E. P. L., M. J. F. Stive, H. Bonekamp, and J. Cleveringa (2003). "Tidal inlet dynamics in response to human intervention". In: *Coastal Engineering Journal* 45.4, pp. 629–658. DOI: 10.1142/S0578563403000932.

Elias, E. P. L., A. J. F. Van Der Spek, Z. B. Wang, and J. De Ronde (2012). "Morphodynamic development and sediment budget of the Dutch Wadden Sea over the last century". In: *Geologie en Mijnbouw/Netherlands Journal of Geosciences* 91.3, pp. 293–310. DOI: 10.1017/S0016774600000457.

Escoffier, E. F. (1940). "The stability of tidal inlets". In: *Shore and Beach* 8.4, pp. 114–115.

FEMA (2013). *Hurricane Sandy in New Jersey and New York: Building Performance Observations, Recommendations, and Technical Guidance*. Tech. rep. FEMA P-942. Federal Emergency Management Agency, p. 223. DOI: 10.7282/T3J67F96.

FitzGerald, D. M. (1996). "Geomorphic Variability and Morphologic and Sedimentologic Controls on Tidal Inlets". In: *Journal of Coastal Research* 23, pp. 47–71. DOI: 10.2307/25736068.

Flagg, C., C. Hinrichs, R. Flood, and R. Wilson (2017). *Update on the Status of Old Inlet Breach*. Tech. rep. Stony Brook University. URL: http://po.msrc.sunysb.edu/GSB/Inlet%7B%5C_%7DReport%7B%5C_%7D17.pdf.

Flemming, B. and K. Ziegler (1995). "High-Resolution Grain Size Distribution Patterns and Textural Trends in the Backbarrier Environment of Spiekeroog Island (Southern North Sea)". In: *Senckenbergiana maritima* 26.1, pp. 1–24.

Gerritsen, F. and D. W. Dunsbergen (1998). "Modelling Morphological-Empirical Relationships for Ebb Tidal Deltas as a Tool in Dynamic-Empirical Modelling". In: *Journal of Coastal Research* 81.26, pp. 273–281. URL: http://www.jstor.org/stable/25736150.

Glaeser, J. D. (1978). "Global Distribution of Barrier Islands in Terms of Tectonic Setting". In: *Journal of Geology* 86.3, pp. 283–297. DOI: 10.1086/649691.

Google (2016). *Google Earth, Map Data: Copernicus, DigitalGlobe, GEBCO, Landsat, NOAA, SIO, TerraMetrics, USDA Farm Service Agency, US Navy.*

Haas, T. de, H. J. Pierik, A. J. F. van der Spek, K. M. Cohen, B. van Maanen, and M. G. Kleinhans (2018). "Holocene evolution of tidal systems in The Netherlands: Effects of rivers, coastal boundary conditions, eco-engineering species, inherited relief and human interference". In: *Earth-Science Reviews* 177, pp. 139–163. DOI: 10.1016/j.earscirev.2017.10.006.

Harter, C. and J. Figlus (2017). "Numerical modeling of the morphodynamic response of a low-lying barrier island beach and foredune system inundated during Hurricane Ike using XBeach and CSHORE". In: *Coastal Engineering* 120.October 2016, pp. 64–74. DOI: 10.1016/j.coastaleng.2016.11.005.

Hayes, M. O. (1979). "Barrier Island Morphology as a Function of Wave and Tide Regime". In: *Barrier islands: from the Gulf of St. Lawrence to the Gulf of Mexico*. Ed. by S. P. Leatherman, pp. 1–27. ISBN: 0124402607.

Hayes, M. O. and D. M. FitzGerald (2013). "Origin, Evolution, and Classification of Tidal Inlets". In: *Journal of Coastal Research* 69.69, pp. 14–33. DOI: 10.2112/si_69_3.

Hill, A. E. and A. J. Souza (2006). "Tidal dynamics in channels: 2. Complex channel networks". In: *Journal of Geophysical Research: Oceans* 111.11. DOI: 10.1029/2006JC003670.

Hinrichs, C., C. N. Flagg, and R. E. Wilson (2018). "Great South Bay After Sandy: Changes in Circulation and Flushing due to New Inlet". In: *Estuaries and Coasts* 41.8, pp. 2172–2190. DOI: 10.1007/s12237-018-0423-6.

Horsburgh, K. J. and C. Wilson (2007). "Tide-surge interaction and its role in the distribution of surge residuals in the North Sea". In: *Journal of Geophysical Research: Oceans* 112.8. DOI: 10.1029/2006JC004033.

Hosseini, S. R., M. Marani, and M. Scaioni (2016). "Statistical Distribution Fits for Hurricanes Parameters in the Atlantic Basin". In: *ASITA*, pp. 446–452. URL: http://atti.asita.it/ASITA2016/Pdf/123.pdf.

Inman, D. L. and R. Dolan (1989). "The Outer Banks of North Carolina: budget of sediment and inlet dynamics along a migrating barrier system". In: *Journal of Coastal Research* 5.2, pp. 193–237.

Intergovernmental Panel on Climate Change (2013). *Climate Phenomena and their Relevance for Future Regional Climate Change Supplementary Material*. Cambridge: Cambridge University Press, pp. 1217–1308. ISBN: ISBN 978-1-107-66182-0. DOI: 10.1017/CBO9781107415324.028.

Jallah, A. N. and W. T. Bakker (1994). *Lorentz on PC. A PC approach to the Lorentz tidal computation method — based on a 1-dimensional linear model —*. Tech. rep. Univ. Technol., Dep. Hydraul. eng. URL: https://puc.overheid.nl/rijkswaterstaat/doc/PUC%7B%5C_%7D98064%7B%5C_%7D31/.

Jarret, J. (1976). *Tidal prism-inlet area relationships General investigation of tidal inlets*. Tech. rep. U.S. Army Coastal Engineering Research Center, Fort Belvoir, VA. U.S. Army Engineers Waterways Experiment Station, Vicksburg, MS. URL: https://usace.contentdm.oclc.org/digital/api/collection/p266001coll1/id/7466/download.

Keim, B. D., R. A. Muller, and G. W. Stone (2007). "Spatiotemporal patterns and return periods of tropical storm and hurricane strikes from Texas to Maine". In: *Journal of Climate* 20.14, pp. 3498–3509. DOI: 10.1175/JCLI4187.1.

KNMI (2016). *Uurgegevens van het weer in Nederland*. URL: http://projects.knmi.nl/klimatologie/uurgegevens/selectie.cgi.

Kombiadou, K., A. Matias, Ó. Ferreira, A. R. Carrasco, S. Costas, and T. Plomaritis (2019). "Impacts of human interventions on the evolution of the Ria Formosa barrier island system (S. Portugal)". In: *Geomorphology* 343, pp. 129–144. DOI: 10.1016/j.geomorph.2019.07.006.

Kox, A. (2007). "Uit de hand gelopen onderzoek in opdracht: H.A. Lorentz' werk in de Zuiderzeecommissie". In: *Onderzoek in Opdracht: De publieke functie van het universitaire onderzoek in Nederland sedert 1876*. Ed. by L. J. Dorsman and P. J. Knegtmans. Verloren, pp. 39–52. URL: https://hdl.handle.net/11245/1.276683.

Kragtwijk, N. G., T. J. Zitman, M. J. F. Stive, and Z. B. Wang (2004). "Morphological response of tidal basins to human interventions". In: *Coastal Engineering* 51.3, pp. 207–221. DOI: 10.1016/j.coastaleng.2003.12.008.

Kraus, N. C., A. Militello, and G. Todoroff (2002). "Barrier Beaching Processes and Barrier Spit Breach, Stone Lagoon, California". In: *Shore and Beach* 70.4, pp. 21–28.

Leatherman, S. P. (1985). "Geomorphic and Stratigraphic analysis of Fire Island, New York". In: *Marine Geology* 63, pp. 173–195.

Leatherman, S. P. (1989). "Role of inlets in geomorphic evolution of the south shore barriers of Long Island, New York, USA". In: *Environmental Management* 13.1, pp. 109–115. DOI: 10.1007/BF01867592.

Lehoucq, R. B., D. C. Sorensen, and C. Yang (1998). *ARPACK Users' Guide: Solution of Large-scale Eigenvalue Problems with Implicitly Restarted Arnoldi Methods*, p. 152. ISBN: 0898714079.

Lely, C. (1892). "Design for the closure of the Zuiderzee (in Dutch)". Enkhuizen. URL: https://geheugen.delpher.nl/nl/geheugen/view?coll=ngvn%7B%5C&%7Didentifier=ZZM01%7B%5C%%7D3A013525.

Lindemer, C. A., N. G. Plant, J. A. Puleo, D. M. Thompson, and T. V. Wamsley (2010). "Numerical simulation of a low-lying barrier island's morphological response to Hurricane Katrina". In: *Coastal Engineering* 57.11-12, pp. 985–995. DOI: 10.1016/j.coastaleng.2010.06.004.

Lipari, G. and G. P. van Vledder (2009). *Viability study of a prototype windstorm for the Wadden Sea surges*. Tech. rep. Alkyon Hydraulic Consultancy & Research. URL: http://publications.deltares.nl/WeL1938.pdf.

Lipari, G., G. P. van Vledder, J. Adema, J. Cleveringa, O. Koop, and A. Haghgoo (2008). *Simulation studies for storm winds, flow fields and wave climate in the Wadden Sea*. Tech. rep. Alkyon Hydraulic Consultancy & Research. URL: http://publications.deltares.nl/WeL1937.pdf.

Lorentz, H. A. (1922). "Ein Rechnungsansatz für den Widerstand bei Flüssigkeitsschwingungen". In: *De Ingenieur* 37, p. 695.

Luettich, R. A., S. D. Carr, J. V. Reynolds-Fleming, C. W. Fulcher, and J. E. McNinch (2002). "Semi-diurnal seiching in a shallow, micro-tidal lagoonal estuary". In: *Continental Shelf Research* 22.11-13, pp. 1669–1681. DOI: 10.1016/S0278-4343(02)00031-6.

MacIvor, L. H. and K. Motivans (1998). *Impacts to Piping Plover and Seabeach Amaranth from Long-Term Sand Management Component*. Tech. rep. March 1998. US Army Corps of Engineers.

Mallinson, D. J., S. J. Culver, S. R. Riggs, J. P. Walsh, D. Ames, and C. W. Smith (2008). *Past, present and future inlets of the Outer Banks barrier islands, North Carolina*. Tech. rep. URL: https://www.ecu.edu/icsp/ICSP/Reports%7B%5C_%7Dfiles/PastPresentAndFutureInletsDec2008.pdf.

Mallinson, D. J., S. J. Culver, E. Leorri, S. Mitra, R. Mulligan, and S. R. Riggs (2018). "Barrier Island and estuary co-evolution in response to holocene climate and sea-level change: Pamlico sound and the outer banks Barrier Islands, North Carolina, USA". In: *Barrier Dynamics and Response to Changing Climate*, pp. 91–120. ISBN: 9783319680866. DOI: 10.1007/978-3-319-68086-6_3.

Mallinson, D. J., C. W. Smith, S. J. Culver, S. R. Riggs, and D. Ames (2010). "Geological characteristics and spatial distribution of paleo-inlet channels beneath the outer banks barrier islands, North Carolina, USA". In: *Estuarine, Coastal and Shelf Science* 88.2, pp. 175–189. DOI: 10.1016/j.ecss.2010.03.024.

Matias, A., Ó. Ferreira, and J. M. Alveirinho-Dias (1999). "Preliminary results of the Cacela Peninsula (southern Portugal) replenishment". In: *Bol. Inst. Esp. Oceanogr* 15.June 2014, pp. 1–4. URL: http://w3.ualg.pt/%7B~%7Djdias/JAD/papers/RN/99-BIEO%7B%5C_%7D283%7B%5C_%7DCacela%7B%5C_%7DAM.pdf.

Mazure, J. P. (1963). "Hydraulic research for the Zuiderzeeworks". In: *In: Selected aspects of hydraulic engineering, Liber Amicorum dedicated to Johannes Theodoor Thijsse, on occasion of his retirement as professor.* TU Delft, Section Hydraulic Engineering.

Mickey, R., J. Long, P. S. Dalyander, N. Plant, and D. Thompson (2018). "A framework for modeling scenario-based barrier island storm impacts". In: *Coastal Engineering* 138.June 2017, pp. 98–112. DOI: 10.1016/j.coastaleng.2018.04.012.

Mulhern, J. S., C. L. Johnson, and J. M. Martin (2017). "Is barrier island morphology a function of tidal and wave regime?" In: *Marine Geology* 387, pp. 74–84. DOI: 10.1016/j.margeo.2017.02.016. URL: http://linkinghub.elsevier.com/retrieve/pii/S002532271630189X.

Murray, A. B. (2003). "Contrasting the goals, strategies, and predictions associated with simplified numerical models and detailed simulations". In: *Geophysical Monograph Series* 135, pp. 151–165. DOI: 10.1029/135GM11.

Nahon, A., X. Bertin, A. B. Fortunato, and A. Oliveira (2012). "Process-based 2DH morphodynamic modeling of tidal inlets: A comparison with empirical classifications and theories". In: *Marine Geology* 291-294, pp. 1–11. DOI: 10.1016/j.margeo.2011.10.001.

National Oceanic and Atmospheric Administration (2020). *NOAA TIDES \& CURRENTS. USCG Station Hatteras, NC*. URL: https://tidesandcurrents.noaa.gov/stationhome.html?id=8654467 (visited on 01/20/2020).

Nienhuis, J. H. and A. D. Ashton (2016). "Mechanics and rates of tidal inlet migration: Modeling and application to natural examples". In: *Journal of Geophysical Research: Earth Surface* 121.11, pp. 2118–2139. DOI: 10.1002/2016JF004035.

O'Brien, M. P. (1931). "Estuary tidal prisms related to entrance areas". In: *Civil Engineering* 1.8, pp. 738–139.

O'Brien, M. P. (1969). "Equilibrium flow areas of tidal inlets on sandy coasts". In: *J. Waterw. Harb. Div.* WW1, pp. 43–52. DOI: 10.9753/icce.v10.25p.

Oost, A. P., P. Hoekstra, A. Wiersma, B. Flemming, E. J. Lammerts, M. Pejrup, J. Hofstede, B. van der Valk, P. Kiden, J. Bartholdy, M. W. van der Berg, P. C. Vos, S. de Vries, and Z. B. Wang (2012). "Barrier island management: Lessons from the past and directions for the future". In: *Ocean and Coastal Management* 68, pp. 18–38. DOI: 10.1016/j.ocecoaman.2012.07.010.

Pacheco, A., A. Vila-Concejo, Ó. Ferreira, and J. A. Dias (2008). "Assessment of tidal inlet evolution and stability using sediment budget computations and hydraulic parameter analysis". In: *Marine Geology* 247.1-2, pp. 104–127. DOI: 10.1016/j.margeo.2007.07.003.

Polyanin, A. D. (2002). *Handbook of linear partial differential equations for engineers and scientists*. Chapman & Hall/CRC, p. 743. ISBN: 1584882999.

Prandle, D. and J. Wolf (1978). "The interaction of surge and tide in the North Sea and River Thames". In: *Geophysical Journal of the Royal Astronomical Society* 55.1, pp. 203–216. DOI: 10.1111/j.1365-246X.1978.tb04758.x.

Puch, D. T. (1983). *Tides, surges and mean sea level trends.* (Southampton, U.K.: Sep. 14-15, 1982), London, U.K., Thomas Telford Ltd., 1983, Session III, Paper 9. John Wiley & Sons Ltd. ISBN: 0727701738.

Reef, K. R. G. ., P. C. Roos, H. M. Schuttelaars, and S. J. M. H. Hulscher (2021). *Varying Depth Model*. URL: https://github.com/Kreef/VaryingDepth.

Reef, K. R. G., P. C. Roos, H. M. Schuttelaars, and S. J. M. H. Hulscher (2020a). "Influence of Back-Barrier Basin Geometry on Multiple Tidal Inlet Systems: The Roles of Resonance and Bottom Friction". In: *Journal of Geophysical Research: Earth Surface* 125.3. DOI: 10.1029/2019JF005261.

Reef, K. R. G., G. Lipari, P. C. Roos, and S. J. M. H. Hulscher (2018). "Time-varying storm surges on Lorentz ' s Wadden Sea networks". In: *Ocean Dynamics* 68.8, pp. 1051–1065. DOI: 10.1007/s10236-018-1181-5.

Reef, K. R. G., P. C. Roos, T. E. Andringa, A. Dastgheib, and S. J. M. H. Hulscher (2020b). "The Impact of storm-induced breaches on barrier coast systems

subject to climate change - A stochastic modelling study". In: *Journal of Marine Science and Engineering* 8.4. DOI: 10.3390/JMSE8040271.

Rijkswaterstaat (1916). *Verslag over de stormvloed van 13/14 januari 1916*. Tech. rep.

Rijkswaterstaat (2013). *Stormvloedrapport van 5 t/m 7 december 2013. Sint-Nicolaasvloed 2013*. Tech. rep. Watermanagementcentrum Nederland. URL: https://waterberichtgeving.rws.nl/water-en-weer/verwachtingen-water/water-en-weerverwachtingen-waternoordzee/stormvloedrapportages/stormvloedverslagen/download:835.

Rijkswaterstaat (2016). *Waterbase*. URL: live.waterbase.nl.

Roos, P. C., C. Pitzalis, G. Lipari, K. R. G. Reef, and S. J. M. H. Hulscher (2017). "Time-dependent linearisation of bottom friction for storm surge modelling in the Wadden Sea". In: *4th International symposium on shallow flows*. Eindhoven University of Technology.

Roos, P. C., H. M. Schuttelaars, and R. L. Brouwer (2013). "Observations of barrier island length explained using an exploratory morphodynamic model". In: *Geophysical Research Letters* 40.16, pp. 4338–4343. DOI: 10.1002/grl.50843.

Safaie, B. B. (1984). "Wind Stress at Air-Water Interface". In: *J. Waterway, Port, Coastal, Ocean Eng.* 110.2, pp. 287–293. DOI: 10.1061/(ASCE)0733-950X(1984)110:2(287).

Safak, I., J. C. Warner, and J. H. List (2016). "Barrier island breach evolution: Alongshore transport and bay-ocean pressure gradient interactions". In: *Journal of Geophysical Research: Oceans* 121, pp. 8720–8730. DOI: 10.1002/2016JC012029.

Sallenger, A. H. (2000). "Storm Impact Scale for Barrier Islands". In: *Journal of Coastal Research* 16.3, pp. 890–895. DOI: 10.2307/4300099.

Salles, P., G. Voulgaris, and D. G. Aubrey (2005). "Contribution of nonlinear mechanisms in the persistence of multiple tidal inlet systems". In: *Estuarine, Coastal and Shelf Science* 65.3, pp. 475–491. DOI: 10.1016/j.ecss.2005.06.018.

Sassi, M., M. Duran-Matute, T. van Kessel, and T. Gerkema (2015). "Variability of residual fluxes of suspended sediment in a multiple tidal-inlet system: the Dutch Wadden Sea". In: *Ocean Dynamics* 65.9-10, pp. 1321–1333. DOI: 10.1007/s10236-015-0866-2.

Sherwood, C. R., J. W. Long, P. J. Dickhudt, P. S. Dalyander, D. M. Thompson, and N. G. Plant (2014). "Inundation of Barrier Islands during a Hurricane".

In: *Journal of Geophysical Research: Earth Surface* 119, pp. 1498–1515. DOI: 10.1002/2013JF003069.Received.

Simms, A. R., J. B. Anderson, and M. Blum (2006). "Barrier-island aggradation via inlet migration: Mustang Island, Texas". In: *Sedimentary Geology* 187.1-2, pp. 105–125. DOI: 10.1016/j.sedgeo.2005.12.023.

Sommerfeld, A. (1949). *Partial Differential Equations in Physics*. 1st. New York: Academic Press Inc. ISBN: 978-0126546569.

Spencer, T., S. M. Brooks, B. R. Evans, J. A. Tempest, and I. Möller (2015). "Southern North Sea storm surge event of 5 December 2013: Water levels, waves and coastal impacts". In: *Earth-Science Reviews* 146, pp. 120–145. DOI: 10.1016/j.earscirev.2015.04.002.

State Committee on the Zuiderzee (1926). *Report of the State Committee on the Zuiderzee (in Dutch)*. report. 's Gravenhage.

Stroband, H. J. and N. J. V. Wijngaarden (1977). "Modelling of the Oosterschelde estuary by a hydraulic model and a mathematical model." In: *in: Proc. Seventeenth Congress of the International Association for Hydraulic Research, Hydraulic Engineering for Improved Wa*. Vol. 2 , Subjec, pp. 271–278.

Stutz, M. L. and O. H. Pilkey (2011). "Open-ocean barrier islands: Global influence of climatic, oceanographic, and depositional settings". In: *Journal of Coastal Research* 27.2, pp. 207–222. DOI: 10.2112/09-1190.1.

Tran, T.-T., J. van de Kreeke, M. J. F. Stive, and D.-J. R. Walstra (2012). "Cross-sectional stability of tidal inlets: A comparison between numerical and empirical approaches". In: *Coastal Engineering* 60, pp. 21–29. DOI: http://dx.doi.org/10.1016/j.coastaleng.2011.08.005.

United Nations (2017). *Factsheet: People and Oceans*. URL: https://www.un.org/sustainabledevelopment/wp-content/uploads/2017/05/Ocean-fact-sheet-package.pdf.

United States Geological Survery (2019). *National Water Information System: Web Interface. USGS 02084472 PAMLICO RIVER AT WASHINGTON, NC*. URL: waterdata.usgs.gov (visited on 01/20/2020).

United States Geological Survey (2016). *LandsatLook Viewer: a prototype tool that allows rapid online viewing and access to the USGS Landsat archive*. URL: http://landsatlook.usgs.gov.

Van de Kreeke, J. (1990a). "Can multiple tidal inlets be stable?" In: *Estuarine, Coastal and Shelf Science* 30.3, pp. 261–273. DOI: 10.1016/0272-7714(90)90051-R.

Van de Kreeke, J. (1990b). "Stability analysis of a two-inlet bay system". In: *Coastal Engineering* 14.6, pp. 481–497. DOI: 10.1016/0378-3839(90)90031-Q.

Van de Kreeke, J. (2004). "Equilibrium and cross-sectional stability of tidal inlets: Application to the Frisian Inlet before and after basin reduction". In: *Coastal Engineering* 51.5-6, pp. 337–350. DOI: 10.1016/j.coastaleng.2004.05.002.

Van de Kreeke, J., R. L. Brouwer, T. J. Zitman, and H. M. Schuttelaars (2008). "The effect of a topographic high on the morphological stability of a two-inlet bay system". In: *Coastal Engineering* 55.4, pp. 319–332. DOI: 10.1016/j.coastaleng.2007.11.010.

Van der Lugt, M. A., E. Quataert, A. Van Dongeren, M. Van Ormondt, and C. R. Sherwood (2019). "Morphodynamic modeling of the response of two barrier islands to Atlantic hurricane forcing". In: *Estuarine, Coastal and Shelf Science* 229.October, p. 106404. DOI: 10.1016/j.ecss.2019.106404. URL: https://doi.org/10.1016/j.ecss.2019.106404.

Van Goor, M. A., T. J. Zitman, Z. B. Wang, and M. J. F. Stive (2003). "Impact of sea-level rise on the morphological equilibrium state of tidal inlets". In: *Marine Geology* 202.3-4, pp. 211–227. DOI: 10.1016/S0025-3227(03)00262-7.

Van Straaten, L. (1954). "Composition and structure of recent marine sediments in the Netherlands". In: *Leidse Geologische Mededelingen* 19.1, pp. 1–108.

Velasquez Montoya, L., E. J. Sciaudone, H. Mitasova, and M. F. Overton (2018). "Observation and modeling of the evolution of an ephemeral storm-induced inlet: Pea Island Breach, North Carolina, USA". In: *Continental Shelf Research* 156.March 2017, pp. 55–69. DOI: 10.1016/j.csr.2018.02.002.

Vila-Concejo, A., Ó. Ferreira, B. D. Morris, A. Matias, and J. M. A. Dias (2004). "Lessons from inlet relocation: Examples from Southern Portugal". In: *Coastal Engineering* 51.10, pp. 967–990. DOI: 10.1016/j.coastaleng.2004.07.019.

Vila-Concejo, A., A. Matias, Ó. Ferreira, C. Duarte, and J. M. A. Dias (2002). "Recent Evolution of the Natural Inlets of a Barrier Island System in Southern Portugal". In: *Journal of Coastal Research* 36.September, pp. 741–752. DOI: 10.2112/1551-5036-36.sp1.741.

Vila-Concejo, A., A. Matias, A. Pacheco, Ó. Ferreira, and J. A. Dias (2006). "Quantification of inlet-related hazards in barrier island systems. An example from the Ria Formosa (Portugal)". In: *Continental Shelf Research* 26.9, pp. 1045–1060. DOI: 10.1016/j.csr.2005.12.014.

Vogel, M. J. and T. W. Kana (1984). "Sedimentation patterns in a tidal inlet system Moriches Inlet, New York". In: *Coastal Engineering Proceedings*, pp. 3017–3033. ISBN: 0872624382.

Vos, P. C. and E. Knol (2015). "Holocene landscape reconstruction of the Wadden Sea area between Marsdiep and Weser". In: *Geologie en Mijnbouw/Netherlands Journal of Geosciences* 94.2, pp. 157–183. DOI: 10.1017/njg.2015.4.

Wamsley, T. V., K. K. Hathaway, and M. Wutkowski (2010). *Hatteras Breach, North Carolina*. Tech. rep. July. US Army Corps of Engineers, p. 23.

Wang, Z. B., P. Hoekstra, H. Burchard, H. Ridderinkhof, H. E. De Swart, and M. J. F. Stive (2012). "Morphodynamics of the Wadden Sea and its barrier island system". In: *Ocean and Coastal Management* 68, pp. 39–57. DOI: 10.1016/j.ocecoaman.2011.12.022.

Willemsen, P. W. J. M., B. W. Borsje, S. J. M. H. Hulscher, D. Van der Wal, Z. Zhu, B. Oteman, B. Evans, I. Möller, and T. J. Bouma (2018). "Quantifying Bed Level Change at the Transition of Tidal Flat and Salt Marsh: Can We Understand the Lateral Location of the Marsh Edge?" In: *Journal of Geophysical Research: Earth Surface* 123.10, pp. 2509–2524. DOI: 10.1029/2018JF004742.

Yu, J., R. E. Wilson, and C. N. Flagg (2018). "A Hydraulic Model for Multiple-Bay-Inlet Systems on Barrier Islands". In: *Estuaries and Coasts* 41.2, pp. 373–383. DOI: 10.1007/s12237-017-0294-2.

Zijl, F., M. Verlaan, and H. Gerritsen (2013). "Improved water-level forecasting for the Northwest European Shelf and North Sea through direct modelling of tide, surge and non-linear interaction". In: 63.7, pp. 823–847. DOI: 10.1007/s10236-013-0624-2.

Publications

Peer-reviewed journal papers

1. **Reef, K. R. G.**, P. C. Roos, H. M. Schuttelaars, and S. J. M. H. Hulscher (2020a). “Influence of Back-Barrier Basin Geometry on Multiple Tidal Inlet Systems: The Roles of Resonance and Bottom Friction”. In: *Journal of Geophysical Research: Earth Surface* 125.3. DOI: 10.1029/2019JF005261.

2. **Reef, K. R. G.**, P. C. Roos, T. E. Andringa, A. Dastgheib, and S. J. M. H. Hulscher (2020b). “The Impact of storm-induced breaches on barrier coast systems subject to climate change - A stochastic modelling study”. In: *Journal of Marine Science and Engineering* 8.4. DOI: 10.3390/JMSE8040271.

3. **Reef, K. R. G.**, G. Lipari, P. C. Roos, and S. J. M. H. Hulscher (2018). “Time-varying storm surges on Lorentz ’ s Wadden Sea networks”. In: *Ocean Dynamics* 68.8, pp. 1051–1065. DOI: 10.1007/s10236-018-1181-5.

4. Roos, P. C., G. Lipari, C. Pitzalis, **K. R. G. Reef**, G. H. P. Campmans, and S. J. M. H. Hulscher (2021). “Unsteady Linearisation of Bed Shear Stress for Idealised Storm Surge Modelling”. In: *Journal of Marine Science and Engineering* 9.11, p. 1160. DOI: 10.3390/jmse9111160.

Conference papers and abstracts

1. **Reef, K. R. G.**, P. C. Roos, H. M. Schuttelaars, and S. J. M. H. Hulscher (2020). "How do tidal divides affect the morphological evolution of tidal inlets?". Abstract from NCK-days 2020, Texel, the Netherlands.

2. **Reef, K. R. G.**, P. C. Roos, H. M. Schuttelaars, and S. J. M. H. Hulscher (2019). "The impact of basin geometry on the long-term morphological evolution of barrier coasts: an exploratory modelling study". In: RCEM 2019: the 11th Symposium on River, Coastal and Estuarine Morphodynamics: Book of abstracts. Ed. by H. Friedrich and K. Bryan.

3. **Reef, K. R. G.**, P. C. Roos, T. Andringa, A. Dastgheib, and S. J. M. H. Hulscher (2019). “the Effect of Stochastically Simulated Storm-Induced Breaches on the Long-Term Morphological Evolution of Barrier Coasts”. In: Proceedings of the 9th International Conference on Coastal Sediments 2019. Ed. by P. Wang, J. D. Rosati, and M.Vallee. WorldScientific, pp.139–148. DOI: 10.1142/9789811204487_0013.

4. **Reef, K. R. G.**, P. C. Roos, H. M. Schuttelaars, and S. J. M. H. Hulscher (2019). "The influence of basin geometry on the long-term morphological evolution

of barrier coasts". Abstract from NCK-days 2019, Enkhuizen, the Netherlands.

5. **Reef, K. R. G.**, P. C. Roos, H. M. Schuttelaars, and S. J. M. H. Hulscher (2018). "WADSnext! morphodynamic modelling tools for the sustainable management of barrier coasts" Abstract from the 16th ISISA Islands of the World Conference 2018, Leeuwaarden, the Netherlands.

6. **Reef, K. R. G.**, P. C. Roos, T. Andringa, A. Dastgheib, and S. J. M. H. Hulscher (2018). "Long-term morphological behavior of barrier coasts: influence of storm-induced breaches using stochastic modelling". Abstract from NCK-days 2018, Haarlem, the Netherlands.

7. **Reef, K. R. G.**, P. C. Roos, H. M. Schuttelaars, and S. J. M. H. Hulscher (2017). "Exploratory modelling of mesotidal barrier coasts: the influence of basin geometry on equilibrium configurations". Abstract from ECSA Focus Meeting, Where Land Meets Ocean: The Vulnerable Interface 2017, Shanghai, China.

8. **Reef, K. R. G.**, P. C. Roos, G. Lipari, and S. J. M. H. Hulscher (2016). "A time-dependent network model for storm surges in the Wadden Sea". Abstract from the 18th Physics of Estuaries and Coastal Seas Conference 2016, Scheveningen, the Netherlands.

Professional publications

1. **Reef, K. R. G.**, P. C. Roos, H. M. Schuttelaars, S. J. M. H. Hulscher (2017). "Exploratory Modelling of Mesotidal Barrier Coasts: Using Idealized Models to study the Lont-Term behavior of the Wadden Sea". In: ConcepTueel 26.4, pp. 16-19.

2. **Reef, K. R. G.**, P. C. Roos, G. Lipari, and S.J.M.H. Hulscher (2016). "Het uitbreiden van Lorentz stormvloedmodel". ConcepTueel 25.4.

3. **Reef, K. R. G.**, B. W. Borsje (2014). "Natuurvriendelijke Oevers in de IJssel". ConcepTueel 23.1.

About the author

Koen Reef grew up in the small city of Goor in the East of the Netherlands. After graduating from Twickel college in Hengelo, he entered the Civil Engineering program at the University of Twente in 2010. During his bachelor he did his minor at Luleå University of Technology in the north of Sweden and finished his bachelor with a thesis on river bank protection in the IJssel river, performed at Waterschap Vallei en Veluwe.

Koen continued his studies at the University of Twente with the Civil Engineering and Management program, following the Water Engineering and Management track. During his master he joined the Latin Links study tour in 2014 to study Civil Engineering projects in the South American countries of Argentina and Uruguay. For his master thesis he digitalized and extended a historical model that was used to study the impact of the Dutch Afsluitdijk and studied the storm-surges in the Wadden sea.

Koen started his PhD at the Water Engineering and Management group of the University of Twente in December 2016. Here he studied the long-term morphological evolution of barrier coasts. During his PhD he was actively involved in teaching various courses relating to Fluid Dynamics, Mathematics, and Programming; and as a supervisor on the Join Japan Study tour to Tokyo, Kyoto, Osaka, and Hiroshima in Japan. Koen presented his work at international conferences in Shanghai (China), St. Petersburg (Florida, USA) and Auckland (New Zealand).